Nanostructured Approaches to Light Management in Thin Silicon Solar Cells and Silicon-based Tandems

by

Natasa Vulic

A Dissertation Presented in Partial Fulfillment
of the Requirements for the Degree
Doctor of Philosophy

Approved April 2019 by the
Graduate Supervisory Committee:

Stephen Goodnick, Chair
Christiana Honsberg
Zachary Holman
David Smith

ARIZONA STATE UNIVERSITY

May 2019

ABSTRACT

Semiconductor nanostructures are promising building blocks for light management in thin silicon solar cells and silicon-based tandems due their tunable optical properties. The present dissertation is organized along three main research areas: (1) characterization and modeling of III-V nanowires as active elements of solar cell tandems, (2) modeling of silicon nanopillars for reduced optical losses in ultra-thin silicon solar cells, and (3) characterization and modeling of nanoparticle-based optical coatings for light management.

First, the recombination mechanisms in polytype GaAs nanowires are studied through photoluminescence measurements coupled with rate equation analysis. When photons are absorbed in polytype nanowires, electrons and holes quickly thermalize to the band-edges of the zinc-blende and wurtzite phases, recombining indirectly in space across the type-II offset. Using a rate equation model, different configurations of polytype defects along the nanowire are investigated, which compare well with experiment considering spatially indirect recombination between different polytypes, and defect-related recombination due to twin planes and other defects. The presented analysis is a path towards predicting the performance of nanowire-based solar cells.

Following this topic, the optical mechanisms in silicon nanopillar arrays are investigated using full-wave optical simulations in comparison to measured reflectance data. The simulated electric field energy density profiles are used to elucidate the mechanisms contributing to the reduced front surface reflectance. Strong forward scattering and resonant absorption are observed for shorter- and longer- aspect ratio nanopillars, respectively, with the sub-wavelength periodicity causing additional diffraction. Their potential for light-trapping is investigated using full-wave optical

simulation of an ultra-thin nanostructured substrate, where the conventional light-trapping limit is exceeded for near-bandgap wavelengths.

Finally, the correlation between the optical properties of silicon nanoparticle layers to their respective pore size distributions is investigated using optical and structural characterization coupled with full-wave optical simulation. The presence of scattering is experimentally correlated to wider pore size distributions obtained from nitrogen adsorption measurements. The correlation is validated with optical simulation of random and clustered structures, with the latter approximating experimental. Reduced structural inhomogeneity in low-refractive-index nanoparticle inter-layers at the metal/semiconductor interface improves their performance as back reflectors, while reducing parasitic absorption in the metal.

ACKNOWLEDGMENTS

I would like to acknowledge those without whom the research presented in this dissertation would not be possible. First of all, I would like to thank my advisor, Prof. Stephen Goodnick, for his guidance and support over the years. He encouraged my ideas while providing critical feedback, allowing me to direct my research in ways that I saw interesting. In addition to being an accomplished researcher, his steady demeanor and good character made him an ideal advisor.

The research presented in Chap. 4 grew out of the one-year research assistantship at the École Polytechnique Fédérale de Lausanne (Laboratory of Semiconductor Materials headed by Prof. Anna Fontcuberta i Morral) that was funded through the Fulbright fellowship. Yannik Fontana is acknowledged for his assistance with the project design, Gözde Tütüncüoglu and Heidi Potts for providing the samples, Dmitry Mikulik for assisting in sample preparation, and Luca Francaviglia with training on the PL set-up and providing TEM images.

The research presented in Chap. 5 grew out of direct collaboration with Jea-Young Choi who fabricated, imaged and characterized the samples. Esther Alarcon Llado, who introduced me to optical modeling in nanostructures and provided assistance as I learned the ropes, thank you for your time and patience.

The research presented in Chap. 6 grew out of direct collaboration with the Holman Lab. Peter Firth and Nathan Rodkey performed the depositions and Joe Carpenter imaged the samples. Salman Manzoor, who shared his knowledge and trained me on the optical set-up used in the project, thank you for your time and assistance.

The funding agencies are acknowledged for their support that made this work possible. The NSF IGERT SUN program is acknowledged for funding the start-

ing two years of my PhD studies; the U.S. Fulbright Scholar/Swiss FCS Scholarship for funding the one-year research assistantship at École Polytechnique Fédérale de Lausanne; the Arizona State University Dean's Fellowships for partial research-assistantship funding throughout my PhD; and the ARCS Marley Foundation (in Memory of Milton "Bud" Webb) together with the Ronald E. & Sharon W. Thomas Graduate Fellowship for supplementary support. This material is based upon work supported in part by the National Science Foundation (NSF) and the Department of Energy (DOE) under NSF CA No. EEC-1041895. Any opinions, findings and conclusions or recommendations expressed in this material are those of the author and do not necessarily reflect those of NSF or DOE.

Aside from research, the people I met through the program made this time the most worthwhile. I would especially like to thank my original officemates, the 525 crew, for the daily dose of laughs, support, and perspective. Prad, the best person to bring a bit of nihilism to make you feel better with a quote from *Rick and Morty* "Nobody exists on purpose. Nobody belongs anywhere. Everybody's gonna die." said in a very positive and reassuring way. Robin, who has so eloquently captured how working in research makes you feel most of the time: "I am an idiot. I finally figured out what was wrong with <problem>. It was just <solution>." Josh, always up for discussion and after-work beers...unless they come in non-pint glasses. And, Yong, who is always there to offer feedback, and whose signature laugh brightens up the mood.

From QESST ERC and beyond, I crossed paths with many amazing people that made my time here enjoyable, especially the lunch group, starting with Simone, Ameryc, Tine, Matheau, Laura, and Micheal, joined by Brad, Sebastian, Jake, Pablo, Genevieve, Tara, and Truman, and most recently Rico, Arthur, Nathan, and, of

course, Shannon, who ventured the farthest she's ever been from the Shire, bringing her quiet sense of humor and bold comebacks. Even though it took daily persistence to get everyone to eat lunch together, it was worth the effort to be able to share that time with you. Also, I'd like to thank Ashling for bringing people together for the Short Story Club that inspired insightful discussions.

From my time at EPFL, thank you for the shared times: Dmitry and Luca with whom I worked more closely and shared the joys and desperations of experimental work; and everyone else in the lab who was always ready to discuss and made me feel welcome in (and out of) the lab: Heidi, Martin, Francesca, Andreana, Korbi, Edo, Lea, Mahdi, Marco, Wonjong, Pablo, Pranit, and especially Gözde, Eleonora, and Jelena. A big thank you to my study abroad group—Marta, Thalia, Alex, and David—I am happy I got to share that time with you.

Thanks to my dear friends at ASU. Shirley-Ann, thank you for being a great friend, and your support with dealing with the anxieties of grad school. Natália, thank you for your kindness—I missed having you here these last couple of years.

I'd also like to thank my long-time friends who've remained my support throughout these many years of grad school: Kristina, Kayleigh, Colleen, and Michelle. And, of course, I would like to thank my boyfriend Yannik for his love and support throughout these years, despite the thousands of miles that often separated us.

At the very last, I owe my biggest thanks to my family. I am infinitely grateful for your love and support, and also, for the example you've set for me through your tenacity and humanity.

TABLE OF CONTENTS

LIST OF TABLES

LIST OF FIGURES

Chapter 1

INTRODUCTION

The demand for electricity continues to increase with rising world population and standards of living. From 1974 to 2016, world electricity production nearly quadrupled, at an average annual growth rate of 3.3% [1]. To meet that rising demand requires substantially more energy supply. The current world demand is mostly met through fossil fuels; coal, oil, and natural gas make up 65% of electricity production, with only 5.6% from renewable energy sources[1] [1]. Electricity from solar energy sources, which is the most abundant and distributed form of energy, has the potential to meet the additional demand, while reducing the harmful impacts on human health and the environment from air pollution and green-house gas emissions, the latter leading to rising temperatures and more extreme weather events [2]. Current technology, in the form of photovoltaic (PV) solar cells, is already leading the way in new installed electricity generation capacity to meet the rising demand. At the end of 2017, two-thirds of the added electricity generation capacity came from renewable energy (178 GW), with solar PV expanding the most (97 GW) [3]. A combination of cost reductions and increase in efficiency has led to a significant decrease in levelized cost of electricity (LCOE) for utility-scale solar PV ($0.04-0.06/kWh, reduction of 80-82% from 2010 to 2018)[2] [4], making it cost-competitive with conventional electricity generation (median cost $0.05-0.08/kWh [5]). Keeping pace with rising

[1] includes solar, wind, geothermal, tide, etc.

[2] $0.09-0.12/kWh for commercial-scale and $0.12-0.16/kWh for residential-scale

demand necessitates reduction in material use accompanied with further efficiency improvements.

Most of the solar energy produced today comes from silicon (Si) solar cells, making up about 95% of the market. Since the first practical silicon solar cell was produced in 1954, while significant improvements have been made in efficiency, the basic solar cell design and the choice of material has remained unchanged. Silicon is a convenient choice due to its price and abundance, as well as its high material quality, spurred partly by intense R&D efforts in the computer industry over six decades. However, one disadvantage of Si solar cells (compared to the more expensive GaAs) is poor light absorption: while only a few microns of GaAs are necessary to absorb most of the incoming light, Si needs around 100 μm to do the same. Its indirect bandgap reduces the probability of photon absorption, requiring longer path-lengths to absorb the incoming light. Reducing material costs (due to material quantity and quality), while maintaining efficiency of its thicker counterparts, would necessitate the use of light-management approaches compatible with thinner solar cells to absorb most of the above-bandgap light; at the same time, reduced solar cell thickness decreases the need for long diffusion lengths (i.e. high quality material), further reducing the cost. In terms of applications, thinner, more flexible substrates provide a wider range of possibilities for seamlessly integrating electricity generation into the built environment (i.e. building-integrated PV), as well as greater portability for electricity deployment in remote locations, disaster zones, and space.

The emergence of nanotechnology has brought new possibilities for, among other applications, photovoltaic devices (see Chap. 2). In particular, it has made possible the design and control of light-matter interactions using sub-wavelength features, altering the absorption of light and opening opportunities for new solar cell

geometries and combinations of materials not possible in planar form. Considerable work remains in the understanding and optimization of the material structures and resulting optical properties in the nanoscale regime necessary for accurate tuning of the optoelectronic properties for intended applications, which is the main focus of the present work.

This dissertation provides information on exploiting the unique optical properties of semiconductor nanostructures for reduced optical losses in thin silicon solar cells and silicon-based tandems. Using combined experimental and theoretical approaches, this work explores how the material structure impacts the optical properties for several semiconductor nanostructures, and how those properties can be exploited for improving the optical performance in solar cells. The following chapter introduces different types of semiconductor nanostructures relevant to this work, including a discussion of properties of interest for solar energy applications. Chapter 3 gives an overview of the main experimental and simulation methods used here. The results chapters start with a study of III-V nanowires as active elements of nanowire solar cells in Chap. 4, specifically their recombination mechanisms, through photoluminescence spectroscopy and rate equation analysis. Chapter 5 focuses on the study of silicon nanopillars for reduced optical losses in ultra-thin silicon solar cells through finite-difference optical modeling in comparison with reflectance data. Finally, Chap. 6 presents the main results from the characterization and modeling of nanoparticle-based optical coatings for light management, including a discussion of their tunable physical and optical properties.

Chapter 2

SEMICONDUCTOR NANOSTRUCTURES

This chapter introduces the reader to the different types of semiconductor nanostructures relevant to the present work. The focus is placed on their unique optoelectronic properties of interest to photovoltaics, including scattering, resonant absorption, carrier collection, and light trapping.

2.1 Challenges to overcoming fundamental limits of solar energy conversion

The performance of semiconductor-based solar cells is far below the theoretical maximum thermodynamic efficiency limits of solar energy conversion (~85%)[6]. State-of-the-art structures have reached slightly over 50% of that limit (four-junction solar cells under concentration [7]), while the record single-junction solar cells (state-of-the-art GaAs solar cells[8]) stand at barely 34% of that limit.

In 1961, Shockley and Queisser presented the first paper [9] outlining the limits of solar energy conversion in single-junction solar cells based on detailed balance calculations, setting the theoretical limits for an ideal solar energy converter at 33.7% for a standard AM1.5 spectrum. The positions of the two theoretical maxima corresponded to the bandgaps of 1.1 eV and 1.4 eV (close to the Si and GaAs bandgaps, respectively) [9]. The large discrepancy between the thermodynamic limit and the Shockley-Queisser (S-Q) stems from the loss of energy associated with the thermalization of electron-hole pairs excited by above-bandgap photons, and the lack of absorption of below-bandgap photons. Both Si and GaAs have approached their

respective S-Q limits in state-of-the-art structures (26.3% and 28.8% [8]). Overcoming those limits rests in addressing the assumptions on which the S-Q limit is based: a single-junction material, loss of photons with energy below the bandgap, loss of excess energy of the photons above the bandgap (due to thermalization of photo-excited carriers to the band-edge), and one electron-hole pair generated per photon. Some potential approaches to overcoming these assumptions include multi-bandgap solar cells, multi-exciton generation (MEG) [10–12], intermediate band-gap materials [13], and hot-carrier solar cells [14–16]. Mechanisms involved in some these designs necessitate the use of nanotechnology-based approaches, as they are either weak or non-existant in bulk materials. In addition, nanotechnology also allows for reduced quantity and quality of material through optimization of light absorption using sub-wavelength structures.

2.2 Nanotechnology-based approaches in solar photovoltaics

Nanotechnology refers to technology conducted at the nanoscale, usually with feature sizes between 1–100 nm. Remarkable advances in material synthesis and nanofabrication have allowed for creation of structures with unique properties that arise from their small dimension, setting them apart from their bulk counterparts. Their fundamental material properties (chemical, mechanical, optical, electrical, etc.) are modified, essentially creating a new material. No longer limited by the properties of the bulk material, nanostructured materials can be tuned and optimized for specific properties and applications.

Nanostructures in solar cells can be used to improve photovoltaic performance in a number of ways:

1. overcome the limitation of set material properties in bulk materials (i.e. bandgap engineering)
2. improve mechanisms of carrier generation (i.e. multi-exciton generation)
3. reduction of optical losses
4. design new solar cell architectures that reduce the quantity/quality of material
5. overcome the limitation of combining materials based on lattice-matching

In the present work, improvements in optical performance (3) are considered.

An ideal solar cell structure should be both optically thick (to increase the probability of photon absorption) and electrically thin (to increase the probability of carrier collection). In direct bandgap semiconductors, such as GaAs, where the absorption coefficient is large, and only a few microns are needed to absorb most of the near-bandgap light, the trade-off between those requirements is minimized. Nevertheless, the costs can be reduced by further decreasing the material quantity. On the other hand, indirect bandgap materials such as Si, where solar cell thickness exceeding 1 mm is needed to effectively absorb near-bandgap light, necessitate ways to decrease the volume of solar cell material while increasing the probability of photo-generation.

Light-trapping approaches provide a way to increase the photon flux per unit volume, allowing for a reduction in the quantity of the solar cell material. The optical thickness of the solar cells is effectively increased by extending the path length of light, compensating for the reduced volume. One way to achieve this is using front and back surface texturing to couple light obliquely into the solar cell; this can lead to multiple internal reflections at the boundaries before the light escapes, increasing the probability of photon absorption. In crystalline Si solar cells, random pyramid structures produced through preferential etching of crystallographic planes, are traditionally used to improve light absorption.

The effectiveness of the structures to generate path length enhancement is usually compared to the conventional light-trapping limit. In 1982, Yablonovitch proposed the maximum absorption enhancement factor of $4n^2$ for the weakly absorbed light, achieved through randomization in the angular distribution of light entering the slab [17]. The statistical ray optics approach used in the paper is based on the detailed balancing of light incident on a small area—which undergoes internal angular randomization upon entering the cell—and the light in the loss cone that escapes from it. The derived limit is based on the assumption that feature sizes are large compared to the wavelength of light, and the light interaction with matter is operating in the ray optics regime. Solar absorbers with sub-wavelength features, governed by wave-optics phenomena are not considered, suggesting a potential for exceeding the conventional light trapping limit using nanostructures. Evidence that non-planar solar cells with sub-wavelength feature may exceed the conventional light-trapping limit has been previously investigated through experiment [18, 19], simulation [20], and semi-analytical approaches [21, 22]. Yu *et al.* has suggested that the conventional light trapping limit can be exceeded in grating structures, however, with significant angular dependency. A statistical temporal coupled mode theory developed in the paper was used to describe the combined effect of guided resonances, and compute the resulting theoretical limit [23, 24]. Callahan *et al.* have generalized the assumptions needed to exceed the conventional light trapping limit by designing structures with an elevated local density of optical states (LDOS) — integrated over the absorber region, LDOS must exceed that of its planar counterpart [25]. Optical mechanisms of resonant absorption, light diffraction, and scattering in nanostructures have potential to enhance optical absorption above the conventional light trapping limit.

Information on several semiconductor nanostructures, classified by their geome-

try into nanowires, nanopillars, and nanocrystals, is presented. Nanowires (NWs) are filamentary crystals with high-aspect ratios that enable effective light absorption and novel junction design for light collection. Nanopillars (NPs), on the other hand, have short-aspect ratios, often designed to effectively scatter light with potential for light-trapping. Crystalline nanoparticles, or nanocrystals (NCs), are ultra-fine particles, having (approximately) spherical shape with dimensions between 1–100 nm. The optical properties of NCs (often deposited as thin layers) can be tuned by adjusting their size, composition, density, and arrangement.

The sections that follow provide a brief overview of the optical properties of these semiconductor nanostructures from literature, with a focus on the improvement of optical performance in solar cells through light trapping, scattering, and collection.

2.2.1 Light trapping and scattering

Nanowires can be used for increased light-trapping within the nanowire (used as an active material) as well as in combination with tandem structures (to couple light into the bottom cell). A single nanowire solar cell can even exceed the conventional S-Q limit as a result of the increased absorption cross section [26]. However, if the absorbed cross-section is used in calculating the incident power (instead of the physical cross section), this limit is no longer exceeded. In addition, new geometrical consideration should be taken into account for calculating the S-Q limits [27]. Despite the strong wavelength-dependence of absorption on geometry, arrays of nanowires can also be optimized for absorption over a broad range of wavelengths [28] [shown in Fig. 2.1(a)]; introducing non-uniformity can further increase the light absorption [29] [shown in Fig. 2.1(b)].

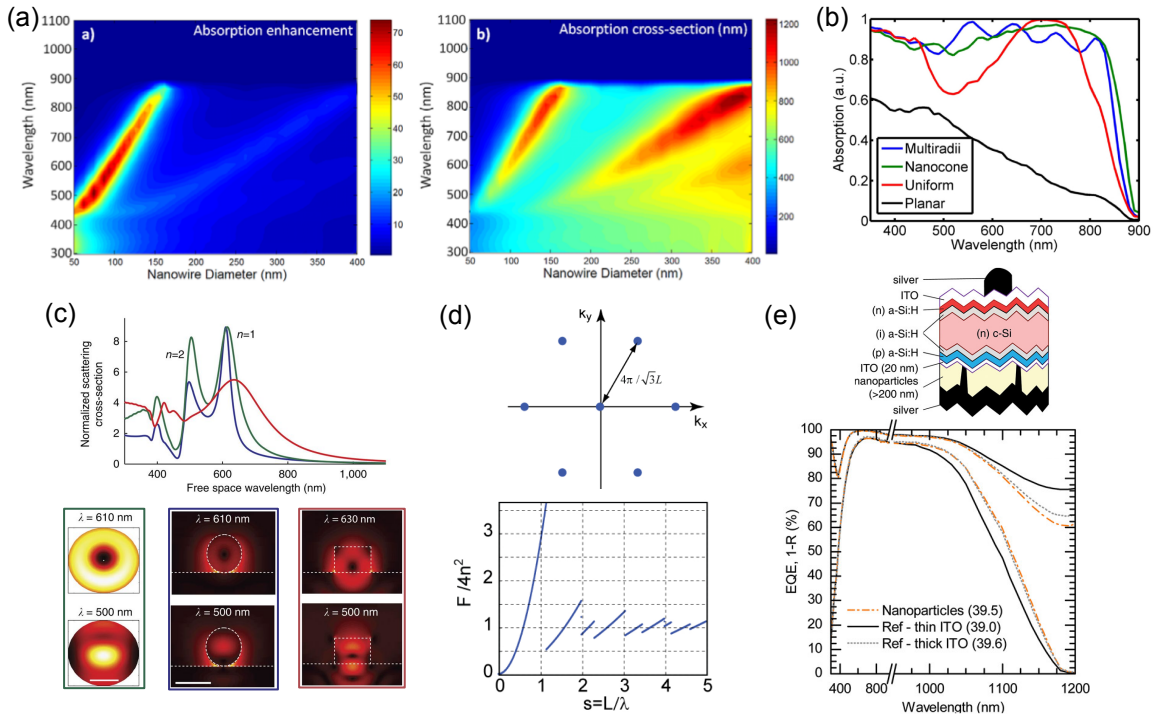

FIG. 2.1: (a) Absorption enhancement in a single GaAs nanowire as a function of wavelength (left) and the corresponding absorption cross-section (right) (Adapted by permission from Macmillan Publishers Ltd: Nanotechnology, Ref. [28], copyright 2014). (b) Nanowire arrays with multiple radii, as well as tapered nanowires (i.e. nanocones), can further boost the broadband absorption of light in the arrays (Adapted from [29]. Optical Society of America, copyright 2014.). (c) Enhanced forward scattering of low-aspect ratio silicon nanopillars (in contact with a silicon substrate) due to leaky Mie resonances. Simulated normalized scattering cross-sections of free-standing silicon spheres (green), silicon spheres in contact with a silicon substrate (blue), and nanopillars of equivalent diameter (red) are shown together with the corresponding electric field energy density at the indicated resonant wavelengths. Leaky Mie resonance is observed for the pillars at the second resonant wavelength (Adapted from [30]. Springer Nature, copyright 2012). (d) Light trapping enhancement for nanopillar arrays having trigonal periodicity. The period (L) of nanopillar arrays enhances the conventional light trapping limit ($4n^2$) by a factor F for a particular wavelength. As L increases to multiples of the wavelength (λ), the light trapping approaches the $4n^2$ limit (Adapted from [23]. Optical Society of America, copyright 2010). (e) Low-refractive-index nanoparticle interlayers for reduced parasitic absorption in metallic rear reflector of solar cells. Schematic of the test structure is shown together with the EQE and 1-R comparing nanoparticle layers to the thin and thick ITO layers (Adapted with permission from Ref. [31]. Copyright 2017 John Wiley & Sons, Inc.).

The implementation of nanoscale features has been investigated for reduced reflection and improved light-trapping in solar cell devices. Spinelli *et al.* [30] demonstrated the broadband reduction in reflectance with the implementation of short-aspect-ratio nanopillar (NP) structures due to strong forward scattering of light. When the size of the scattering structures is comparable to the wavelength of light, the phenomenon is often referred to as Mie scattering. Figure 2.1(c) shows the normalized scattering cross-sections of a free-standing Si sphere (green), a Si sphere on a Si substrate (blue) and a Si cylinder on a Si substrate. The electric field intensity is shown for each case at the first and second resonance for the indicated wavelengths. A broader resonant peak for the third case is observed as the overlap of the Mie resonance inside the cylindrical particle with the substrate, creating a leaky channel [30]. The strong forward scattering of these features suggested that they could also be used in thin solar cells for improved light trapping, where conventional micro-texturing may not be possible (due to feature size). Higher order diffraction would contribute to increased path length of poorly absorbed light (in addition to reduced front reflection) by increasing the likelihood of internal reflectance at the interfaces. To investigate the suitability of Mie scatterers for increased light trapping, Spinelli *et al.* investigated the geometry optimized for front-surface reflectance to investigate the light absorption in 5 and 20 μm-thick silicon solar cells [32], and compared those to the conventional ($4n^2$) limit of light trapping [17, 33]. In the broadband wavelength range, the structures did not exceed the light trapping limit. However, structures optimized for anti-reflection may not be optimized for light trapping. The fundamental limits of light trapping in ordered grating structures suggests that the light-trapping limits may be exceeded for a particular wavelength range [23] [see Fig. 2.1(d)]. For example, the feature geometry can be chosen to optimize light trapping only for the

wavelength regions where the material is poorly absorbing (as opposed to the full wavelength range).

Nanoparticle-based layers can also be used to reduce reflection and increase light trapping, either by providing index matching or increased scattering. The porosity of the nanoparticle layers reduces the effective refractive index of the film, allowing the fabrication of an optical layer between that of air and the constituent material, minimizing the reflective losses at the front surface [34]. Similarly, low-refractive index layers can be used as inter-layers at the metal-semiconductor interface of the back contact to increase reflection and reduce parasitic absorption due to excitation of evanescent waves (that decay along the interface). Increased infra-red response was experimentally demonstrated in single-junction [31] and silicon-based tandems [35] through improved reflectance at the back interface with the implementation of a low-refractive index nanoparticle-based layer. Figure 2.1(e) shows an improved infrared external quantum efficiency (EQE) response of a complete solar cell with the implemented nanoparticle layers; increased reflectance of sub-bandgap light [low 1-reflectance (R)] suggests that the improvement is associated with improved back reflectance of the metal-semiconductor interface [31]. In addition to being used as optical coatings, these nanoparticle layers may also be optimized for scattering: larger scattering angles can increase the path length of poorly absorbing light when placed on the top or bottom of the solar cell (if the particles are non-absorbing). When used as an active material, the scattering centers within the films can be used to increase the light trapping of the nanoparticle structure by randomizing the path of light.

2.2.2 Light collection

The nanowire geometry and resonant absorption of light has permitted new solar cell designs with respect to traditional junction geometry. To perform well, solar cells should be both optically thick (to absorb most of the incoming light) and electrically thin (to reduce carrier losses). If carrier collection and light absorption occur along the same line, the two requirements are at odds. For indirect bandgap materials, such as Si, where near bandgap light is poorly absorbed, high purity is necessary to ensure that carrier losses due to trap-assisted recombination are reduced. The high purity requirements therefore increase the material costs.

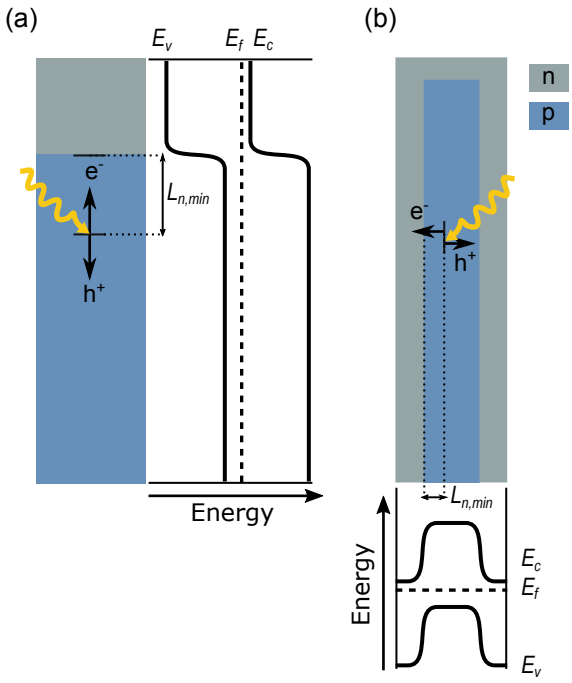

FIG. 2.2: (a) Axial junction vs. (b) radial junction designs for carrier collection in nanowire solar cells. For axial and radial junction designs, carriers are separated along the axial and radial directions, respectively. The radial junction geometry allows for shorter diffusion lengths of the minority carriers (L_n) in the absorber layer (i.e. lower quality materials) [36].

Kayes *et al.* have proposed a radial junction design that orthogonalizes the photon absorption and carrier collection, suitable for implementation in nanopillar and nanowire geometries [36]. Figure 2.2 illustrates the difference between axial junction and radial junction geometries. In the axial junction, light is absorbed and carriers are separated along the axial direction of the NW. For light absorbed far away from the junction (deeper in the material), the minority carrier diffusion length (L_n) must be sufficiently long for carrier collection [Fig. 2.2(a)]. In the radial junction design, light is absorbed along the axial direction, while the carriers are collected in the radial direction. As a result, generated carriers are sufficiently close to the junction at each point along the NW length, placing lower requirements on the L_n, and therefore, a need for high quality material. However, the large surface-to-volume ratio, and the resulting surface recombination losses, increases the dark current, leading to reduced voltage. These losses are better mitigated with radial junction geometries, as shown in Ref. [37] using coupled optical and electrical simulation. Together with enhanced light absorption, implementation of radial junction geometry has the potential to decrease both the required quantity and quality of the semiconductor material, with the potential reductions in costs, especially for more expensive III-V materials.

2.3 Overview of nanostructures used in this dissertation

A brief description of each type of nanostructure studied in this dissertation is provided below, including their description, fabrication, and potential applications in energy generation.

2.3.1 Nanowires

Nanowires are filamentary crystals with a high aspect ratio where the cross-sectional dimension is nanoscale, while the height is unconstrained (typically microscale). Two techniques are mainly used for growth of nanowires: metal-organic chemical vapor deposition (MOCVD) and molecular beam epitaxy (MBE). Nanowires can be grown with both MOCVD and MBE via two main mechanisms: selective area epitaxy (SAE), where a mask pattern determines where on the substrate epitaxy will occur, and vapor-liquid-solid growth (VLS). The mechanisms governing VLS growth were first described by Wagner and Ellis in 1964 for gold-catalyzed silicon filaments [38]. Since incorporation of gold in some semiconductors can lead to degradation of the optoelectronic properties (i.e. increased non-radiative recombination due to deep-level traps), self-catalyzed nanowire growth is a suitable alternative.

Figure 2.3(a) describes the typical (self-catalyzed) VLS process, followed by radial epitaxial growth. In the self-catalyzed growth of GaAs nanowires, gallium droplets that form on an oxidized substrate in the initial stages of gas flow act as catalysts, providing sites for arsenic incorporation; the growth process proceeds with precipitation of GaAs along the droplet interface [39]. Figure 2.3(b) shows an SEM image of an array of GaAs nanowires grown on an oxidized GaAs substrates via the self-catalyzed VLS method, with the Ga droplet still visible at the tip of the nanowire. The nanowire geometry also allows for growing radial shells with modulated doping and composition, important to the development of nanowire-based devices [40]. Directly following VLS growth, and the extinction of the Ga droplet, changes in growth condition (increased As pressure and reduced temperature) allow for radial epitaxial growth to proceed along the surface of the nanowire [schematically shown in the last

step of Fig. 2.3(a)]. As is the case with planar 2D growth, doping and composition can be modulated for different layers in the radial direction. Figure 2.3(c) shows a TEM image of a nanowire cross-section showing their its core-shell structure, fabricated following self-catalyzed VLS growth [41]. The GaAs nanowire structures that will be discussed in this dissertation were fabricated via the VLS method and include radial epitaxial growth (G. Tütüncüoglu and H. Potts grew the samples at the Laboratory of Semiconductor Materials, EPFL, Switzerland).

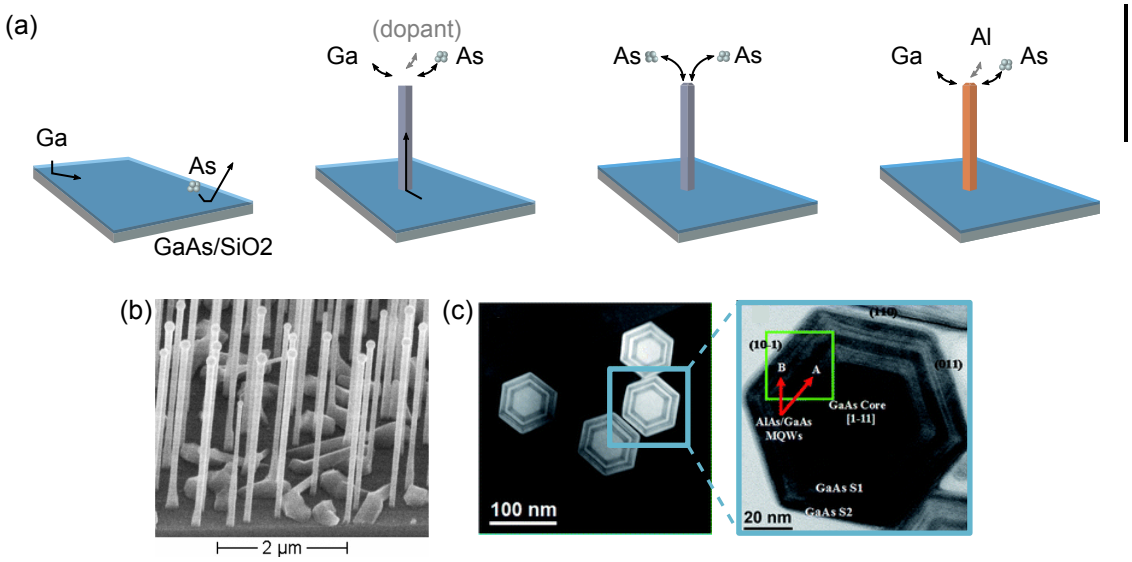

FIG. 2.3: (a) Self-catalyzed VLS growth of a NW. The first step shows the formation of a Ga droplet on an oxidized substrate, followed by NW growth and termination with the extinction of the droplet. Directly following VLS growth, core-shell structures can be formed via radial epitaxial growth. Dopants and alloying materials can be introduced during each stage of growth to modulate the doping and composition in both the axial and radial directions. Image adapted from [42]. (b) SEM image of GaAs NWs grown on an oxidized GaAs substrate via self-catalyzed VLS; the Ga droplet is visible at the tip (Reprinted figure with permission from Ref. [39]. Copyright 2008 by the American Physical Society.). (c) Formation of core-shell structures via radial epitaxial growth following the catalyst-free VLS nanowire growth (Republished with permission of Royal Society of Chemistry, from Ref. [41]; permission conveyed through Copyright Clearance Center, Inc.).

Semiconductor NWs are promising candidates for next generation photovoltaic [26, 43–45] and photocatalytic [46–48] devices due to improved optical properties and unique electrical properties compared to planar devices. The filamentary morphology of NWs increases light absorption for the same quantity of material [28, 29, 49], while the use of radial p-n junctions reduces the need for long diffusion lengths (i.e. high purity materials) for carrier collection [18, 36, 50]. The NW geometry also makes it possible to overcome the limitation of combining materials based on lattice matching [51], as well as realize advanced concept solar cell structures with improved mechanisms of carrier generation (i.e. multi-exciton generation) [10–12], reduction of thermalization losses (i.e. hot-carrier solar cells) [14–16], and introduction of multiple energy levels (i.e intermediate bandgap solar cells) [13]. These mechanisms offer pathways to overcoming the Schockley-Quisser (S-Q) limit of efficiency [9, 52], as discussed earlier. In terms of cost, the use of less expensive silicon substrates may decrease the large substrate costs associated with the growth of III-V materials [53, 54]. Today, the experimental efficiency of NW-based devices has improved rapidly in recent years (15.3% for GaAs [55] and 17.8% for InP in 2017 [56]), although still below their planar counterparts that already approach their respective Shockley-Queisser limits [8]. Their fabrication also relies on expensive nanolithography techniques and substrates. To reduce these costs, NWs should be fabricated via a bottom-up approach on unpatterned foreign substrates (i.e. c-Si). In order to ensure comparable performance to their patterned, metal-catalyzed counterparts, requires understanding the potential loss mechanism in NW-based GaAs solar cells at different scales: from a collection of NWs in the array to a single diode, down to the quality of the starting material.

Mikulik *et al.* have previously studied the photovoltaic performance of individual

NWs in the array, and the impact of inhomogeneity between them on the performance of the full solar cell device using conductive-probe atomic force microscopy [57]. Among the individually measured NWs, however, even the highest performing NWs showed relatively low open-circuit voltage (0.6 V). Understanding the underlying physical limitations and providing meaningful simplified models are the first step to improving their photovoltaic performance.

A major challenge to utilizing bottom-up, self-catalyzed NWs is the presence of wurtzite (WZ)/zincblende (ZB) polytype defects along their length. The unintentional phase change along the length of the NW is believed to arise due to the local temperature and source-flux variations at its growth interface [58]; recent *in-situ* observations of phase-switching during growth has given additional insight on its mechanisms and ways to control it [59]. The main concern is the impact these polytype defects may play in reducing the performance of a NW-based device. To predict the expected device performance requires a model that can capture (and simplify) complex carrier dynamics of an ensemble of crystalline defects. The interface between the WZ and ZB phases of gallium arsenide (GaAs) exhibits a type-II band offset, first computed theoretically [60–62], that has been since corroborated experimentally. Nanowires containing WZ/ZB polytype defects have been previously studied via transmission electron microscopy and photoluminescence (PL) spectroscopy [63–67] including direct correlation of structural and optical properties along the full length of the nanowire by Heiss et al. [68], suggesting an ensemble of localized states of varying confinement resulting from the type-II offset between the WZ and ZB phases. Time-resolved PL studies further suggest different recombination rates for polytype regions compared to the band-to-band [63, 69].

In Chap. 4, we analyze the various recombination mechanisms in self-catalyzed

GaAs NWs through spectroscopic measurements coupled with a rate equation model to help describe the results. As shown in Fig. 2.4, photo-generated carriers recombine through various radiative channels due to crystal variations along the wire (at bandgap and sub-bandgap energies) as previously illustrated in [69], while their proximity to the surface makes them susceptible to non-radiative recombination through surface traps, depleting the photo-excited carriers in the proximity of the surface [70]. When observing only bandgap recombination, the two effects of carrier relaxation are not readily separable: (1) recombination due to surface traps and (2) thermalization to lower energy levels from which they radiatively recombine. The individual energy levels are coupled and have well-defined relaxation rates, giving rise to the observed PL intensities.

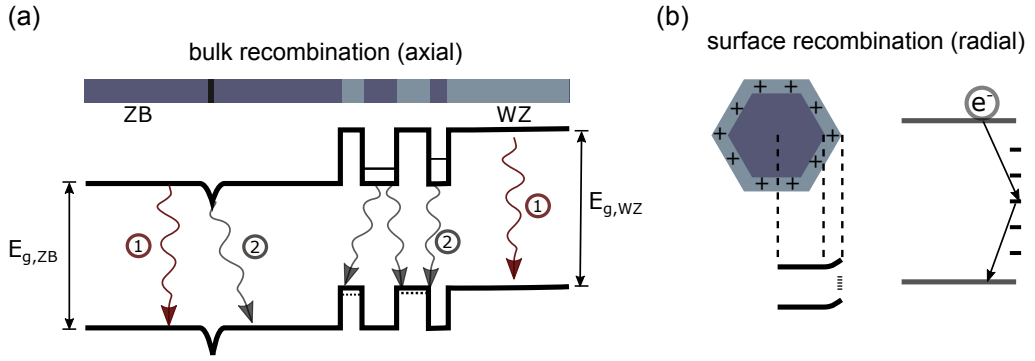

FIG. 2.4: (a) Crystal variations along the wire give rise to ① bandgap and ② sub-bandgap radiative transitions while being subject to (b) surface recombination in the radial direction.

In this dissertation, time-resolved photoluminescence spectroscopy (TRPL) and power-series time-integrated photoluminescence spectroscopy (TIPL) is used to assess relaxation rates and the dominance in intensity for different transitions in GaAs NWs (bandgap, polytype regions, and defects) in Section 4.2, and utilize a rate equation model to help describe the observed variation in spectroscopic features as a

function of photon energy for various illumination intensities and temperatures in Section 4.3.

2.3.2 Nanopillars

Nanopillars usually refer to the short-aspect-ratio nanostructures, in which both the cross-sectional dimension and the length are nanometer scale (on the order of 100 nm). Nanopillars are most often fabricated using top-down, etching techniques, such as reactive ion etching (RIE) [71] and metal-assisted chemical etching (MaCE) [72]. Prior to etching, the substrates are patterned via one of the lithography techniques. Several alternatives to e-beam lithography have emerged, such as nanosphere and nanoimprint lithography, that have allowed relatively inexpensive, large-area nanopatterning of substrates [73–75].

Figure 2.5(a) provides a work-flow for fabricating low-aspect ratio nanopillars based on silica nanosphere (SNS) lithography. SNS are spin-coated onto a silicon substrate forming a monolayer. An SEM image of a coated substrate [Fig. 2.5(b)] shows near-uniform arrangement of SNS and trigonal periodicity [75]. The period of the fabricated structures is determined by the initial size of the SNS. The nanospheres are then reduced in size through RIE prior to the deposition of a metal catalyst. SNS size reduction can be tuned, producing nanopillars with different diameter sizes. The SNS particles are removed prior to etching. An SEM image of three metal-patterned silicon substates are shown in Fig. 2.5(c), where the SNS were reduced to three different sizes. Following the MaCE step, the metal catalyst is removed. An SEM image of the fabricated NP structures [Fig. 2.5(d)] shows the NP arrays having comparable periodicities where the diameter is tuned through SNS reduction

[76]. The Si nanopillar structures that will be discussed here were fabricated via silica nanosphere (SNS) lithography and MaCE, as described in Ref. [76] (J.Y. Choi fabricated the samples at the Solar Power Labs, Arizona State University, USA).

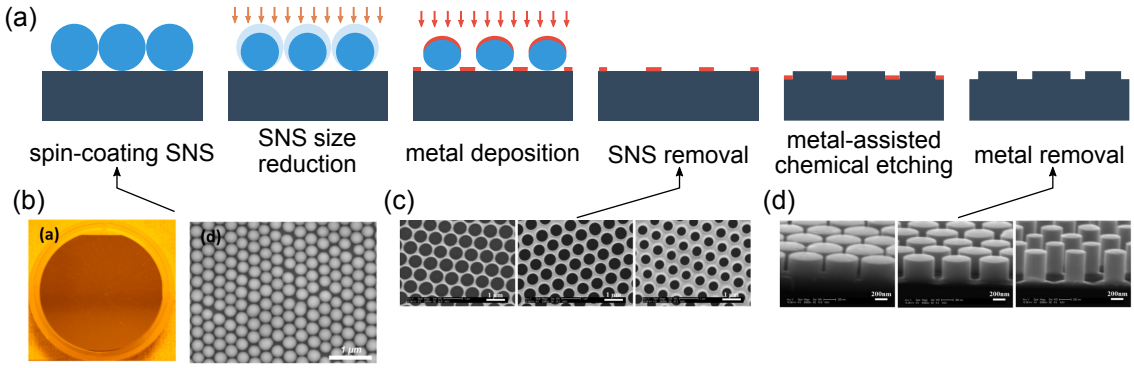

FIG. 2.5: (a) SNS lithography and MaCE for fabrication of large-area nanopillar arrays. Period of the nanopillars is controlled by the initial size of the deposited SNS and their thickness by SNS size reduction with RIE. (b) SNS-coated substrate is shown after spin-coating deposition with the SEM image showing the trigonal periodicity arrangement of SNS (Adapted with permission from Ref. [75]. Copyright 2014 American Chemical Society.) (c) SEM images showing metal-patterned silicon substrates following metal deposition and SNS removal for three different SNS size reductions. (d) Images of the corresponding nanopillar structures following MaCE and metal removal (Adapted with permission from Ref. [76]. Copyright 2015 American Chemical Society.).

The optical property of semiconductor nanopillars, of particular interest to photovoltaics, is the strong forward scattering of light that results in reduced front surface reflection and enhanced light trapping [30, 32] of the nanostructured substrate. The strong forward scattering of light occurs when the cross-sectional dimension of the nanopillar (d) is on the order of the wavelength of light (λ): $d \approx \lambda$. This behavior was first described by the Mie theory in 1908 [77]. In thick silicon solar cells, pyramid texturing is used to alter the angle of normally incident light as it enters the substrate - this ensures that light is internally reflected multiple times before exiting the cell. For ultra-thin silicon substrates (25 μm or less), 5–10 μm pyramidal textures

may not be feasible. Spinelli *et al.* had already demonstrated broadband reduced reflection due to short-aspect ratio pillars using a square lattice arrangement through experimental measurements and simulation [30]. However, Yu et. al., using a theoretical approach, have argued that hexagonal (or trigonal) periodicity can achieve a higher maximum enhancement factor over the bulk $4n^2$ limit resulting from the sub-wavelength diffraction grating geometry [23].

In Chap. 5, the optical properties of hexagonally-arranged silicon nanopillar arrays for potential applications in reducing optical losses in ultra-thin silicon solar cells are investigated. The scattering behavior of the nanopillars was investigated using the finite-difference solver for different nanopillar geometries [78]. In addition, the potential of these nanostructures for light trapping is investigated: rigorous-coupled wave-analysis (RCWA) was used to study the impact of the nanopillars on the higher order diffraction with visualization of the fields using finite-difference frequency-domain solver in Ref. [79].

2.3.3 Nanoparticles

Nanoparticles have structural dimensions usually between 1–100 nm. Crystalline nanoparticles may also be referred to as nanocrystals (NC). For very small NCs (1-10 nm), quantum confinement effects emerge, shifting the fundamental band gap of the material to higher energies, thus altering their optical and electrical properties compared to that of bulk materials. In addition, silicon NCs even have high luminescence despite bulk silicon being an indirect bandgap material. This phenomenon was first observed in porous silicon [82], which garnered greater interest for silicon NCs. Semiconductor NCs are fabricated by a variety of processes: (1) mechanical grinding,

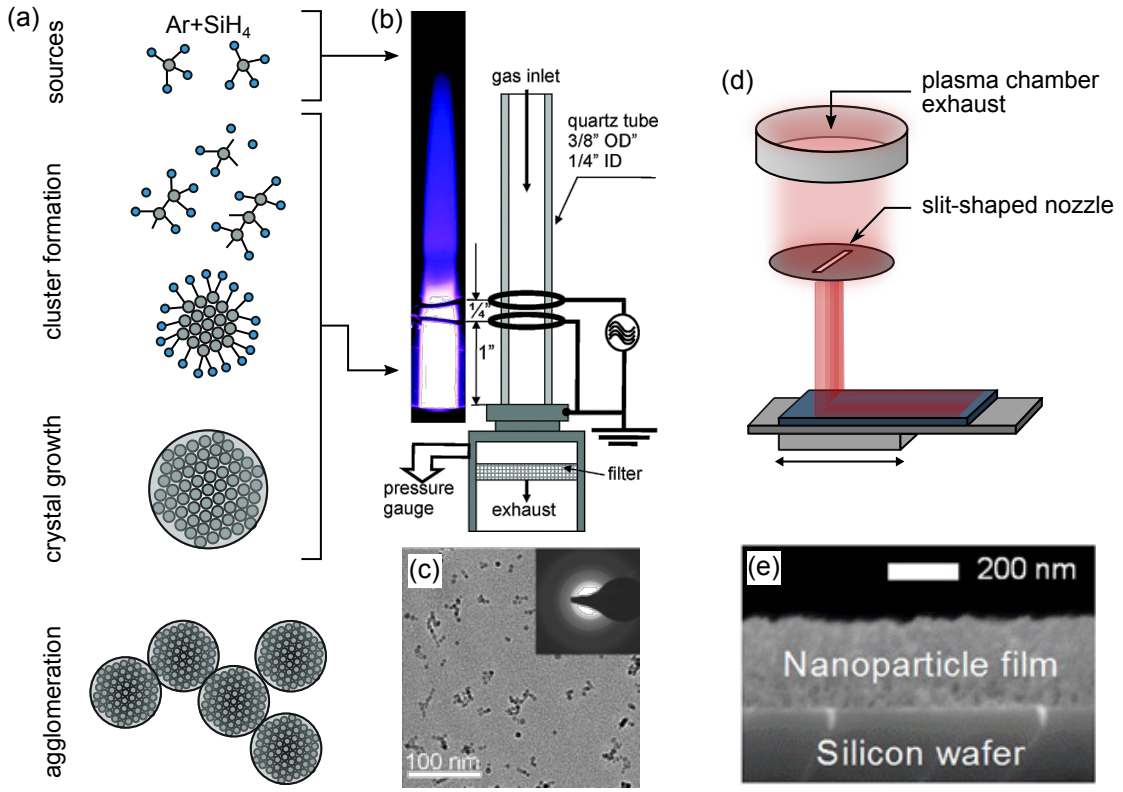

FIG. 2.6: (a) Gas-phase plasma process schematic for silicon nanoparticle production. Silane gas dissociates into ions that rapidly form clusters and continue to grow through aggregation of ions, forming silicon nanoparticles. The nanoparticles agglomerate as they exit the plasma zone due to weak van-der-Waals interactions. (b) Schematic of the RF plasma reactor used in the synthesis of silicon nanoparticles. (c) TEM image of the produced particles with the average size of 5.7 nm. (Adapted with permission from Ref. [80]. Copyright 2005 American Chemical Society). (d) Plasma chamber exhaust can be adapted with a slit-shaped nozzle; combined with a movable substrate stage, uniform, large area nanoparticle-based films are produced [81]. (e) SEM X-section image of silicon nanoparticles grown in layers, forming a porous thin film (Adapted with permission from Ref. [31]. Copyright 2017 John Wiley & Sons, Inc.).

(2) pyrolisis, (3) RF plasma, (4) sol-gel, and (5) self-assembly via Stansky-Krastinov growth process [83]. The silicon NCs investigated in this dissertation were fabricated via the non-thermal RF plasma method [80, 81]. Figure 2.6(a) shows a simplified process of gas-phase NC formation in the plasma, starting with dissociation of the silane

gas (SiH_4), followed by the clustering of the dissociated products into primary particles. The particles continue to grow through aggregation of dissociated products before exiting the plasma zone. As the particles exit the plasma zone, they tend to agglomerate due to weak Van-der-Waals forces. Figure 2.6(b) shows a schematic of the plasma reactor, with an accompanying digital image of the argon-silane plasma. Radio-frequency power is applied to the two copper ring electrodes attached to the quartz tube chamber through which the gas sources continuously flow [80]. A TEM image of the deposited NCs is shown in Fig. 2.6(c). The plasma chamber exhaust can be adapted with a slit-shaped nozzle with increased control over the NCs deposition with respect to density and uniformity of the deposited film across large areas [81]. Figure 2.6(e) shows an SEM image of a nanoparticle-based thin films deposited through the impaction of silicon nanocrystals following plasma synthesis (density ~30%). The density of the resulting films can be tuned by varying the speed of NC impaction on the substrate by adjusting the nozzle-to-substrate distance [31]. The NC-based films studied here were fabricated in this way (P. Firth deposited the films in the Holman Lab, Arizona State University, USA).

Introducing porosity in semiconductor materials can alter their properties, including those related to quantum confinement, surface chemistry, and light propagation, for applications such as anti-reflection coatings, mirrors, etc. Porous silicon (PS) thin films, chemically etched into their native crystalline Si substrate, have been the subject of intense research, with potential applications in light-emitting devices [82], solar cells [34, 84, 85], sensors [86], and biomaterials [87]. Nanoparticle deposition offers a "bottom-up" approach to the realization of porous silicon thin films. The nanoparticle films can be deposited on a variety of substrates and with high through-

put [80, 81]. Their physical and chemical properties can be tuned by controlling the size and arrangement of nanoparticles during deposition [88].

Boccard *et al.* recently demonstrated the use of low-refractive-index nanoparticle layers for reducing optical losses in solar cells, specifically the reduction of parasitic absorption at the metal-semiconductor interface of a back reflector [31]. The low-refractive index layer between the semiconductor and the metal: (1) increases the reflectance at the semiconductor edge (before it reaches the metal) and (2) ensures that the light that reaches the metal is incident at an angle closer to the normal, reducing losses due to evanescent waves. As a result, the lowest possible refractive index (closest to n=1) would be ideal. However, high-porosity low-refractive index films performed worse than expected; the best experimental results were demonstrated using a dense Si nanoparticle film (n=1.53). The discrepancy between the theoretical results, where films were approximated as homogeneous, and the experimental were attributed to the increased surface roughness of the more porous nanoparticle films; metal deposited on rougher surfaces, specifically sub-wavelength roughness, was previously shown to increases absorption in metal due to stronger plasmonic effects [89]. The effect of layer inhomogeneity on the performance of the optical layers was not considered.

In Chap. 6 the impact of porosity and pore-size distribution on the optical properties in nanoparticle-based films is investigated in connection with controlling optical losses in Si solar cells as discussed above. We study the physical properties of these films as a function of n_{eff}, and correlate those to their scattering intensities. We experimentally demonstrate increased scattering with increased average pore size and pore-size distribution, and show good agreement to the simulated data.

Chapter 3

METHODS

The main experimental and simulation methods used in this thesis are described here. A brief overview of optical characterization techniques are presented, including photoluminescence spectroscopy and spectrophotometry. Then, full-wave optical simulation method based on finite-difference is briefly described. Finally, structural characterization techniques based on effective medium approximation and BET nitrogen absorption are provided.

3.1 Photoluminescence

Photoluminescence (PL) arises from spontaneous emission of photons resulting from photo-excited electron-hole recombination, primarily in direct bandgap semiconductors. Following photo-excitation, usually with a pump laser having photon energy above the bandgap, an electron is excited from the valance to the conduction band, creating an electron-hole pair. In the simplest case, carriers thermalize to the band-edge and recombine across the bandgap, emitting a photon at an energy of approximately $E_{g,direct}$ of the semiconductor. In addition to band-to-band transitions, PL spectra can reveal more complex energy transitions that arise from localized or continuum impurity and defect levels, if those transitions are radiative.

The PL set-up used in the experimental measurements performed in Chap. 4 of this thesis, is schematically represented in Fig. 3.1. The blue lines represent the laser light, which is used to optically excite the carriers in the semiconductor sample. The

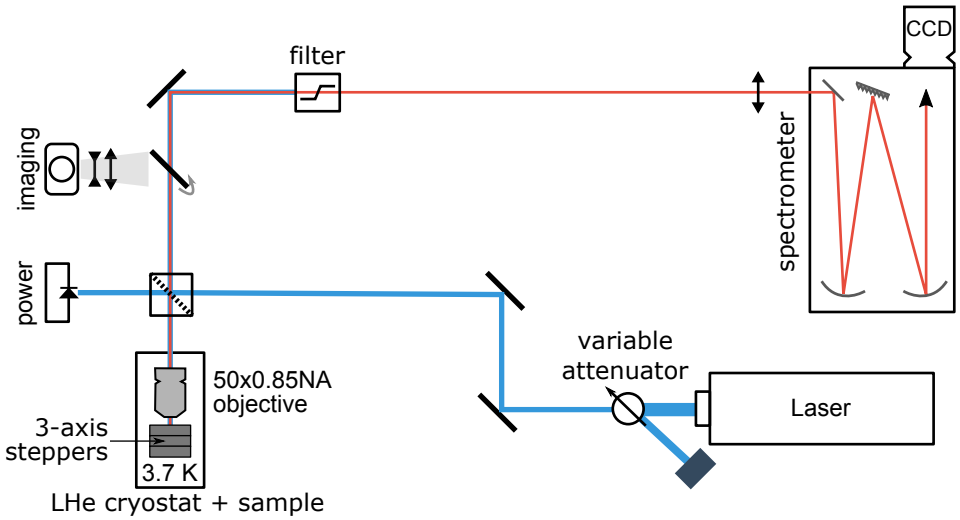

FIG. 3.1: Simplified schematic of a PL set-up. The blue and red lines represent the laser beam and PL signal respectively. Adapted from [42].

power of the laser is adjusted using a variable optical attenuator close to the laser output. The laser light is then partially reflected on the beam-splitter: transmitted light is monitored by the power meter, while the reflected light leads to the closed-loop liquid helium (LHe) cryostat (stage temperature of 3.7 K), where a sample is mounted onto a stage with a 3-axis stepper. In the cryostat, the laser light is focused by a microscope objective, usually high magnification and high numerical aperture, to provide sub-micron resolution.

The PL signal emitted by the sample is filtered from the reflected laser light using a high-pass filter. The PL signal is then directed to a grating spectrometer. Grating periods of 300, 600, and 1200 l/mm are chosen depending on desired wavelength resolution. The dispersed light is then directed to a silicon charge-coupled device (CCD) to detect the signal, which is then converted to wavelength-dependent intensity. Additional details on the PL set-up used here can be found in Ref. [42].

3.1.1 Time-correlated single photon counting

Time-correlated single-photon counting (TCSPC) is a powerful tool for determining the recombination rates for radiative transitions in a sample. The basic principle consists of quickly populating the excited levels (using a short intense laser pulse) and monitoring the emitted PL intensity as a function of time. The time-resolved PL intensity profile of the emitted light is collected over multiple cycles of excitation and emission using a periodic laser pulse.

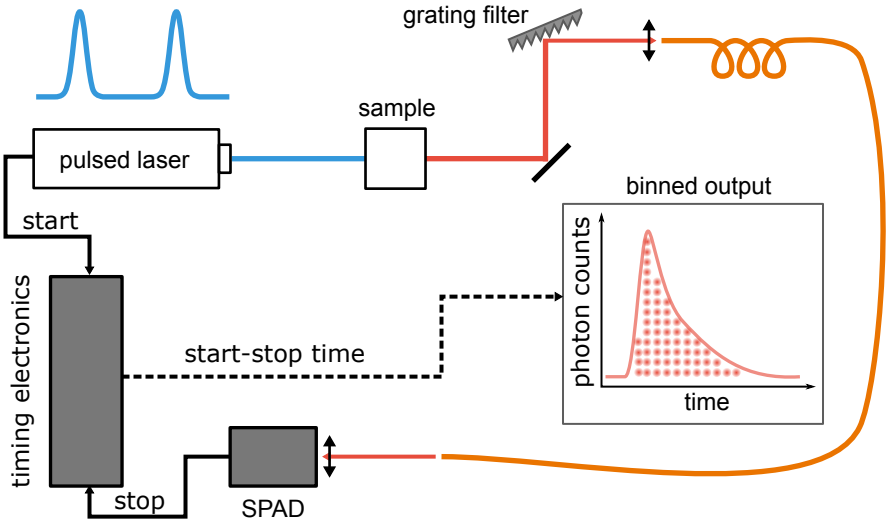

FIG. 3.2: Measurement set-up schematic for lifetime measurements based on TCSPC. Pulsed laser light with defined repetition rate excites the carriers in the sample. Each pulse triggers the "start" time (via an electrical pulse). The PL signal from the sample is filtered using a monochromator and coupled to an optical fiber. The light from the optical fiber is coupled to the silicon photo-avalanche diode (SPAD), and the detected photon triggers the "stop" time. The start-stop times are then binned, generating a histogram, which is analogous to the probability of single-photon emission with respect to the elapsed time.

The TCSPC method is based on the repetitive, precisely-timed detection of single photons from a PL signal [90]. Figure 3.2 provides a simplified schematic of the

TCSPC set-up. The laser signals the emission of an optical pulse, triggering the start channel of the timing card. The pulsed laser (blue), with predefined repetition rate, excites the sample. The PL signal (red) is spectrally filtered using a grating and focused onto a fiber end, limiting the bandwidth of the signal. The output of the fiber is then focused onto a silicon photo-avalanche diode (SPAD), triggering the stop channel of the timing card. The start-stop times are bin-casted and a histogram is generated, which represents the time-evolution of the PL signal. The extent to which the histogram accurately captures the time-evolution of the PL signal depends on the instrument response function (IRF), which arises from timing uncertainties of individual components in the system, as well as careful consideration of the laser power and repetition rate parameters [91].

Here, the excitation source is a Q-switched diode laser operating at 475 nm, with a pulse full-width half-max (FWHM) between 70 and 120 ps (depending on excitation power). The repetition can be adjusted between 2.5 and 40 MHz, set to allow the PL signal to decay before the new laser pulse is generated. Detection is preformed with silicon photo-avalanche diodes (SPADs) with a timing jitter between 30 and 40 ps [42]. The intensity of the laser is also kept sufficiently low to reduce artifacts (i.e. undercount of photon events due to pile-up) by keeping the detection rate on the SPAD at most 1–5% of the excitation rate [91].

A decay model can be fit to the histogram in order to obtain the lifetime(s) of the optical transition(s). In addition, if the measured response approaches the instrument resolution, the effect of the measurement set-up becomes increasingly more important and must be taken into account. The measured signal is the convolution of the actual signal with the IRF (in this case with respect to time t):

$$I_{meas}(t) = I(t) \circledast IRF(t) \tag{3.1}$$

The IRF signal can be obtained by recording the time-evolution of the laser signal (i.e. reflected from the substrate) at the same laser intensity and repetition rate at which the measurements are performed. Figure 3.3 shows the IRF signal for the TRPL measurements performed in Chap. 4. The IRF signal places a limit on the decay rates that can be measured. The measured signal [$I_{meas}(t)$] is then fitted to the convolution of the IRF, and the expected decay model of the signal [$I(t)$], to obtain the fitting parameters [i.e. radiative decay lifetime(s)].

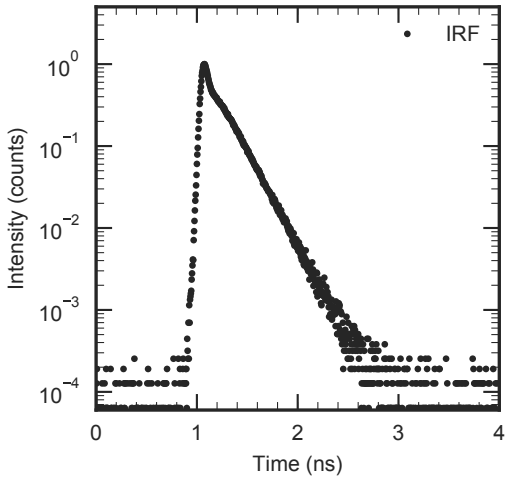

FIG. 3.3: Measured instrument response function (IRF) used for the fit of the deconvolution of the time-resolved signal.

3.2 Spectrophotometry

3.2.1 Transmission haze

Transmission haze is a measure of scattering for light passing through a transparent medium. The presence of irregularities within the medium (i.e. air voids) or at the surface (i.e. roughness) may cause some light to deviate from its direct path, either diffusing in all directions or within a narrow cone (depending on the size of the structures).

The definition of transmission haze is the proportion of the diffuse light ($T_{diffuse}$) to the total transmitted light (T_{total}). This definition is captured in the equation below:

$$\%Haze = \frac{T_{diffuse}}{T_{total}} \times 100 \tag{3.2}$$

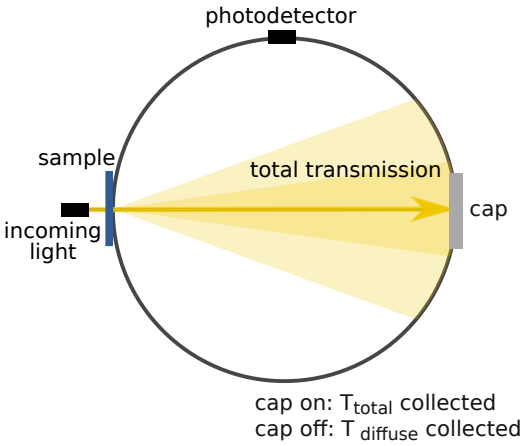

FIG. 3.4: Measurement set-up schematic for obtaining transmission haze.

There are two different methods of measuring haze: (1) using a hazemeter and (2) using a spectrophotometer [92]. While there are differences in the equipment

used, the measurement principles are similar. Both methods include a collimated light source, an integrating sphere with entrance and exit ports, and a photodetector. A simple schematic of the measurement set-up is shown in Fig. 3.4.

T_{total} is measured with the exit port closed, capturing all of the transmitted light; $T_{diffuse}$ is measured with the exit port open, allowing the "direct" portion of the transmitted light to escape. The measurements performed here used a Perkin-Elmer spectrophotometer with an integrating sphere.

3.2.2 Angular intensity distribution

Angular intensity distribution (AID) measurements provide the relative intensities of either transmitted or reflected light, resolved by the angle of detection. The measurement captures both the direct and scattered components as the light is reflected from or transmitted through a sample. This method further supplements the haze measurements by providing the angles along which the light scatters together with their respective intensities, as opposed to only the total scattered intensity.

The AID can be measured using the automated reflectance/transmittance analyzer (ARTA), an accessory to the spectrophotometer [93]. The procedure is as follows: (1) collimated light from the spectrophotometer is incident on the sample, parts of it being reflected/transmitted/scattered, (2) the detector, set to a particular angle, collects the light passing the entrance port of its integrating sphere and converts it to intensity, and (3) the user-defined detector angles and corresponding intensities are tabulated. It is important to note that the detector only collects the light in the horizontal plane. In addition, due to the geometry of the set-up, the detector cannot measure the intensities of angles between -12 degrees and $+12$ de-

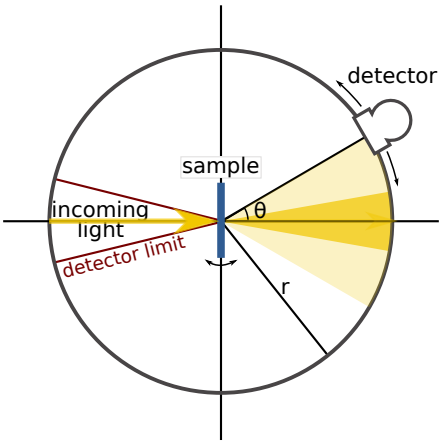

FIG. 3.5: Measurement set-up schematic for obtaining the angular intensity distribution.

grees as they are blocked by the light source post. However, the user can specify arbitrary angles of incidence. Figure 3.5 shows a schematic of the ARTA set-up with its components specified.

3.3 Full-wave optical simulation

3.3.1 Basic principles

To simulate the optical properties of semiconductor nanostructures, the optical simulation method must be able to capture the wave optics phenomena present in the nanoscale regime. The finite-difference time-domain (FDTD) method is a simple grid-based full-wave solver based on Maxwell's equations able to handle arbitrary nanostructured geometries [94, 95]. The method can be used to determine transmittance and reflectance spectra and field patterns resulting from the interaction of the source and the structure.

Maxwell's equations describe the interactions of the electric ($\boldsymbol{E}$) and magnetic($\boldsymbol{H}$) fields with each other, and in the presence of matter and sources:

$$\frac{d\boldsymbol{B}}{dt} = -\nabla \times \boldsymbol{E} - \boldsymbol{J}_B \tag{3.3}$$

$$\boldsymbol{B} = \mu \boldsymbol{H} \tag{3.4}$$

$$\frac{d\boldsymbol{D}}{dt} = \nabla \times \boldsymbol{H} - \boldsymbol{J} \tag{3.5}$$

$$\boldsymbol{D} = \varepsilon \boldsymbol{E} \tag{3.6}$$

where $\boldsymbol{B}$ and $\boldsymbol{D}$ are the magnetic induction and the electric displacement, whose quantities are related to $\boldsymbol{H}$ and $\boldsymbol{E}$ via material properties: the permeability μ and permittivity ε, respectively. $\boldsymbol{J}_B$ and $\boldsymbol{J}$ are the (fictitious) magnetic-charge current density and the electric-charge current density — these quantities are used to specify sources in the simulation. Instead of specifying a particular incident electric/magnetic field, "equivalent" current sources are used in the simulation [96, 97].

Figure 3.6 shows a simplified schematic representing the evolution of electric and magnetic fields in a so-called Yee cell [94]. In dispersive materials (i.e. where permittivity or permeability is a function of frequency), the time-evolution of fields becomes more complex.

3.3.2 Dispersive materials

Materials are represented in Maxwell's equations via their relative permittivity ε and permeability μ. The following analysis will focus on non-magnetic materials ($\mu \approx 1$). A material whose permittivity is frequency-dependent is called dispersive. Microscopically, their behavior arises from the relative motion of (small, negatively

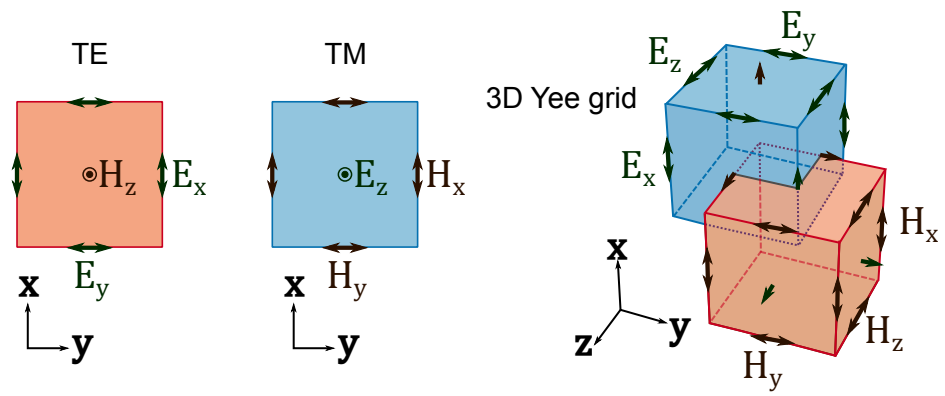

FIG. 3.6: Evolution of electric and magnetic fields in 2D shown for transverse electric (TE) and transverse magnetic (TM) modes for a single cell and in 3D, along a Yee grid. (Image adapted from FDominec [license: CC BY-SA 4.0], from Wikimedia Commons).

.

charged) electrons to the (large, positively charged) nucleus in response to the frequency of the applied electric field, which causes the electrons to oscillate. This motion of electrons in the medium can be described using a harmonic oscillator driven by an electric field (i.e. Lorentz oscillator model). Solids with ionic bonding have an additional (ionic) contribution to the permittivity that arises due to the relative displacement between positive and negative ions in response to the applied field.

Material dispersion is accounted for in the simulation with the addition of a frequency-dependent polarization density $\boldsymbol{P}$, defined as the density of dipole moments arising from the displacement of electrons in the material in response to the applied electric field. Equation 3.6 is then expanded to:

$$\boldsymbol{D} = \varepsilon_0 \boldsymbol{E} + \boldsymbol{P} \tag{3.7}$$

where ε_0 is the permittivity of free space. The polarization of the material does not instantaneously respond to the applied field (i.e. the polarization is time-dependent). As a result, a set of auxiliary fields $\boldsymbol{P}_n$ (for each resonance n) is stored and evolved

in the simulation along with the $\boldsymbol{E}$ field in order to keep track of the polarization.

$$\boldsymbol{P} = \sum_n \boldsymbol{P}_n \tag{3.8}$$

$$\frac{d^2\boldsymbol{P}_n}{dt^2} + \gamma_n \frac{d\boldsymbol{P}_n}{dt} + \omega_n^2 \boldsymbol{P}_n = \sigma_n \omega_n^2 \boldsymbol{E} \tag{3.9}$$

where γ_n is the damping constant, ω_n is the resonant frequency, and σ_n is the strength of the n^{th} resonance. The permittivity $\varepsilon(\omega)$ of a material can be modeled as the sum of any number of Lorentz terms (subject to memory and time requirements to perform the simulation):

$$\varepsilon(\omega) = \varepsilon_\infty + \sum_n \frac{\sigma_n \omega_n^2}{\omega_n^2 - \omega^2 - i\omega\gamma_n} \tag{3.10}$$

where ε_∞ is the high-frequency permittivity.

Permittivity of a material is related to the refractive index (n) and the extinction coefficient (k). If n and k are known for a particular material, one can compute the permittivity to obtain a fit to the $\varepsilon(\omega)$.

$$\begin{aligned} \varepsilon &= \widetilde{n}^2 \\ &= (n - ik)^2 = (n^2 - k^2) - i2kn \end{aligned} \tag{3.11}$$

Here, we primarily consider the optical properties of silicon in the FDTD simulations. The fitting parameters for the permittivity of silicon (approximated with three Lorentz terms) are obtained from Ref. [98], which provide excellent agreement to experimental data from Ref. [99].

3.3.3 Frequency-domain solver

A common frequency-domain problem in electromagnetism is to find fields produced in a structure in response to a source at a constant frequency, ω. Unlike in the

time domain, this method is based on Fourier transforming Maxwell's equations into a system of linear equations, and solving them iteratively. This can be achieved using the finite-difference frequency-domain (FDFD) method [100]. However, in the simulation software used here, instead of using a full FDFD solver, the frequency-domain solver is implemented within the FDTD environment. The FDTD timestep is used directly to iteratively solve for the frequency-domain response, by treating the time-step as an abstract linear operation. As a result, the features within the FDTD solver are also readily available in the frequency-domain implementation [97].

The simulation proceeds by specifying a continuous wave source at a specific frequency. The material properties are set using the real part of $\varepsilon(\omega)$ and electrical conductivity $\sigma_D(\omega)$ parameters, which can be computed from the n and k. One specifies the electrical conductivity instead of the imaginary part of $\varepsilon(\omega)$ to avoid storing complex fields (halving computational memory and time requirements), according to the relationship $\mathrm{Im}(\varepsilon) = \varepsilon_\infty \sigma_D / \omega$.

3.3.4 Simulation set-up

The choice of the computational domain size and resolution needs to be first taken into account, thus limiting the size of the structure being simulated. Implementation of boundary conditions — e.g. perfectly-matched layers (PMLs) and periodic boundary conditions (PBCs) — serve to reduce the size of the computational domain. PMLs are absorbing boundary conditions that minimize (ideally, eliminate) reflection at the boundaries of the computational domain by "matching" the impedance (defined as $Z = \sqrt{\frac{\mu}{\varepsilon}}$) of the PML to the simulation region and its materials. Their implementation serves to simulate problems with open boundaries. Berenger first

proposed the PML approach in FDTD simulations [101], and since then, several related reformulations have emerged. Simulations performed here employ a variation of uniaxial PML (UPML) [102] (first proposed by Sacks *et al.* [103]), where the formulation is based on an artificial anisotropic absorbing material. While small reflections will always arise in practice due to discretization, in certain cases (e.g. inhomogeneous media at the PML boundary), PML may fail altogether; in this case, adiabatic absorbers (with gradually turned on absorption profile) are recommended [104]. Implementation of PBCs is another way to truncate the computational domain: if the structure has translational symmetry in some direction, one would simulate only the unit cell with the PBCs specified in that direction. With plane wave illumination at normal incidence, PBCs simply copy the fields at one edge of the computational domain and place them at the opposite edge. For illumination at an angle, however, the fields in adjacent periods are not exactly periodic, but rather phase-shifted. The Bloch boundary conditions correct for this phase-shift by multiplying the field components by $e^{i\,\boldsymbol{k_{bloch}}\cdot a}$ where $\boldsymbol{k_{bloch}}$ is the Bloch wavevector and a is the length of unit cell (i.e. period) in that direction [105].

Setting up the simulation requires specifying the geometrical structure, material properties, light source, boundary conditions, and data collection monitors (Fig. 3.7). The FDTD simulation presented here were performed using MEEP, an open-source FDTD software package, which also contains a frequency-domain solver [97].

3.3.4.1 Reflectance and transmittance flux spectra

The FDTD method provides a way to investigate the reflectance and transmittance flux as a function of the frequency of incident light. A single time-domain

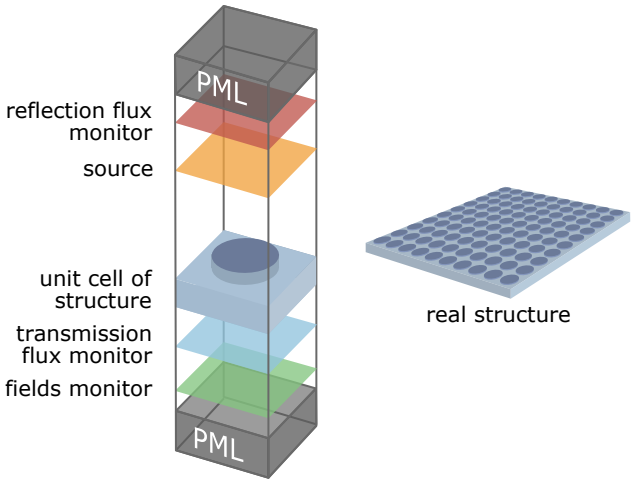

FIG. 3.7: FDTD simulation set-up, shown here for periodic structures.

.

simulation can solve for power for a range of frequencies by Fourier transforming the response to a short pulse. The integral of the Poynting flux is used to compute the power at each frequency:

$$P(\omega) = \Re \oiint_S E_\omega(x)^* \times H_\omega(x) dA \tag{3.12}$$

To compute reflectance and transmittance spectra requires running two sets of simulation: reference and structure, with incoming and outgoing fluxes computed for each simulation. The transmittance flux is then computed as the ratio of the transmitted power and the reference power as:

$$T(\omega) = \frac{P(\omega)_{out}}{P(\omega)_{ref}} * 100 \tag{3.13}$$

For reflectance, the reflected power is the sum of the incident and reflected power. As a result, the incoming power is subtracted from the reference before the ratio is taken:

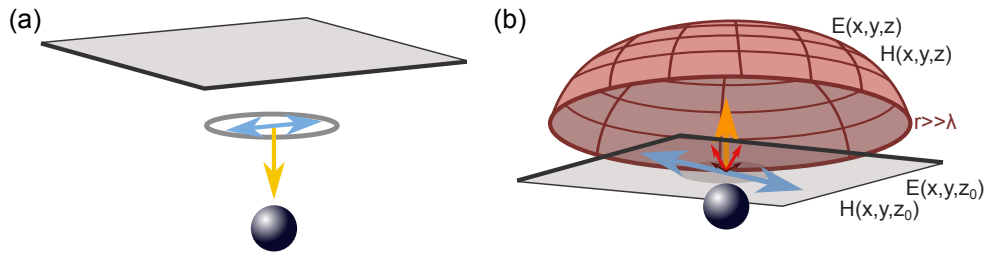

FIG. 3.8: (a) Schematic showing incident fields and a scattering object (b) Scattered fields recorded on the "near" surface — E(x, y, z_0) and H(x, y, z_0) — inside the computational domain are used to calculate propagating fields E(x, y, z) and H(x, y, z) beyond the plane, assuming a homogeneous material.

.

$$R(\omega) = \frac{P(\omega)_{ref} - P(\omega)_{in}}{P(\omega)_{ref}} * 100 \tag{3.14}$$

3.3.4.2 Near-to-far-field transformation

Despite the small size of the computational domain (in this case, $\approx 1\ \mu m$ or less), field-patterns can be computed far away from the source (at the distance $r >> \lambda$) using near-to-far-field transformation (NTFFT) [100]. The near-field is complicated, containing both evanescent and propagating waves — NFFFT is performed to eliminate the near-field evanescent components. The remaining propagating waves are a better approximation to our experimental measurements where detectors are placed far away from the sample and only propagating waves are detected. The NFFFT is based on replacing the fields at the "near" surface (inside the computational cell) with equivalent sources and analytically propagating them to the far-field region [106]. Figure 3.8 is a simplified schematic of the NTFFT. The fields recorded on the near field monitor $E(x, y, z_0)$ and $H(x, y, z_0)$ are transformed to equivalent current sources.

These are then propagated to a distance $r >> \lambda$, assuming that the medium is homogeneous. The angular dependence can be captured by computing the fields along a hemisphere surface. The propagating fields are calculated for each frequency. The power for each frequency (and at each point along the hemisphere surface) is computed using Eq. 3.12.

The dimensions of the near-field monitor used for the projection can affect the accuracy of the projected far-fields. Due to the assumption that the EM fields are zero beyond the edge of the monitor, the fields are truncated at the monitor edge (an alternative being making the monitor region, and thus the simulated domain, impractically large). When the dimensions of the monitor are on the order of the wavelength of light, the monitor acts like an aperture, causing strong diffraction, making these projections limited. This is true even if periodic conditions are used. To reduce the diffraction effects, phase corrected sums for multiple periods m can be calculated in post-processing, knowing the E-fields from a single period $\boldsymbol{E}_0$:

$$\boldsymbol{E}^{far} = \boldsymbol{E}_0^{far} \sum_m e^{i(\boldsymbol{k_{in\text{-}plane}})\cdot m \cdot a} \tag{3.15}$$

where m is the period number, N is the total number of periods, and a is period length. The phase corrected sums can be applied in one or both in-plane directions, for 2D and 3D simulations, respectively.

3.3.4.3 Validation of boundary conditions

Boundary conditions in the reduced simulation domain were validated using known sources and structures. Figure 3.9 shows the results of the FDTD simulation for planar c-Si structure using a plane-wave source at normal incidence, with

n and k values, and corresponding Lorentz-Drude fit parameters, taken from literature [98, 99]. The computational domain is reduced to 600 nm x 600 nm for in-plane directions, and periodic boundary conditions implemented. The perfectly matched layers are included in the vertical directions to eliminate back reflectance. Figure 3.9(a) demonstrates good agreement between analytically computed transmittance, reflectance, and absorptance to FDTD-simulated values. Electric field energy density profile of the simulation domain cross-section is shown in (b), with the dashed line indicating the top surface of c-Si.

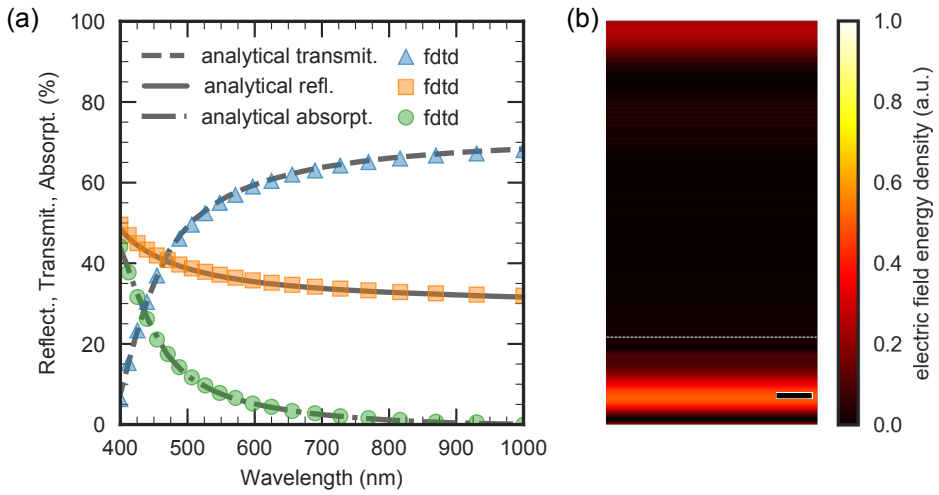

FIG. 3.9: (a) Analytically-computed vs. FDTD-simulated reflectance, transmittance, and absorptance of planar c-Si substrate (b) Electric field energy density in the cross-section of the computational domain. The scale bar corresponds to 100 nm.

.

The in-plane dimensions of the computational domain also influence the far-field profiles. As previously mentioned, when the size of the near-field monitor is on the order of wavelength of light, light will diffract as it passes through the monitor, leading to broad profiles and diffraction peaks. If the structure is simulated as periodic, broadening can be reduced using phase-shifted sums of the E-fields from a single

period, Eq. 3.15. Figure 3.10 shows the far-field corrections for normally-incident light in air using simulated data (shown for a single period, m=1); as the number of periods increases from 1 to 100, the profile becomes narrower to better approximate normally incident light. To confirm the accuracy of the phase-shifted sums, larger computational domains, corresponding to m=2, 4, and 8, are also simulated; the obtained data (circles) is in good agreement with the computed phase-shifted sums.

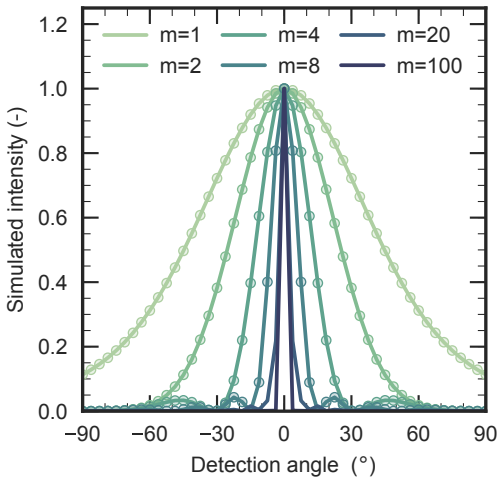

FIG. 3.10: Far-field corrections for normally-incident light in air using phase-shifted sums with m periods. Simulated data using larger computational domains (corresponding to m=2, 4, and 8) are shown for comparison.

.

3.4 Characterization of structural properties in non-periodic media

3.4.1 Effective medium approximation

Ellipsometry is a commonly used technique for determining the optical constants of thin films: the refractive index (n) and extinction coefficient (k). It measures the change in polarization of reflected (or transmitted) light that arises from the

interaction of incident light with the material. A model is then chosen to fit the measured data and obtain the best approximation for n and k.

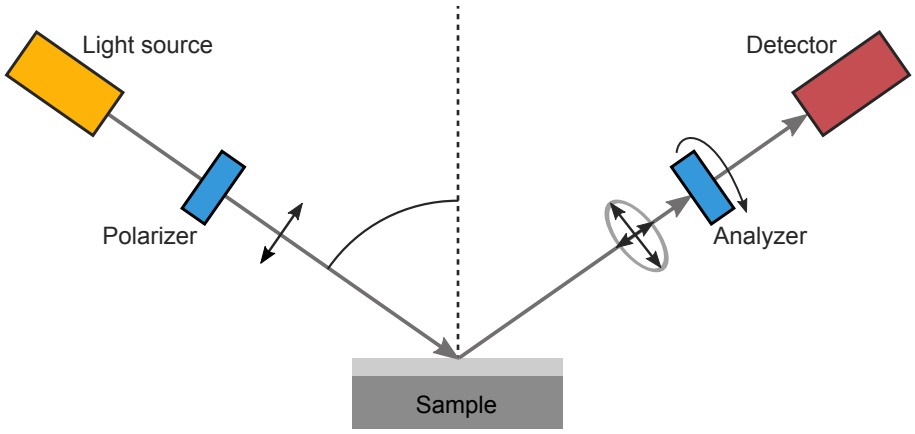

FIG. 3.11: Schematic of an ellipsometry set-up. (Image adapted from Buntgarn, at the English Wikipedia project [license: CC BY-SA 3.0])

.

Figure 3.11 provides a simplified schematic of an ellipsometry set-up. The incident light source is linearly polarized before being incident on the sample. The polarization of the reflected light is captured using a rotating analyzer (a polarizer), with transmitted light incident on the detector. The ellipsometry data provides the ratio of the reflected p-polarized (parallel to the plane of incidence) r_p and s-polarized light (perpendicular to the plane of incidence) r_s, represented in terms of an amplitude (Ψ) and the phase difference component (Δ):

$$\frac{r_p}{r_s} = tan(\Psi)e^{i\Delta} \tag{3.16}$$

The ellipsometry method is an indirect measurement technique. The derivation of n and k is based on the chosen dispersion model.

While the method is best suited for characterizing homogeneous films, it can

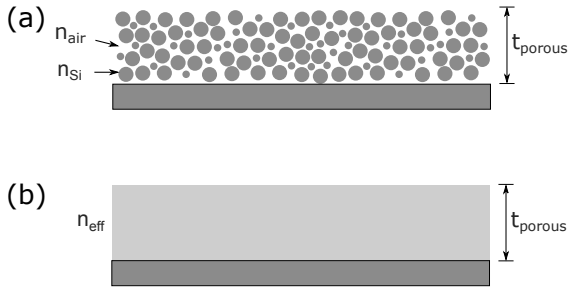

FIG. 3.12: (a) Schematic of a porous nanoparticle-based film and (b) a representative homogeneous film with effective optical properties (i.e. n_{eff}), which are measured with ellipsometry.

.

also provides the effective properties of some heterogeneous materials (i.e. porous media). Figure 3.12(a) provides a schematic of a porous nanoparticle-based film consisting of nanoparticles surround by air, with optical properties n_{Si} and n_{air}, respectively. Ellipsometry measurements provide the film's effective optical properties [n_{eff}, shown in (b)], which are related to their relative fractions; if the optical properties of the constituent materials are known, a suitable model can be used to extract them.

Several models have been developed to estimate the structural composition of heterogeneous films from the effective refractive index (n_{eff}) obtained from ellipsometry measurements. These effective medium approximation (EMA) models provide a mathematical description of a heterogeneous medium based on the optical properties and relative fractions of its components. The EMA model was first proposed by Bruggeman [107] in 1935, considering polydisperse spheres in a continuous medium [108, 109]. The resulting equation proposed therein relates n_{eff} of the medium to the optical properties (n_i) and relative fractions (f_i) of its components:

$$\Sigma f_i \frac{n_i^2 - n_{eff}^2}{n_i^2 + (d-1)n_{eff}^2} = (1 - f_{Air}) \frac{n_{c\text{-}Si}^2 - n_{eff}^2}{n_{c\text{-}Si}^2 + 2n_{eff}^2} + f_{Air} \frac{1 - n_{eff}^2}{1 + 2n_{eff}^2} = 0 \tag{3.17}$$

where d is the dimensionality factor.

To reduce the effect of the potential changes in absorption properties for bulk and nano-materials (i.e. bandgap narrowing), the porosity is determined for the wavelength regions where absorption is negligible.

3.4.2 BET porosity analysis

The BET surface area and porosity analysis techniques estimate the total area, cumulative pore volume, and pore distribution from gas adsorption in porous media. The analysis is based on the Brunauer-Emmett-Teller (BET) theory that aims to explain how gas molecules are physically adsorbed on a solid surface in multilayer form [110]. The theory, first developed in 1938, forms the basis for estimating the surface area in both non-porous and porous materials. In 1951, Barrett, Joyner, and Halenda expanded on this seminal work, developing a model for determining the pore volume and area distributions in porous media [111], known as the BJH model.

A suitable analysis technique is often chosen based on the pore size (d_{pore}) in the material. The International Union of Pure and Applied Chemistry (IU- PAC) classifies the pores as microporous (d_{pore} < 2 nm), mesoporous (d_{pore} = 2–50 nm) and macroporous (d_{pore} > 50 nm) [112]. The BJH model is suitable for pore size analysis of mesoporous and macroporous materials. However, the accurate pore size analysis in micropores often relies on density functional theory (DFT) and molecular simulation methods (i.e. Monte Carlo). In addition, for smaller mesopores (< 10 nm), numerical methods can provide more accurate results [113].

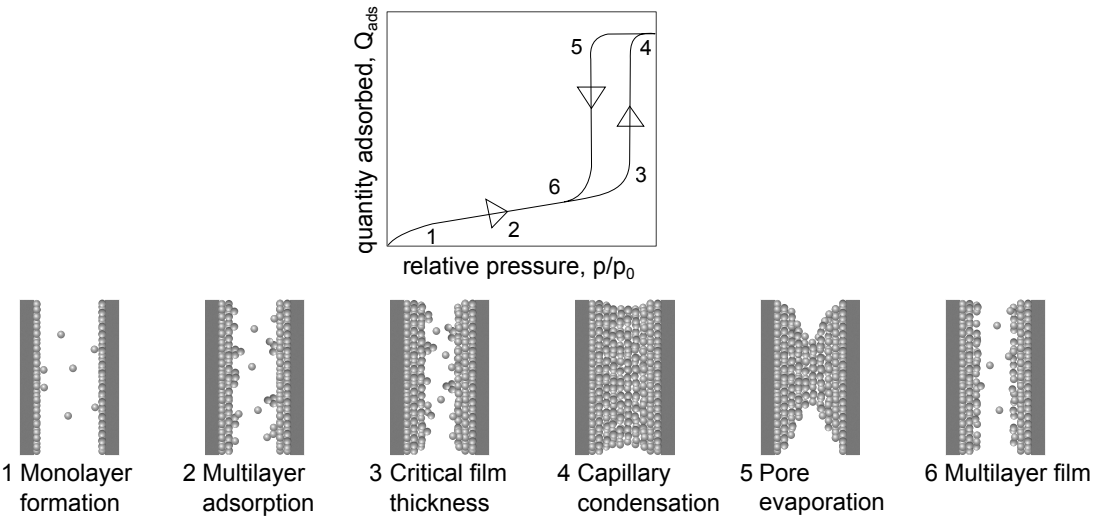

FIG. 3.13: Pore filling mechanisms in mesopores and how they relate to the adsorption isotherm (adsorbed volume (Q_{ads}) as a function of relative pressure (p/p_0). Image adapted from [114].

The appropriate analysis techniques are applied to the measured data: the adsorbed amount as a function of pressure, performed at constant temperature. The resulting curve is often referred to as the adsorption isotherm, forming the basis for both surface area and porosity analysis discussed above. Figure 3.13 shows the origins of the different features in the isotherm corresponding to stages of the pore filling process. In most cases, nitrogen (N_2) gas (at its boiling temperature of 77 K) is used as the adsorbate due to its non-reactivity; carbon dioxide and argon gas are used in certain cases. The adsorbed amount is usually measured by volumetric (manometric) methods - the amount of adsorbate removed from the gas phase is determined by changes in pressures. (Additional details on the experimental set-up can be found in ref. [115]). Figure 3.14 shows a simplified schematic of the set-up. A sample holder is first immersed into a liquid nitrogen dewar. Helium gas, (which is non-adsorbing) is then introduced to determine the void volume of the sample tube. Following helium gas evacuation, nitrogen gas is introduced into the sample holder

(its pressure and temperature recorded prior to opening the sample port) and allowed to adsorb into the sample until equilibrium is reached. The quantity adsorbed (Q_{ads}) is determined from quantity dosed minus any residual nitrogen remaining in the sample tube. The pressure is incrementally increased using an injection piston until the saturation pressure of nitrogen (p_0) is reached. The acquired data — Q_{ads} as a function of relative pressure (p/p_0) — is then analyzed. The measurements performed here used the Micrometrics Tristar II 3020.

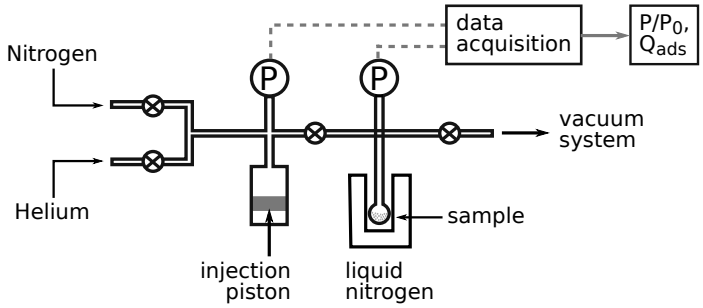

FIG. 3.14: BET porosity analysis measurement set-up for obtaining gas adsorption isotherms.

Chapter 4

CHARACTERIZATION AND MODELING OF III-V NANOWIRES AS ACTIVE ELEMENTS OF NANOWIRE SOLAR CELLS

In this chapter, recombination mechanisms in polytype gallium arsenide (GaAs) nanowires (NWs) are studied through photoluminescence measurements coupled with rate equation analysis. Polytype NWs exhibit switching between zinc-blende (ZB) and wutrzite (WZ) crystal phases along the wire due to rotational twinning during self-catalyzed growth. When photons are absorbed in polytype NWs, electrons and holes separate: in the simplest case, electrons quickly thermalize to the band-edge of the ZB phase, while holes thermalize to the band-edge of the WZ phase, recombining indirectly in space across the type-II offset. The recombination mechanisms of this system are investigated experimentally through time-resolved photoluminescence (TRPL) at liquid helium temperature, and time-integrated photoluminesence (TIPL) at various temperatures, for the baseline case of AlGaAs capped GaAs NWs. The effects of the surface recombination on sub-bandgap transitions are also investigated using Al_2O_3 and no capping at the surface. The inference is made that carriers quickly thermalize to the spatially closest, lowest energy level, where they radiatively recombine across a sub-bandgap energy gap at a slower radiative rate than band-to-band. Finally, a rate equation model is used to investigate different configurations of polytype defects along the wire, including the effects of the surface and temperature, which compares well with experiment considering spatially indirect recombination between different polytypes, and defect-related recombination due to twin planes and other defects.

4.1 Experimental details

4.1.1 Sample growth and preparation

The GaAs NWs were grown by molecular beam epitaxy (MBE) system via the gold-free gallium-assisted vapor-liquid-solid (VLS) mechanism on GaAs $(1\bar{1}1)$B substrates coated with thin SiO_2 (all of the NW samples discussed here were grown at the Laboratory of Semiconductor Materials, EPFL, Switzerland). Two unintentionally doped samples were grown under similar conditions with and without the AlGaAs shell. Both samples were first grown axially by the VLS method, with an estimated 70 nm diameter. Then, the samples were thickened with an epitaxial GaAs shell (60-65 nm) to reduce the surface-to-volume ratio of the nanowires, allowing for better optical probing of the "bulk-like" properties of polytype NWs. The first sample was then capped with an AlGaAs/GaAs epitaxial shell, while the second sample was capped with a 10 nm As capping layer to prevent oxidation of the GaAs surface. This thin layer of As was removed prior to measurements to either add the Al_2O_3 via atomic layer deposition (ALD), or to use the NW sample as a reference. The resulting three sets of samples were used in the measurements: AlGaAs-capped, Al_2O_3-capped, and bare (As-decapped) GaAs NWs.

For the PL measurements, the nanowires were transferred onto polished silicon (Si) substrates. The three nanowire samples were first sonicated in isopropyl alcohol to detach the wires from their native substrate. The resulting solution was then deposited and allowed to dry, leaving behind the nanowires electrostatically attached to the silicon substrate.

4.1.2 Photoluminescence characterization

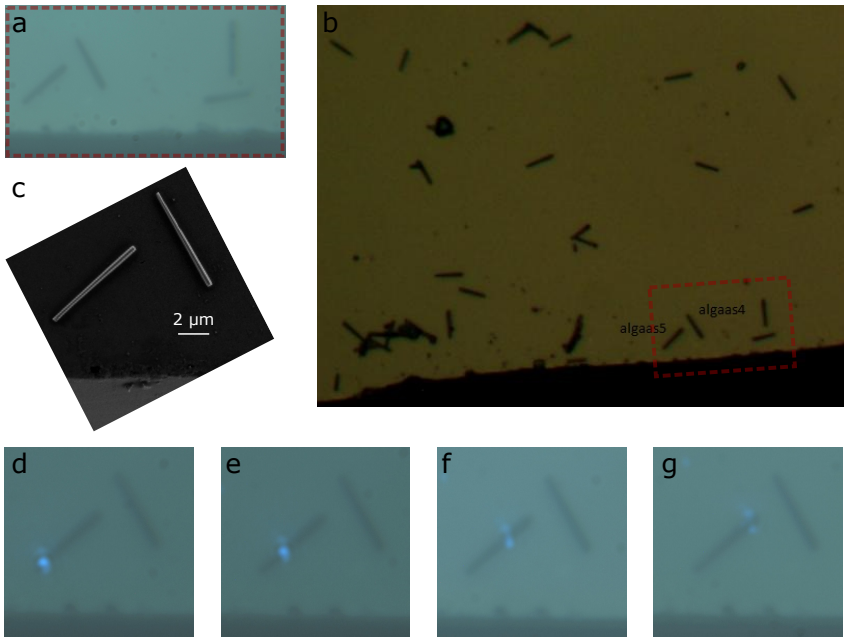

FIG. 4.1: (a) Image from the cryostat projected onto the camera showing GaAs NWs lying on the silicon substrate. (b) Optical microscope image of the sample following completion of measurements to locate the NWs of interest. (c) SEM image of the NWs to determine their orientation (i.e. tip and bottom of the NW) and correlate the position to the PL measurement. (d)–(g) The laser spot in relation to the NW for one set of measurements performed.

The TIPL measurements were performed using a low-temperature micro-PL set-up consisting of a highly-stable (transverse vibration < 10 nm) closed-loop helium cryostat (T≈3.7K) with an internal low-working distance, high numerical aperture (NA) apochromatic cryo-compatible objective together with a wide-field, white-light imaging [42]. With NA of 0.85 and pump-laser wavelength of 632.8 nm, sub-micron laser spot size is achieved, estimated as 2x Rayleigh criterion (∼ 900 nm). Figure 4.1(a) shows the projected image from the cryostat on a flat substrate. Following

the measurements, we locate the NWs on the substrate using the optical microscope [Fig. 4.1(b)]. The SEM image allows us to determine the orientation of the NW (i.e. tip and bottom of the NW) [Fig. 4.1(c)] and correlate the relative laser spot position along the NW to the observed PL. Figures 4.1 (d)–(g) show the laser spot at four different positions along the NW for one of the samples; in Fig. 4.2 (a) below, PL measurements were taken with a continuous-wave red laser at these four positions along the NW. The laser spot is positioned at a desired location using a piezoelectric actuator. Using a circular variable neutral density filter in front of the laser output, the incident power on the sample was varied logarithmically for up to 20 different powers from 6.83 nW to 70.1 μW. A quarter-waveplate ($\lambda/4$) is used to generate circularly polarized light incident on the sample.

The TRPL measurements were performed using a picosecond diode laser (with $\lambda = 475$ nm and FWHM of 70–100 ps at a repetition rate of 5 MHz). The emission from the sample was filtered using a reflection grating that directs the desired bandwidth of light onto a fiber end leading to the silicon photo-avalanche diodes (SPAD) for time-correlated single photon counting (TCSPC). The grating filter combined with the optical fiber limits the collected signal to a bandwidth of around 5–10 meV, ensuring that only the desired wavelength corresponding to a peak of interest is measured.

For temperature-dependent TIPL, the temperature was varied with a heater in contact with the sample holder inside the cryostat from 3.7K to 200K for 12 temperatures varied logarithmically. At each temperature, power-dependent measurements were taken for up to 20 different power levels to monitor the peak evolution.

4.2 Results

4.2.1 Time-integrated PL and TEM

The study begins by correlating the structural properties along the wire to the TIPL of the AlGaAs-capped NW sample. This correlation allows us to confirm that the variation observed in the PL signal along the wire is related to the crystal variation, as previously observed [68]. Figure 4.2(a) shows the power-series PL taken at four points along the wire. The corresponding transmission electron micrograph (TEM) of a representative NW sample grown under similar conditions is shown in Fig. 4.2(f). For these samples, the bottom end of the nanowire [in (g)] is mostly ZB with few twinning defects, while the tip of the wire [in (h)] has short ZB/WZ segments. The middle region of the wire shows a high density of twinning defects.

Looking at the AlGaAs-capped nanowires, the evolution of peaks in the PL along the wire suggests a continuous and discontinuous density of states for the tip and bottom of the NW, respectively, as shown in Fig. 4.2(a). At the tip of the NW for low power, the presence of discrete peaks across a range of energies is observed. With increasing power, lower energy peaks start to dominate in intensity before blue-shifting as the radiative recombination energy approaches the bandgap of GaAs of 1.519 eV (calculated for intrinsic GaAs at 3.7K). This behavior suggests a saturation of the shallower higher energy radiative channels giving way to deeper lower energy radiative channels. For the bottom of the nanowire, the presence of discrete peaks (as is the case for the tip of the nanowire) is not observed, and the broad peak continu-

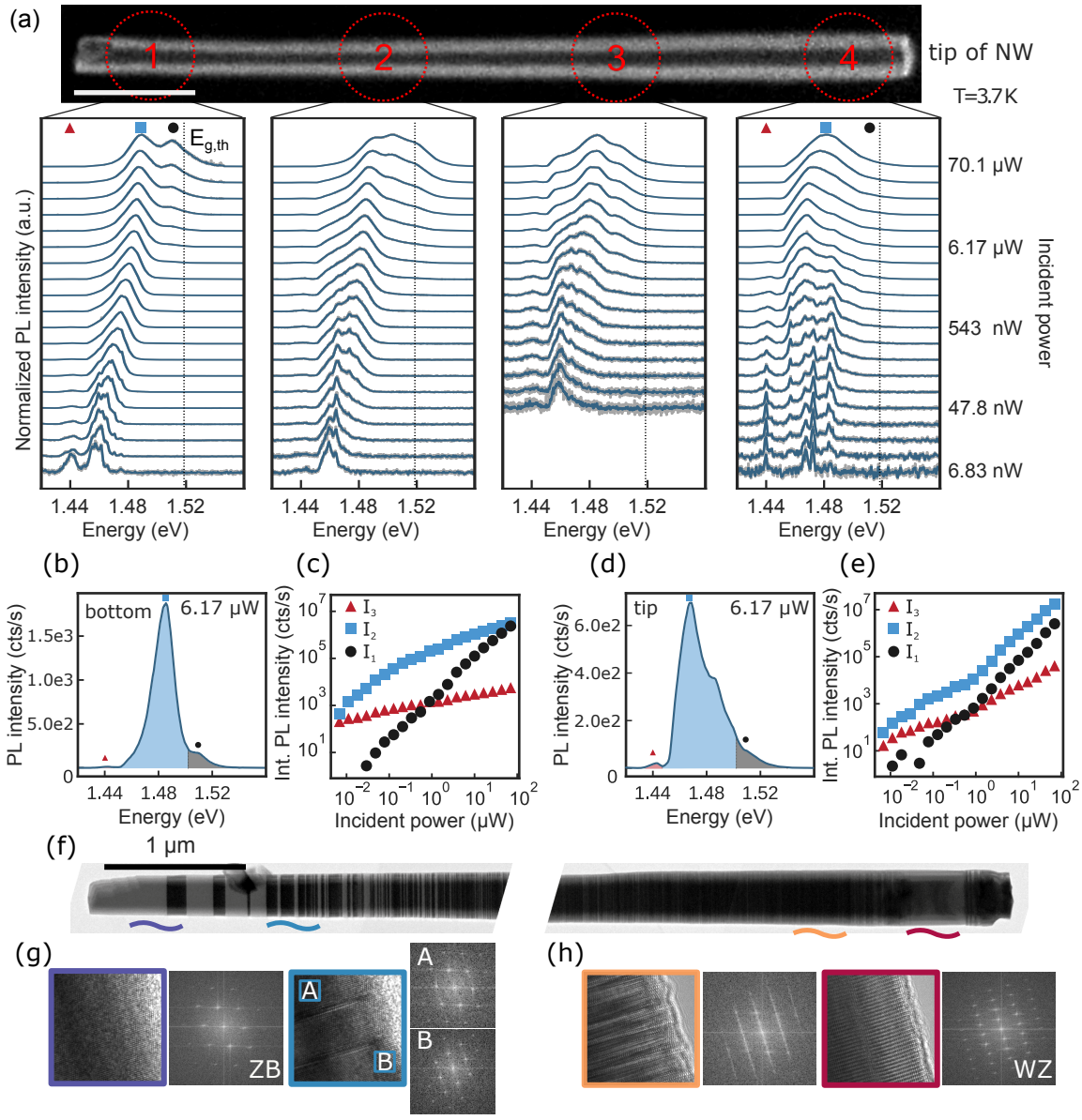

FIG. 4.2: (a) Power-dependent PL spectra along a representative AlGaAs-capped GaAs NW measured at four positions from the bottom to the tip. SEM image of the measured NW with approximate measurement positions is shown. $E_{g,th}$ marks the calculated bandgap of GaAs at 3.7 K of 1.519 eV. (b) PL spectra at 6.17 μW for the bottom of the NW; the shaded areas and corresponding symbols mark the three integration areas, I_1, I_2, and I_3 for the saturation curves in (c). (d) and (e) PL spectra and saturation curves for the tip of the NW. (f) TEM of a self-catalyzed NW grown under similar conditions showing the overall trend in crystal variation. Diffraction patterns are shown for the bottom and tip of NW, in (g) and (h), respectively, showing the two defect-free regions and neighboring twinned regions.

ously blue-shifts. Unlike for the tip end of the NW, this suggests a continuous filling of the energy bands.

With the above observations of the changes with power dependence along the length of the NW, together with the correlation to the crystal structure from TEM, the inferences can be made about what types of transitions are likely giving rise to the observed PL. At the bottom end of the NW, from the TEM, a nearly defect-free region in the ZB crystal phase, with a few twinning defects, is observed. In the PL, from this region of the NW, the bandgap peak at higher incident power approaches the intensity of the sub-bandgap peak that is starting to saturate. The sub-bandgap peak, which blue-shifts with increasing power, appears related to a single type of defect with a mostly continuous density of states. At low incident power, the appearance of multiple peaks around 1.46 eV may suggest discretization of lower energies due to quantum confinement. These transitions are associated to the twinning defects observed in the TEM at the bottom end of the NW. At the top end of the NW, a longer WZ segment (approx. 500 nm) is observed together with shorter segments of what appears to be alterations of short WZ/ZB sections on either side of it. In the PL, at low incident power, a range of peak energies between 1.45 and 1.49 eV is observed that likely arise from different confinement levels associated with the segments, where carriers quickly thermalize. Saturation of shallower, higher energy radiative transitions, gives rise to deeper, lower energy transitions, as evidenced by the lower-energy peak dominating in intensity with increasing power, before blue-shifting at higher incident power. Unlike at the bottom end of the NW, the PL intensity of sub-bandgap recombination is almost one order of magnitude higher than the band-to-band, and does not appear to saturate.

The corresponding saturation curves for the tip and bottom of the NW shown

in Fig. 4.2(c) and (e) [with intensity integration regions graphically represented in (b) and (d), respectively] provide additional information on the recombination mechanisms at the two extremes of the NW. The behavior with increasing power is similar for the tip and bottom of the nanowire for the highest energy range (shown in black), corresponding to the radiative transitions at the bandgap. The integrated PL intensity in this range is proportional to the square of the incident power (slope s is around 2 for $I \propto P^s$) as would be expected for direct band-to-band radiative transitions ($I \propto n^2$). The differences between the tip and bottom of the nanowire are due to below bandgap transitions. Referring to the mid-energy range (1.447 to 1.502 eV, shown in blue), for the bottom of the nanowire, the transitions appear to saturate, with s ranging from 1.5 at low power to 0.5 at high power. For the tip of the nanowire, s increases with increasing power (after first appearing to saturate), reaching approximately s = 2. This trend may suggest that below bandgap transitions in this case are becoming more direct. The lowest energy range with a peak at around 1.44 eV (shown in red) seems to follow the trends of the mid-energy states with regards to saturation, but unlike the mid-energy states, it negligibly shifts in energy with increasing power.

4.2.2 Time-resolved PL at different energies

Figure 4.3 shows energy-resolved TRPL for a single PL spectrum of the AlGaAs-capped nanowire to observe the variation in the radiative decay for the bandgap and sub-bandgap energy transitions, and suggest how they may be coupled. The NW is measured at the nearly defect-free bottom end, where a bandgap peak is clearly observed. The radiative transitions near the bandgap (1 and 2), show a fast radiative de-

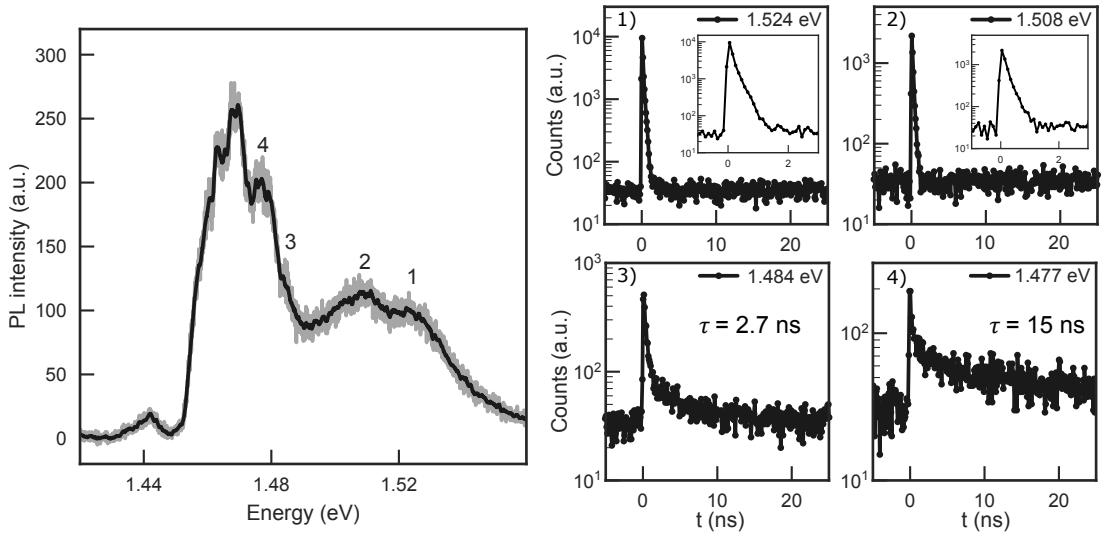

FIG. 4.3: The radiative lifetime increases (i.e. carriers recombine at a slower rate) with decreasing energy of the PL peaks. The TRPL data is taken at: (1) 1.524 eV, (2) 1.508 eV, (3) 1.484 eV, and (4) 1.487 eV indicated in the PL spectra. The fits to the TRPL signal (red lines) are shown for (3) and (4) .

cay (limited by the resolution of the set-up), which is shorter than the typical radiative lifetimes of bulk GaAs. The dominance in intensity of sub-bandgap radiative transitions suggests that the fast radiative decay of the bandgap transitions may be associated with rapid thermalization of carriers to sub-bandgap energy levels, from where they still radiatively recombine. Sub-bandgap energy transitions (3 and 4), fitted using a double exponential decay equation convoluted with the instrument response function, show significantly longer radiative lifetimes in comparison to bandgap transitions (as previously observed for highly polytype regions [63]). These lifetimes also increase as carriers go to lower energies. The longer lifetimes of sub-bandgap transitions suggests that they may be spatially indirect, dictated by the degree of overlap between the electron and hole wavefunctions. The presented results suggest that these transitions become less direct at lower energies.

4.2.3 Temperature-dependent PL

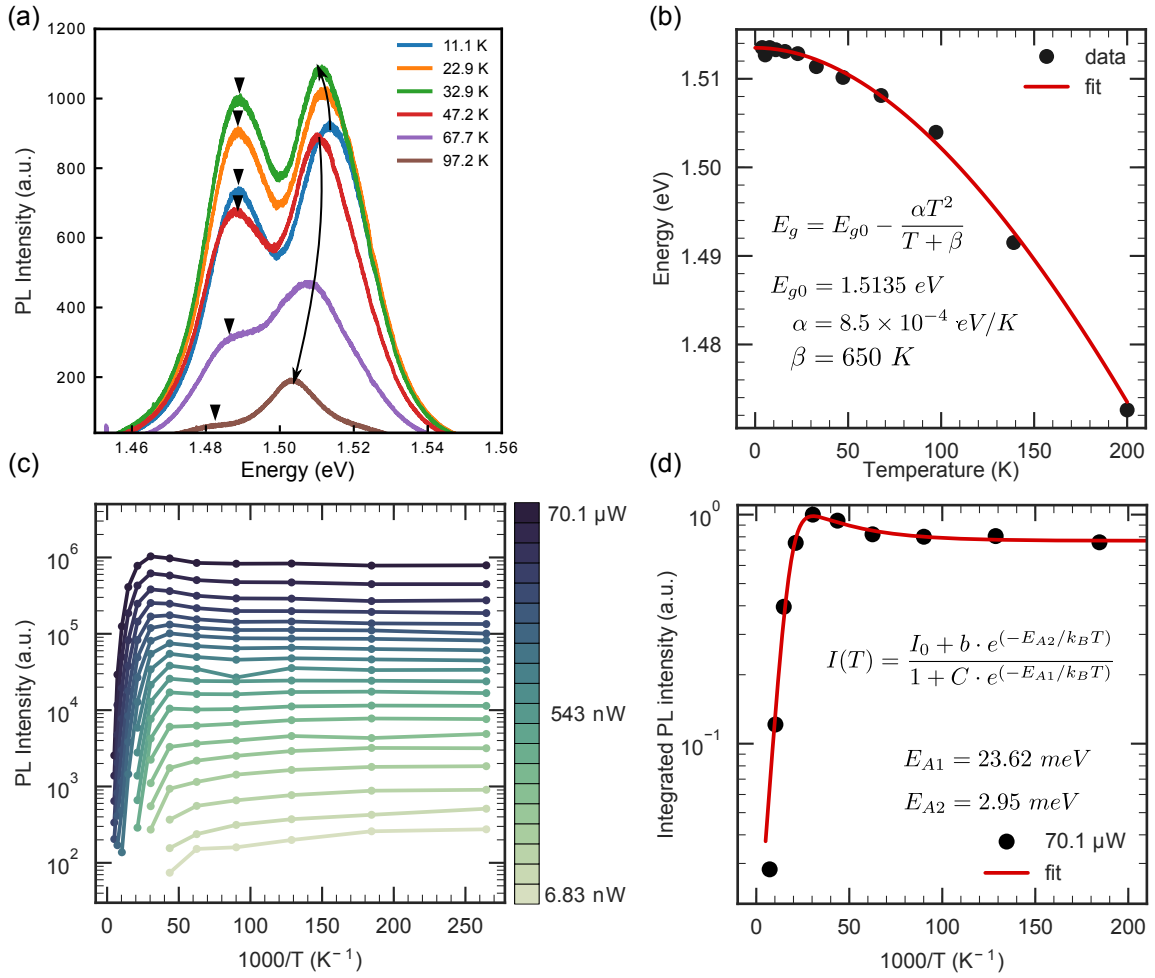

FIG. 4.4: (a) Photoluminescence from the bottom end of the GaAs NW as a function of temperature, showing the peak positions of bandgap and below bandgap transitions (b) Bandgap temperature dependence from 3.7 K to 200 K for the ZB peak at the bottom of the nanowire fitted with the Varshni model [116]. Similar results were obtained in [65] for polytype nanowires; (c) PL intensity vs. temperature for different power incidence levels; (d) Integrated PL intensity for the states at and below the bandgap at the highest power of incidence normalized to the highest intensity and fit to the model presented in Ref. [67].

The temperature-dependent PL shows an increase in PL intensity with increasing temperature (see Fig. 4.4), suggesting thermal re-emission of carriers into faster radiative channels, as previously shown for thin nanowires [67]. Here, the bottom end of the nanowire is again investigated due to the presence of longer ZB segments with a distinct ZB peak. In Fig. 4.4(a), two dominant peaks are observed: a higher energy peak, corresponding to the energy of band-to-band recombination, and a lower energy peak, corresponding to sub-bandgap, type-II spatially indirect recombination, that shift in energy according to different rules. The higher energy peak continually red-shifts in accordance with the Varshni model [116], as shown in Fig. 4.4(b). The lower energy peak negligibly shifts in energy from 11.1 to 22.9 K with a slight blue-shift at 32.9 K. This slight blue-shift of the lower-energy peak with increasing temperature together with the accompanying increase in intensity for both the band-gap and sub-bandgap peaks, suggests thermal re-emission into faster radiative channels (both higher energy sub-bandgap and band-to-band recombination). At 47.2K, the intensity of both peaks drops significantly, suggesting that thermally-activated, non-radiative recombination has surpassed the recombination due to thermal re-emission into faster radiative channels, and the lower-energy peak noticeably red-shifts with subsequent increase in temperature.

An increase in PL intensity is only observed around 30 K only for higher powers of incidence. As seen in Fig. 4.4(c), at lower powers of incidence, a decrease in the integrated PL intensity is observed. This may suggest a transfer of carriers from slower, lower energy states to faster, higher energy radiative channels with increase in power. A model from Ref. [67] is used to fit the curve at the highest power of incidence to obtain the activation energy parameters [shown in (d)].

4.2.4 The effects of surface recombination

Changing the surface cladding produces non-negligible variations in the resulting PL intensities among the samples as shown in Fig. 4.5.

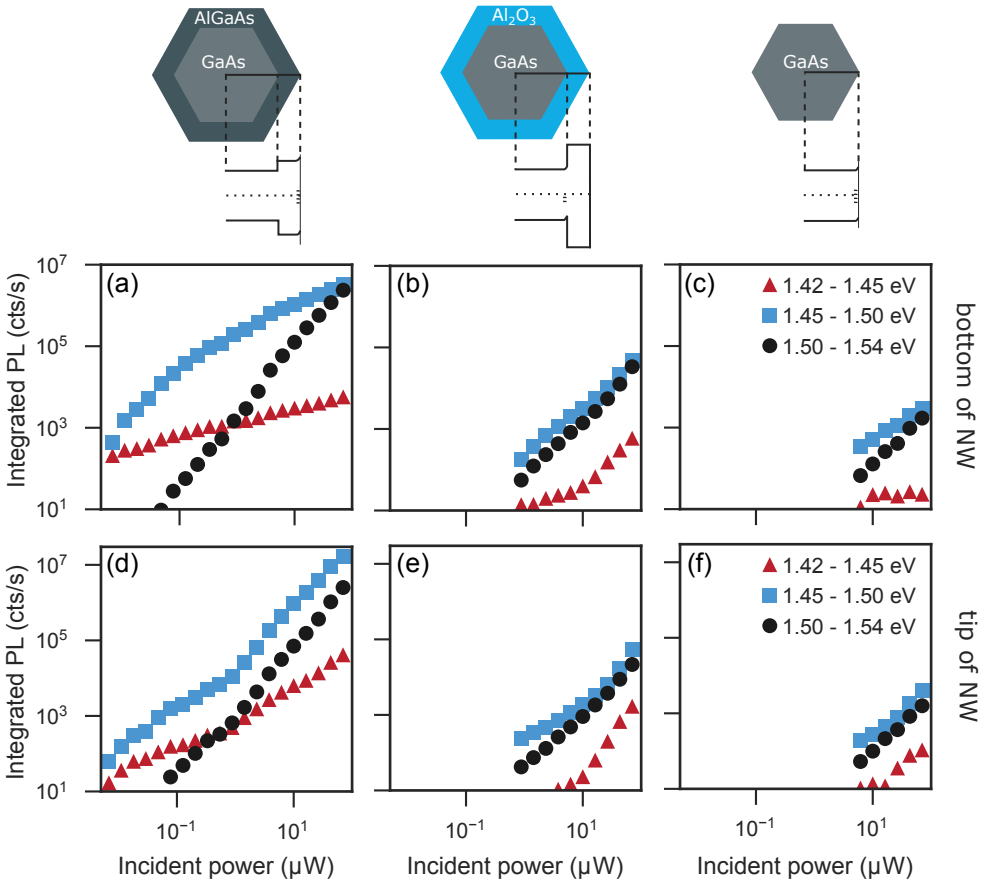

FIG. 4.5: Saturation curves for the bottom [first row, (a)–(c)] and tip [second row, (d)–(e)] of three separate nanowires showing the indicated photon energy ranges in red, blue, and black. The columns correspond to the indicated surfaces: AlGaAs-capped, Al_2O_3-capped, and uncapped.

The SEM images of the measured nanowires are included in Fig. 4.6, together with the STEM-EDX of the AlGaAs-capped sample. The images are set to the same scale. Al_2O_3-capped and uncapped NWs come from the same as-grown sam-

ple and have comparable length and thickness. Compared to the AlGaAs-capped samples, these samples are approximately 2x longer, and appear 2x thinner. The AlGaAs shell, as observed using scanning tunnel electron microscopy (STEM) energy dispersive X-ray (EDX) spectroscopy [Fig. 4.6(d)–(e) for the tip and bottom of NW, respectively], adds to the radial thickness of the AlGaAs-capped sample that accounts for some discrepancy in the NW thickness between the samples. (The higher energy PL emission from the AlGaAs shell is not included in the integrated PL calculations.) Since the AlGaAs shell only partly accounts for the discrepancy in diameter size between AlGaAs-capped and the other two samples (approx. 20-40 nm in diameter), we expect that the difference in NW diameter between the AlGaAs-capped samples and the Al_2O_3-capped (and uncapped) NWs contribute to some difference in the integrated PL intensity that we observe in the Fig. 4.5. Due to non-linear absorption, it is difficult to accurately estimate the change in PL intensity arising from the differences in NW diameter. However, we do not expect this difference to alter the trends we observe.

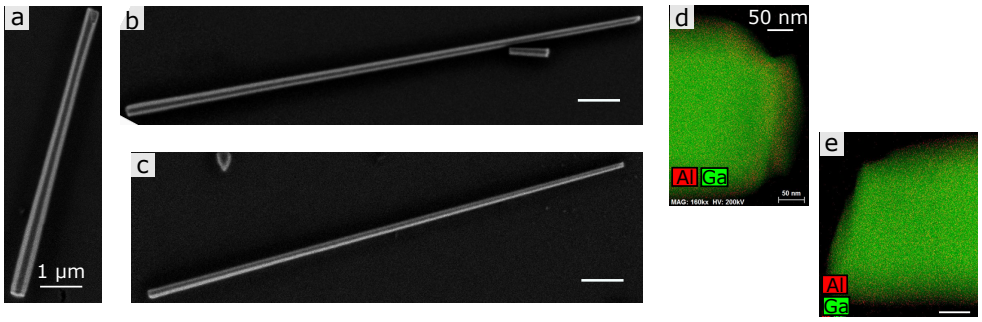

FIG. 4.6: SEM images corresponding to samples investigated in Fig. 4.5: (a) AlGaAs-capped, (b) Al_2O_3-capped, and (c) uncapped. (d) and (e) show the STEM-EDX images of the tip and bottom of an AlGaAs-capped sample indicating the presence of an AlGaAs shell, adding to the radial thickness of the sample (STEM-EDX image: L. Francaviglia).

The suppression of radiative recombination for the non-capped wires is due to the rapid thermalization to lower energy bands combined with slower radiative recombination at those energies, increasing the probability of non-radiative recombination. In other words, an increase in surface recombination reduces the quantum efficiency $QE = \frac{1/\tau_{rad}}{1/\tau_{rad}+1/\tau_{nrad}}$ disproportionately for bandgap and sub-bandgap energies. For the same non-radative lifetime, τ_{nrad}, slower radiative channels (longer radiative lifetime, τ_{rad}) will lead to a lower QE for those energy transitions.

4.3 Theory

In polytype GaAs nanowires, carriers recombine via multiple decay channels with different relaxation rates (band-to-band, defect bands, indirect spatial transitions in polytype regions, etc.). When carriers are excited above the bandgap, they quickly thermalize to the band edges. From there, they can recombine radiatively or non-radiatively across the bandgap, or thermalize to lower available energy bands from where they can also recombine. The coupling between these bandgap and sub-bandgap excited states, together with the competing rates of radiative and non-radiative recombination at each of the levels, give rise to the observed TIPL spectrum.

Here these recombination rates are analyzed using a simple model: the excited states are coupled, each of them with a well-defined relaxation rate (a fast non-radiative and slower radiative) to a common ground state. The coupling rates between the excited states depends on the occupancy level of the sub-bandgap states, which eventually saturate at higher incident optical power. A schematic diagram of this model is shown in Fig. 4.7, where:

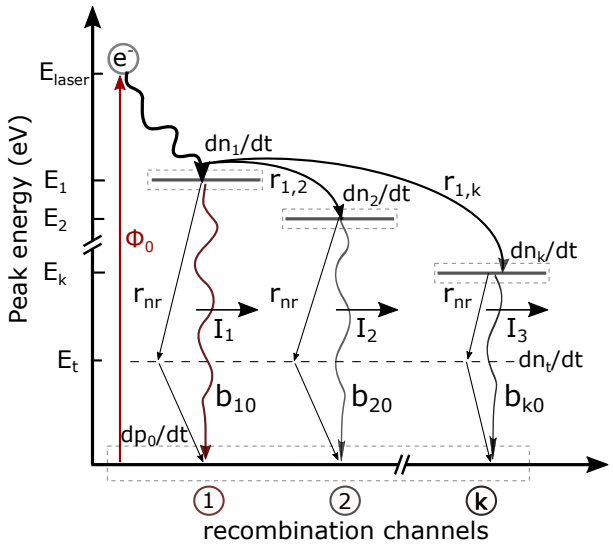

FIG. 4.7: Simplified recombination model representing ① faster band-to-band and (②–ⓚ) slower sub-bandgap transitions due to type-II indirect spatial transitions and/or defect bands that occur at discrete energy levels.

Φ_0: generation rate

p_0: number of holes in the valance band

n_1, n_2, n_k: number of electrons in the conduction band at energy levels E_1, E_2, and E_k, respectively, where $E_1 > E_2 > E_k$

b_{10}, b_{20}, b_{k0}: radiative recombination coefficients for transitions between E_1, E_2, and E_k, and E_0

r_{12}, r_{1k}: transition rate constants between energy level E_1, E_2 and E_k, respectively

r_{nr}: non-radiative recombination rate for all the energy levels

It is important to note that this simple model does not assume the cause of the below bandgap transitions (i.e. the model can be used to describe various causes of below bandgap transitions). Rather the recombination model helps us study the interactions between these different levels in both the steady-state and transient regimes. Equations (4.1)–(4.4) below describe the recombination mechanisms

shown in Fig. 4.7

$$dp_0/dt = \Phi_0 - b_{10}n_1p_0 - r_{nr}n_1 - b_{20}n_2p_0 - r_{nr}n_2... - r_{nr}n_k - b_{k0}n_kp_0 \quad (4.1)$$

$$dn_1/dt = \Phi_0 - b_{10}n_1p_0 - r_{nr}n_1 - r_{12}n_1(1-f_2) + ... - r_{1k}n_1(1-f_k) \quad (4.2)$$

$$dn_2/dt = r_{12}n_1(1-f_2) - b_{20}n_2p_0 - r_{nr}n_2 \quad (4.3)$$

$$dn_k/dt = r_{1k}n_1(1-f_k) - b_{k0}n_kp_0 - r_{nr}n_k \quad (4.4)$$

where:

N_2, N_k: number of available states in energy levels E_2 and E_k, respectively

f_2, f_k: $f_2 = \frac{n_2}{N_2}$ and $f_k = \frac{n_k}{N_k}$

relate to the saturation of sub-bandgap energy levels. The model is further expanded to show the effect of increasing temperature on the carrier dynamics. The effects of thermal re-emission between sub-bandgap and bandgap energy levels are included, as well as thermally-activated non-radiatiative recombination to the model, similar to the model in Ref. [67]. The equations above are expanded with the inclusion of temperature-dependent terms:

$$\begin{aligned} dp_0/dt &= \Phi_0 - b_{10}n_1p_0 - r_{nr}n_1(1-e^{\frac{-E_{a,nr}}{k_BT}}) - b_{20}n_2p_0 \\ &\quad -r_{nr}n_2(1-e^{\frac{-E_{a,nr}}{k_BT}})... - b_{k0}n_kp_0 - r_{nr}n_k(1-e^{\frac{-E_{a,nr}}{k_BT}}) \quad (4.5) \\ dn_1/dt &= \Phi_0 - b_{10}n_1p_0 - r_{nr}n_1(1+e^{\frac{-E_{a,nr}}{k_BT}}) - r_{12}n_1(1-f_2)(1-e^{\frac{-(E_1-E_2)}{k_BT}}) + ... \\ &\quad -r_{1k}n_1(1-f_k)(1-e^{\frac{-(E_1-E_k)}{k_BT}}) \quad (4.6) \\ dn_2/dt &= r_{12}n_1(1-f_2)(1-e^{\frac{-(E_1-E_2)}{k_BT}}) - b_{20}n_2p_0 - r_{nr}n_2(1+e^{\frac{-E_{a,nr}}{k_BT}}) \quad (4.7) \\ dn_k/dt &= r_{1k}n_1(1-f_k)(1-e^{\frac{-(E_1-E_k)}{k_BT}}) - b_{k0}n_kp_0 - r_{nr}n_k(1+e^{\frac{-E_{a,nr}}{k_BT}}) \quad (4.8) \end{aligned}$$

where k_B is the Boltzmann's constant, T is the temperature, and $E_{a,nr}$ is the thermal activation energy to non-radiative channels. The radiative rate constants (e.g. b_{10},

b_{20}, etc.) are assumed to remain constant with temperature. A temperature dependence of band-to-band radiative recombination ($\tau_{rad} \propto T^{3/2}$) suggested elsewhere is not included in this model[117, 118] as the effect is relatively weak compared to the thermally activated portion of the temperature dependence.

4.4 Discussion

From the experimental data and the model, several observations are made regarding radiative recombination in these polytype NWs. The large laser spot relative to the density of twin defects and polytype heterointerfaces, prevents us from analyzing each type of transition in isolation. In the work by Vainorius et. al., the high crystal quality and precise control of phase-switching in gold-catalyzed NWs had allowed for characterization of optical properties of isolated WZ and ZB segments [66]. In this case, the carrier dynamics are more complex and cannot be easily separated. Using NWs exhibiting similar trends in crystal phase-switching and density of defects to the NWs studied here, Heiss et. al. have directly correlated the optical and structural properties at nm-scale and used first-principle calculations to validate their results [68]. However, doing this type of detailed calculation for each NW sample is cumbersome and computationally expensive. Here, a simplified approach that considers the power- and temperature- dependence of integrated PL intensity of bandgap and sub-bandgap transitions (that arise due to twin interface defects and spatially indirect recombination between different polytypes), coupled with a rate equation analysis is presented. The model helps us understand how the coupling between the bandgap and sub-bandgap transitions gives rise to the observed PL intensity for these energy ranges.

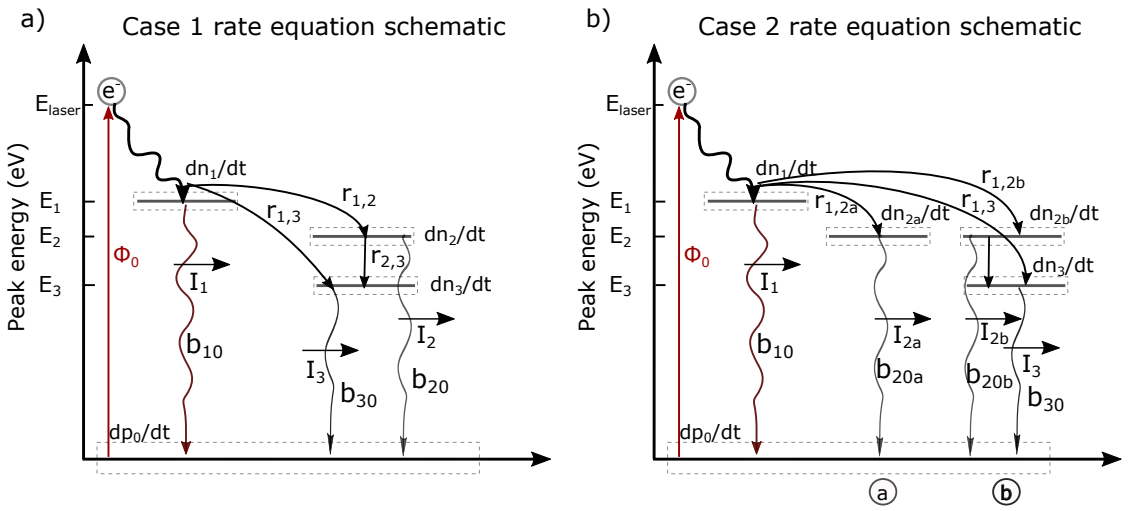

FIG. 4.8: Rate equation schematic for the two cases investigated: (a) twin defect and (b) polytype section.

Two cases of recombination dynamics corresponding to the experimental observations are modeled for the bottom and tip of the of the NW, respectively. At the nearly defect-free bottom end of the NW, observed sub-bandgap radiative transitions [Fig. 4.2(a)] appear to arise from a single type of defect, most likely due to the twin interfaces observed in the corresponding TEM. Despite the fact that the laser spot is likely illuminating multiple twin defects, in the model, the collective effect of multiple twin defects on recombination dynamics is approximated using a representative twin defect [Fig. 4.9(a)]. The approximation is based on the information implied from the shape and evolution of the sub-bandgap peak—a single dominant peak that continually blue-shifts (with few individual peaks at low incident power suggesting some discretization at lower energy levels). At the top end of the NW, the shape and evolution of the sub-bandgap peak (or rather a collection of peaks) suggests more complex carrier dynamics that arise from both polytype crystal phases (as well as additional twin defects) that observed in the corresponding TEM. Considering the effect of each polytype section illuminated by the laser spot on the resulting sub-bandgap re-

combination dynamics would be hard to separate. To simplify the model, the trends in the PL that arise from the combined effect of these defects are considered — multiple peaks at a range of energies at low excitation giving rise to a dominant peak at low energy with increasing power, followed by a blue-shift. This interaction between shallow and deep traps, whose signature is observed in the PL, is approximated using two traps with different confinement levels [Fig. 4.9(b)]. Figure 4.9 shows the model results of radiative recombination events as a function of generation rate (power) in assuming three energy levels (E_{1-3}), with their corresponding radiative recombination coefficients (b_{10-30}). In the first case [Fig. 4.9(a)], a distribution of energy levels that fill sequentially (lowest energy level, E3 saturates first, followed by E2, before reaching the bandgap level, E1), stemming from a single (or same type) of defect is assumed. In the second case [Fig. 4.9(b)], multiple defects with varying confinement levels where carriers recombine independently of each other is assumed. The two cases aim to reproduce the effect of a spatially continuous and discontinuous density of states that implied from experimental data in Fig. 4.2 for the low-defect (bottom of NW) and highly polytype regions (tip of NW), respectively. The rate equation models for the two cases are schematically represented in Fig. 4.8.

Three coupled energy levels are assumed, where E_{10} corresponds to radiative recombination events at the bandgap energy. The energy levels below the bandgap (E_{20} and E_{30}) recombine at decreasing radiative recombination coefficients ($b_{20} > b_{30}$), and have decreasing saturation levels ($N_2 > N_3$), corresponding to the case in (a) where states are filled sequentially in energy. The second case [Fig. 4.9(b)], illustrates the effect of an ensemble of confined states of varying energy distributions; it assumes recombination at two wells of different depths occurring in parallel. The deepest well spans a wider range of available energies (represented here by energy

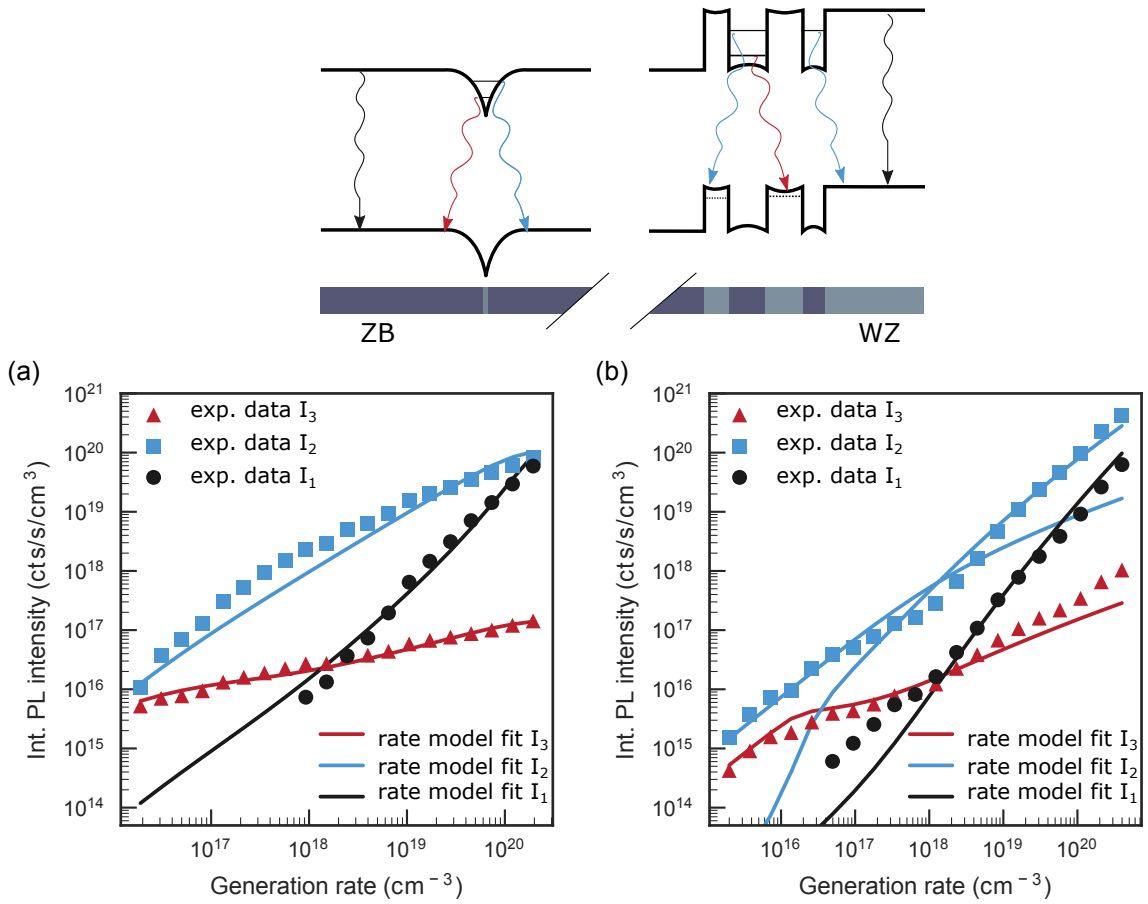

FIG. 4.9: Recombination model showing the saturation of energy levels assuming (a) a single trap and (b) distribution of deep and shallow traps. E_{10}, E_{20}, and E_{30} refer to radiative recombination events where E_{10} corresponds to highest, band-to-band transition

levels E_2 and E_3) while shallower wells have fewer energy levels close to the bangap (represented here by E_2). In the simulation, the recombination events (E_{10}, E_{20} and E_{30}) of the combined effect of the two wells are tabulated, shown in (b).

The two cases illustrated here in (a) and (b) closely correspond to the experimental observations of TIPL in Fig. 4.2 for the bottom and tip of the nanowire in (c) and

(e), respectively. The fit parameters for the two cases are shown in Tables 4.1 and 4.2.

TABLE 4.1: Case 1 Modeling Results

radiative recomb. coeff. (cm^3/s)	saturation level (cm^{-3})	transition rates between levels (s^{-1})
$b10 = 8.86 \times 10^{-6}$		
$b20 = 1.00 \times 10^{-10}$	$N2 = 1.08 \times 10^{15}$	$r12 = 1 \times 10^{11}$
$b30 = 1.20 \times 10^{-12}$	$N3 = 1.08 \times 10^{14}$	$r13 = 1 \times 10^{10}$, $r23 = 1 \times 10^{4}$

TABLE 4.2: Case 2 Modeling Results

radiative recomb. coeff. (cm^3/s)	saturation level (cm^{-3})	transition rates between levels (s^{-1})
$b10 = 8.86 \times 10^{-6}$		
$b20_a = 2.40 \times 10^{-9}$	$N2_a = 1.88 \times 10^{12}$	$r12_a = 1 \times 10^{11}$
$b20_b = 2.00 \times 10^{-11}$	$N2_b = 2.00 \times 10^{17}$	$r12_b = 3 \times 10^{11}$
$b30 = 1.20 \times 10^{-12}$	$N3 = 5.82 \times 10^{13}$	$r13 = 1 \times 10^{10}$, $r2_b3 = 5 \times 10^{4}$

The fit may be further improved by assuming a distribution of energies arising from an ensemble of localized states as proposed by Li et. al. [119].

In Fig. 4.2(c) and (e), negligible non-radiative recombination is implied, corresponding to well-passivated nanowires, as expected for the AlGaAs-capped wires. To include the effect of the surface, a non-zero non-radiative component (r_{nr}) is added, which affects all the available energy levels. The non-radiative recombination rate is therefore in direct competition with the radiative recombination rate at each of the levels (an assumption is not made that regions with slower radiative channels may also be giving rise to higher concentration of surface defects). The simulation results with and without non-radiative recombination are shown in Fig. 4.10. These results show the expected effect of non-radiative recombination on the sub-bandgap

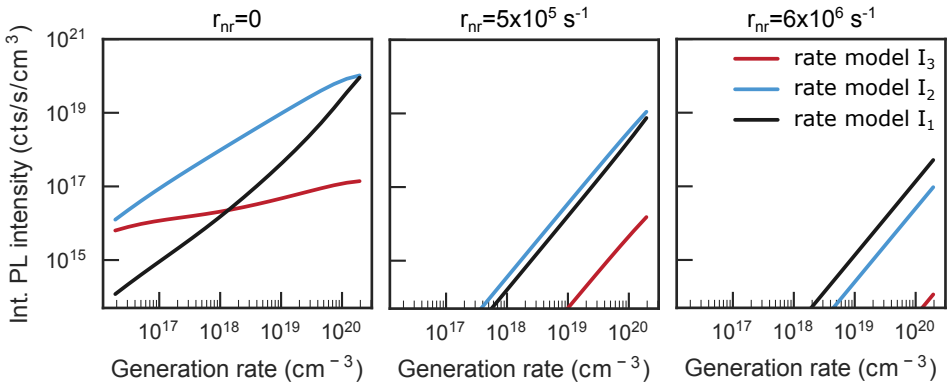

FIG. 4.10: Recombination model showing the saturation of energy levels without non-radiative recombination (left) and with varying levels of non-radiative recombination (middle and right).

radiative channels due to slower radiative recombination rate, corresponding to experimental observations shown in Fig. 4.5.

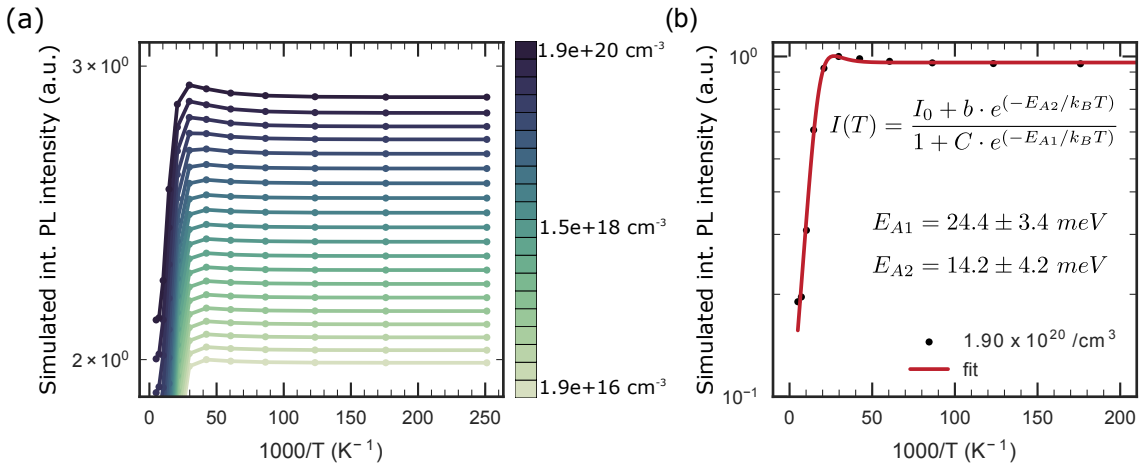

FIG. 4.11: (a) Simulated integrated radiative recombination intensity with existence of slower sub-bandgap channels as a function of inverse temperature (x-axis) and incident power (individual lines), with increasing generation rate moving from bottom to the top of the graph with each line normalized to its own max PL intensity. The individual lines are offset for clarity. (b) The line at highest power of incidence fitted to model from Ref. [67].

The simulations shown in Fig. 4.11 further illustrate the effect of carrier ther-

mal re-emission and thermally activated non-radiative recombination on the radiative emission. The simulated data aims to model the experimental data shown in Fig. 4.4 (the model, however, does not include the bandgap temperature dependence). The simulation results shown in (a) correspond to the temperature-dependent time-integrated PL intensity; individual lines represent varying levels of incident optical power. At low power, increasing the temperature only leads to a decrease in integrated PL intensity due to thermally activated non-radiative recombination; thermal re-emission to faster radiative channels appears negligible due to prohibitively high energy barrier preventing carriers from re-emitting into the bandgap continuum of states. As sub-bandgap energy levels start to saturate with increase in power, the probability of thermal re-emission and recombination at higher energies becomes more likely, leading to a gain in emission.

The gain in emission occurs when the ratio of non-radiative to radiative recombination in the sub-bandgap states becomes non-negligibly higher than in the bandgap states as a result of rising thermally activated non-radiative recombination. This produces a gain in PL intensity as carriers are re-emitted into a bandgap continuum, increasing their chances of recombining radiatively. In (b), the temperature-dependent TIPL is taken at highest incident power and apply the model in Ref. [67] to fit the simulated data. A good agreement between the two models is demonstrated with this fit, as well as the power dependence of temperature-dependent PL. The best fit to the simulated data gives activation energies E_{A1} and E_{A2} of 28.5$\pm$0.2 and 9.5$\pm$0.1 meV, respectively. This is similar to the input values used in the model for $E_{a,nr}$ of 30 meV and the difference between E_1 and E_2 of 10 meV, with discrepancies arising from the averaged effect on recombination of the sub-bandgap states in the model.

With the experimental data of the reference sample, the AlGaAs-capped GaAs

NW, and the model, the following is suggested concerning recombination in polytype NWs:

(1) Carriers thermalize from the bandgap energy level to the lowest and spatially closest available energy level from where they either recombine radiatively (at longer radiative lifetimes) or further thermalize to defect-level states and recombine non-radiatively. Despite the fact that longer sections of faultless crystal are observed at both ends of the NW—ZB at the bottom and WZ at the top [see Figs. 4.2(g) and (h)]—TIPL in Fig. 4.2(a) shows dominance in intensity of the sub-bandgap peaks(s) along the length of the NW. The peak associated with band-to-band recombination approaches the intensity of the sub-bandgap peak only for the bottom of the NW (where lowest defect density is observed) as the sub-bandgap energy levels appear to saturate. The TRPL in Fig. 4.3, showing the rapid radiative decay of bandgap energies, coupled with dominance in intensity of the sub-bandgap peaks, further suggests thermalization of carriers that suppress band-to-band recombination and enable recombination at sub-bandgap energies (either radiative or non-radiative). The TRPL results also show longer radiative lifetimes at sub-bandgap energies (that further increase for lower energy peaks). The increase in PL intensity with temperature (Fig. 4.4) due to thermal re-emission of carriers into higher energy faster radiative channels (evidenced by slight blue-shift of sub-bandgap energy peak), further suggests thermalization to and longer radiative lifetimes at lower energies of radiative transiton. The model results compare well to the experiment with the implementation of these experimental observations (fast thermalization rate from the bandgap to sub-bandgap energy levels together with saturation level and longer radiative lifetimes at these energies) in Fig. 4.9. The modeled temperature-dependence results (Fig. 4.11), showing the effect of thermal re-emission and thermally-activated non-

radiative recombination on the PL intensity, agree with the trends observed in the experiment.

(2) In regions of low crystal variation and long diffusion lengths, carriers will travel along the wire before reaching a lower energy state from which to recombine. In the nearly defect-free bottom end of the NW [Fig. 4.2(g)], the PL intensity is dominated by recombination at sub-bandgap energies [Fig. 4.2(a)], suggesting that carriers quickly thermalize to lower energy levels before being able to recombine at the bandgap energy. The sub-bandgap states have a continuous distribution as evidenced by the shape of the lower energy, sub-bandgap peak, with discretization at the lowest energies (discrete peaks at low incident power). The model results compare well to the experiment [see Fig. 4.9(a)] when one interface defect is assumed, where carriers quickly thermalize from the bandgap energy level until they saturate the defect states. Carriers recombination at sub-bandgap energies is set to recombine at longer radiative lifetimes, decreasing for higher energies of transition (as observed from TRPL in Fig. 4.3).

(3) In regions of high crystal variation and short diffusion lengths, photo-excited carriers thermalize close to the laser spot producing discrete peaks. Spatially localized states of varied 1-D confinement level produce peaks over a range of energies at low excitation. From the TIPL in Fig. 4.2(a) for the top end of the NW, discrete peaks at low incident power are observed. This region shows the presence of a longer WZ with thin alternating segments in the transition region between the two phases [Fig. 4.2(h)] that are expected to lead to confinement of carriers at various energy levels. The model results compare well to the experiment [see Fig. 4.9(b)] when the presence of different confinement levels is approximated with two wells (a shallow and a deep well) with weak transition rates between the wells. As the generation rate

increases and the shallow wells saturate, larger portion of generated carriers thermalize in the deeper well. In the TIPL, this is evidenced by the dominance in intensity of the lower energy peak with the increase in incident power.

(4) In polytype wires, the thermalization of carriers to lower energy radiative channels is not easily separable from surface recombination. The signature will appear similar and further injection-dependent TRPL measurements are needed to address the impact of the surface. In Fig. 4.3, the fast radiative decay at the bandgap energy could either indicate non-radiative recombination or thermalization to lower energy levels from which carriers can still radiatively recombine. Detailed injection-dependent energy-resolved TRPL measurements, coupled with a rate equation model, can provide additonal insight into how the bandgap and sub-bandgap energy levels couple to produce the observed steady-state PL intensities when incident power is varied.

(5) Polytype nanowires may exhibit higher surface recombination losses due to the presence of slower radiative channels. Changing the properties of the surface (from AlGaAs to Al_2O_3 to uncapped) increases non-radiative recombination losses, as seen from integrated PL intensities in Fig. 4.5 and simulated data in Fig. 4.10; with rapid thermalization to lower energy levels, and slower radiative recombination at these sub-bandgap energies, lower radiative efficiency is expected for polytype samples compared to defect-free samples. The model results show that slower sub-bandgap radiative recombination is more affected by the non-radiative recombination. While the reduction in integrated PL intensity due to increased non-radiative recombination rate is observed for both bandgap and sub-bandgap radiative transitions, the latter shows a more significant reduction: the integrated PL intensity due to band-to-band

recombination approaches and then surpasses that of sub-bandgap recombination with increased non-radiative recombination (Fig. 4.10).

4.5 Summary

The recombination mechanisms present in polytype GaAs NWs were discussed using experimental data and a rate equation model developed in this dissertation. First, the power-dependent PL peak evolution is correlated with TEM measurements along an AlGaAs-capped NW. The observed peak evolution for nearly defect-free regions and polytype regions suggests a spatially continuous and discontinuous density of states, respectively. Saturation curves for the integrated PL in bandgap and sub-bandgap energy regions further show saturation of the sub-bandgap states in nearly defect-free regions of the NW, while in polytype regions, sub-bandgap states dominate in intensity. Time-resolved PL at different energies suggests that carriers radiatively recombine slower at sub-bandgap energies compared to bandgap energies, and the radiative decay rate continues to decrease with decreasing energy of the PL peaks. The presence of slower and faster radiative channels at different sub-bandgap energies is also evidenced by an increase in PL intensity with increasing temperature, suggesting thermal re-emission of carriers into faster radiative channels. In addition to the AlGaAs-capped NWs, the effect of surface recombination using NWs with different claddings (Al_2O_3 and no capping at the surface) were investigated. A non-negligible decrease in the PL intensity was observed for the two samples compared to the AlGaAs-capped sample, which was associated with non-radiative surface recombination. The rate equation model developed here was then used to investigate different configurations of polytype defects along the wire, including the effects of

surface and temperature, which compares well with experiment considering spatially indirect recombination between different polytypes, and defect-related recombination due to twin planes and other defects. The study of recombination mechanisms in polytype NWs is a path towards predicting the efficiency of NW-based devices comprising them, and coupling PL characterization with rate equation analysis is a valuable method towards this goal.

Chapter 5

MODELING OF SILICON NANOPILLARS FOR REDUCED OPTICAL LOSSES IN ULTRA-THIN SILICON SOLAR CELLS

In this chapter, the properties of silicon nanopillar structures are investigated using full-wave optical simulation, and compared to the measured values of the fabricated structures. The simulated data is used to explain the mechanisms that contribute to the observed reduced front surface reflectance, including their potential to assist in increased light-trapping through scattering and light diffraction.

5.1 Samples

Si nanopillars were fabricated using silica nanosphere (SNS) lithography (SNL), as discussed in Sec. 2.3.2, which offers a low-cost nanolithography approach with relatively easy control of pattern scale by introducing various sizes of SNSs [76]. The SNSs were deposited via a solvent-controlled spin-coating method [75] and the nanopillars etched via metal-assisted chemical etching (MaCE). Four different pillar geometries were fabricated through a combination of SNL and MaCE for a diameter of 344 nm and period of 600 nm at four different heights from 100 nm–400 nm, shown in Fig. 5.1. (J.Y. Choi fabricated the structures; details of the fabrication method can be found in Ref. [120].)

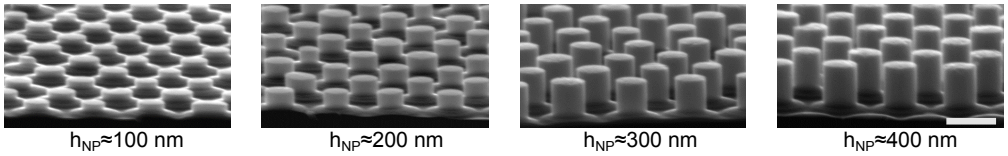

FIG. 5.1: SEM images of silicon nanopillar structures with approximate heights of nanopillars. Scale bar corresponds to 500 nm. Images adapted from [120].

.

5.2 Simulation set-up

The reflectance spectra from fabricated nanopillar structures is simulated using full-wave simulation using the MEEP frequency-domain solver [97] in the 300–1000 nm wavelength range using a plane wave source at normal incidence. A simulation box of size ($\sqrt{3}p \times p$) in the in-plane direction, where p is the array period, captures the unit cell of the periodic structure, with periodic boundary conditions (PBCs) defined along each direction. The height, h, of the simulation domain is chosen based on the combined thickness of substrate and the nanopillars. To "absorb" the reflected light, a perfectly matched layer (PML) is placed on the top of the simulation domain, as discussed in Sec. 3.3.4. When only front reflectance is desired, the PML layer is also placed at the bottom of the simulation domain, thus eliminating back reflectance (i.e. representative of an infinitely thick substrate). Thin substrates with back reflectors are simulated with a placement of a perfect electric conductor (PEC) at the bottom boundary. The mesh grid was set to 10 nm over the entire simulation volume. The reflectance spectra were calculated with the placement of a flux monitor between the plane-wave source and the structure. The optical constants of Si were taken from literature [99].

5.3 Reduced broadband reflectance

Figure 5.2 shows the simulated and measured reflectance spectra for trigonal arrays of Si NPs. The nanostructured surfaces reduce the reflectivity over the entire spectrum for all of the four measured heights. The simulated reflection spectra shows good correlation to spectrophotometry measurements, with major differences arising from more defined interference peaks observed in the simulated data. Overall, the simulated data shows good correlation to the measured reflectance for lower aspect ratio nanopillars, decreasing for higher aspect ratio nanopillars where interference peaks are more prominent. The offset between reflection peaks and valleys for higher aspect ratio NPs, between measured and simulated data, may indicate some non-uniformity in height among the NPs that gets averaged over the measured area of the wafer. The simulated structures also simplify the geometry of the fabricated structures by assuming vertical sidewalls at the substrate/NP interface. The fabricated structures actually have a more gradual (conical) base near the interface that reduces the interference peaks we observe in the simulated data, and potentially approximates the measurements more closely.

The reflectance in the lower wavelength region ($\lambda < 600$ nm) can be further reduced with the addition of a dielectric coating. Figure 5.3 shows the simulated data for the case of Si NPs with height of 200 nm and a conformal coating of a 70-nm silicon dioxide layer of 70 nm showing the lowest reflectance. Simulated reflectance of the uncoated NPs and a bare silicon substrate are shown for comparison.

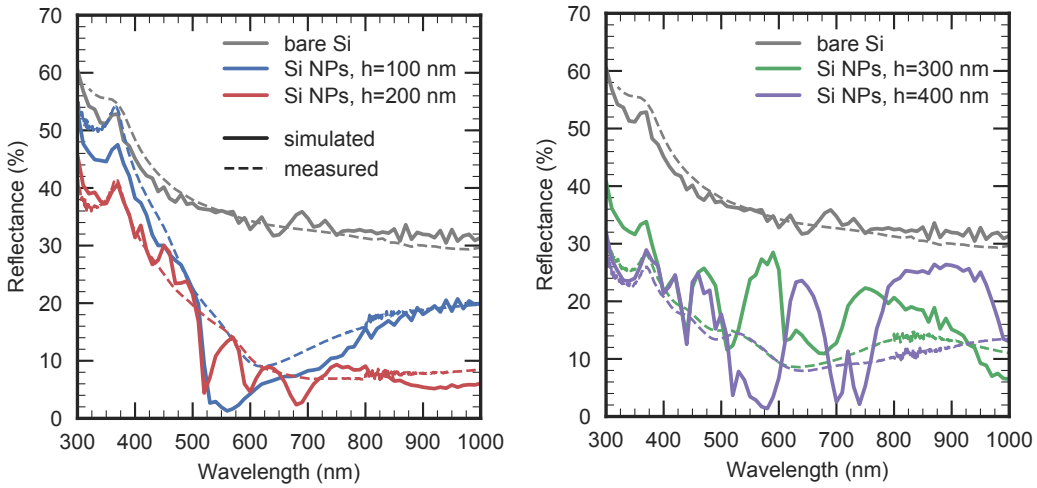

FIG. 5.2: Simulated (solid) and measured (dashed) reflectance spectra from a regular trigonal array of Si NPs with heights of 100 (blue), 200 nm (red), 300 (green), and 400 nm (purple). The period and diameter of the structures is kept constant at 600 nm and 344 nm, respectively. The reflectance from a bare Si surface is included for reference (gray) [78].

.

5.4 Forward scattering of incident light

Spinelli *et al.* have previously demonstrated that short aspect ratio nanopillars fabricated on a silicon substrate produce leaky Mie resonances, resulting in a strong forward scattering to the Si substrate [30] (see Fig. 2.1(c), Sec. 2.2.1). The result is a broadband reduction in reflection.

We observe the forward scattering by calculating the fields along the vertical cross-section at the nanopillar/substrate interface. In Fig. 5.4, we observe some degree of forward scattering for all the four heights of nanopillars at the 900 nm wavelength shown here. At the lower end, we observe weakened forward scattering at 100 nm height compared 200 nm, potentially due to too small a volume of pillars for efficient scattering. On the other hand, we observe weaker scattering for the 400 nm pillars

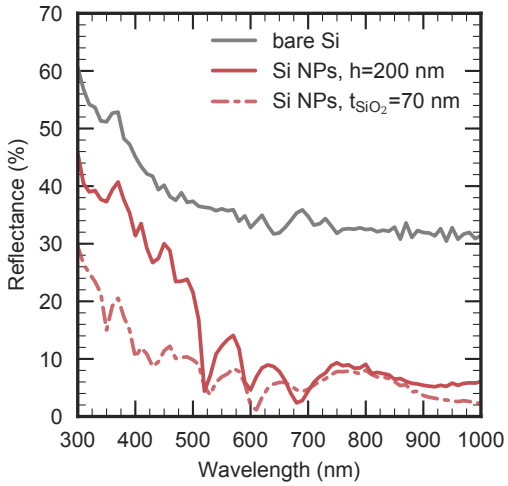

FIG. 5.3: Further reduction in reflectance with SiO_2 coating at shorter wavelengths.

.

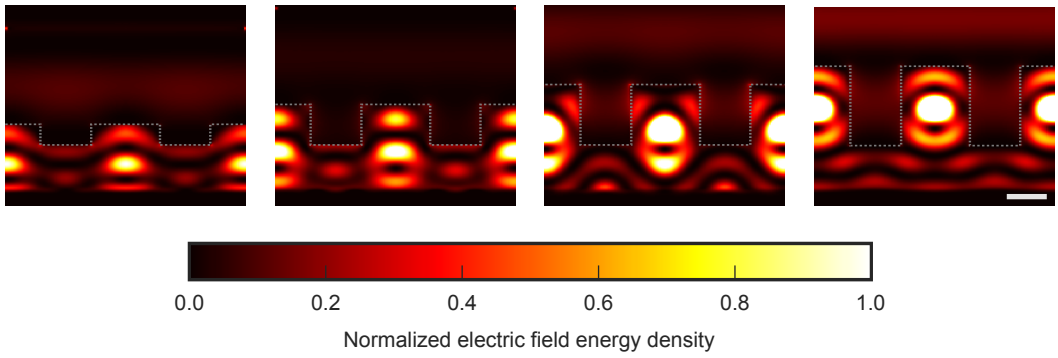

FIG. 5.4: Electric field energy density at NP cross-sections for incident light scattering at 900 nm wavelength showing forward scattering of light to the substrate below for nanopillar heights of 100 nm, 200 nm, 300 nm, and 400 nm (from left to right). The scale marker indicates 200 nm.

.

compared to the 300 nm, which appears related to stronger field confinement within the taller nanopillars that reduce scattering into the substrate below. From the simulated reflectance data, we can also confirm that the taller pillars produce stronger interference effects, acting more as a lower refractive index coating as opposed to a

scatterer. Light diffraction for these heights appears stronger between the NPs, as a result of the grooves, as opposed to scattering from the NPs.

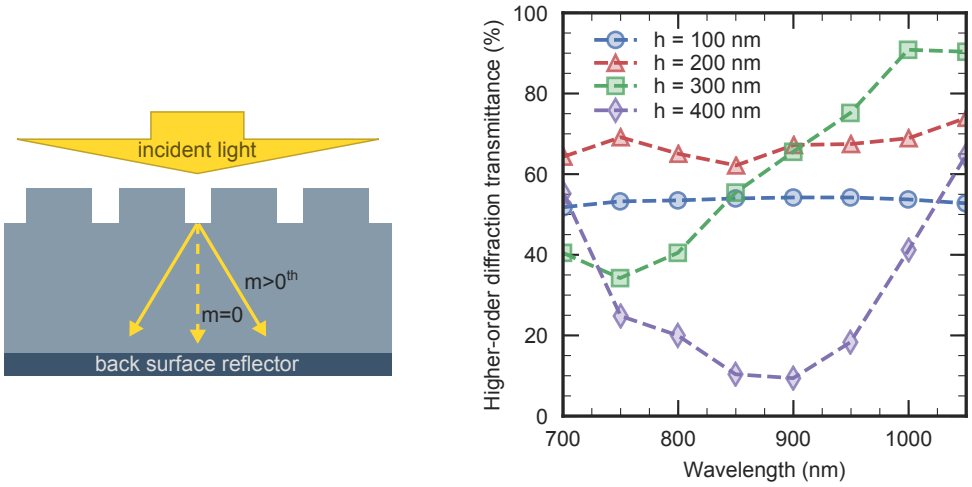

FIG. 5.5: Percentage of higher-order diffraction ($m > 0^{th}$) in transmission for different heights of arrayed Si NPs. Adapted from [79].

.

Complementary simulations, using rigorous coupled wave analysis (RCWA), were used to compute the optical diffraction efficiency of the structures at longer wavelengths [79]. Figure 5.5 shows nearly-uniform diffraction for the lower-aspect NPs, and strong wavelength dependence for the higher-aspect NPs. At 900 nm wavelength, 200 nm and 300 nm NP samples perform equally well. However, for the near-bandgap light, the 300 nm NP sample outperforms the 200 nm sample (where even the 400 nm sample surpasses the 100 nm sample).

5.5 Light-trapping in ultra-thin silicon substrates

Forward scattering from periodic arrays has the additional benefit of increasing the diffraction order of light, beneficial for trapping light in thin substrates, especially

at wavelengths where it is poorly absorbed. To investigate the effect of the nanopillars on light trapping, a 1-μm Si substrate with a perfectly reflecting back was simulated using various NP heights, keeping the NP diameter and period constant at 344 nm and 600 nm, respectively. Figure 5.6 shows the maximum simulated short-circuit current density, J_{sc}, for a 1-μm thick substrate for a set of NP heights, assuming ideal quantum efficiency and carrier collection (i.e. each absorbed photon generates one electron-hole pair that contributes to the current).

All of these structures appear to exceed the classical light trapping limit for a 1-μm slab for higher wavelengths (950–1000 nm) at normal light incidence. Figure 5.7 shows the total short-circuit current density at the (a) full simulated wavelength range (300–1000 nm) and (b) longer wavelength range (700–1000 nm) with contributions from the NPs and the bulk shown separately. Over the entire wavelength range, the structures with NPs of height, h=100 nm and the higher aspect ratio NPs (h=300–400 nm), perform uniformly-well in terms of absorption for two distinct reasons: for 100 nm pillars, the structure provides a shallow grating effect in combination with strong forward scattering, while the structures with higher aspect ratio NPs rely on resonance absorption within the NPs and diffraction due to the deep grating. Although Fig. 5.5 shows that the fractional diffraction above the 0^{th} order with different heights of Si NPs is higher for h=200 nm than h=100 nm over the entire wavelength range, these results indicate that h=100 nm may still provide a larger fraction of higher-order diffraction outside the escape cone, thus leading to more effective light trapping in ultra-thin absorbers ($\sim$1 μm). As the thickness increases, and reducing front surface reflectance becomes more important, we expect that the structure with

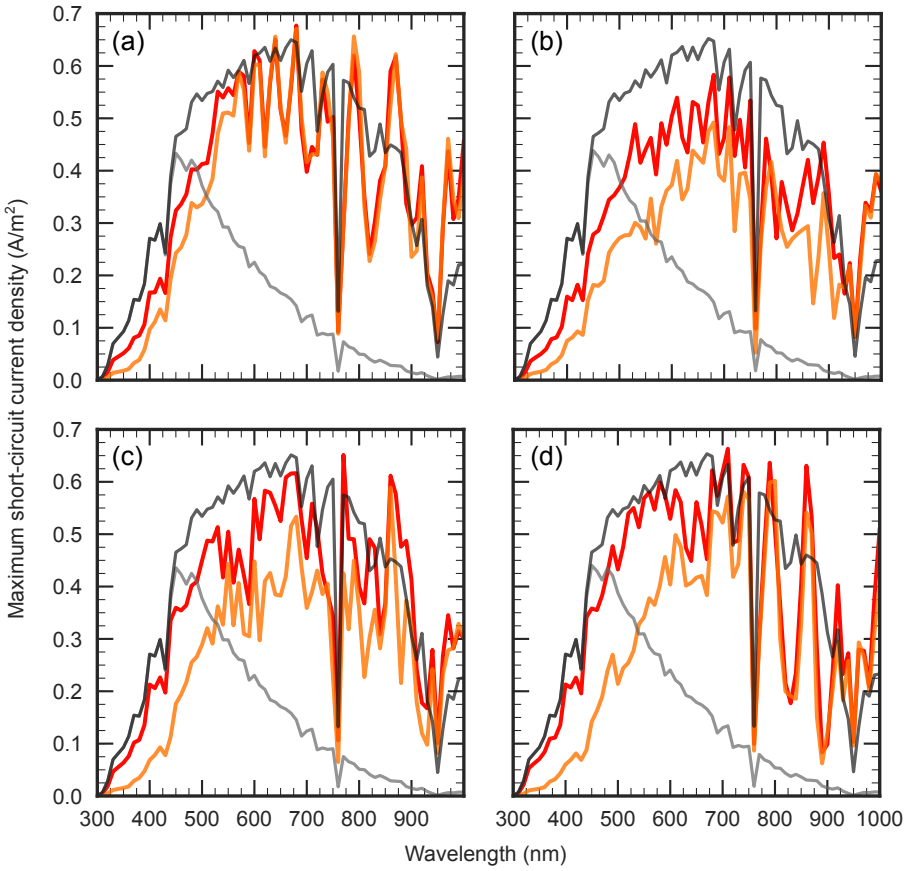

FIG. 5.6: Maximum simulated short-circuit current density, J_{sc}, for a 1-micron nanostructured silicon slab (assuming that each absorbed photon generates one electron-hole pair and is collected) with NPs of trigonal periodicity, P=600 nm, diameter, D=344 nm, and heights of (a) h=100 nm, (b) h=200 nm, (c) h= 300 nm, and (d) h= 400 nm. The figure shows the maximum achievable Jsc in the full structure (red), as well as the absorption in the 1-micron slab (blue). The maximum achievable J_{sc} based on the conventional ($4n^2$) limit and the single-pass limit are shown in black and gray, respectively [79].

.

better anti-reflection properties and comparable diffraction order will perform most optimally, in this case, 200-nm NPs.

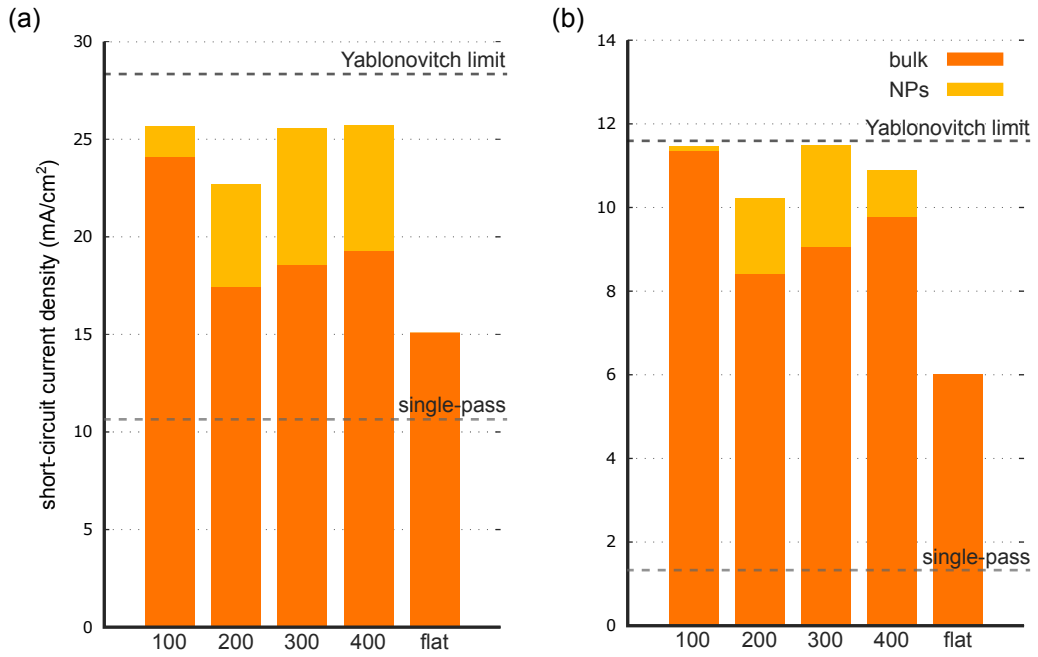

FIG. 5.7: Maximum total short circuit current density over (a) the full simulated wavelength range (λ=300–1000 nm) and (b) at longer wavelengths (λ=700–1000 nm) at normal incidence. The analysis shows that very shallow grating structures, in our case h=100 nm, shows strong confinement within the bulk structure at both wavelength ranges. The structure optimized for antireflection, h=200 nm, appears least suited for light trapping in the 1-μm slab over the both wavelength ranges [79].

.

5.6 Summary

In this chapter, optical properties of nanopillar arrays etched into silicon substrates were investigated using full-wave optical simulation in comparison to experiment. Simulated structures were used to investigate the mechanisms leading to the observed reduction in reflectance of fabricated structures. First, good agreement was demonstrated between the measured and simulated reflectance data using a unit cell with trigonal arrangement of cylinders and periodic boundary conditions along in-plane directions for the simulation. Small differences between experimental and

simulated data arose due to prominent interference peaks in the simulated data; the presence of small variations (i.e. height, diameter, spacing), as well as the tapering at the base of the NPs in fabricated structures, minimize interference effects over the measured area. The mechanisms contributing to reduced reflectance were deduced by viewing the electric field energy density profiles of the vertical cross-sections in the simulated structures. From the cross-section profiles, strong forward scattering is inferred for the short-aspect ratio nanopillars, while resonance absorption within NPs is observed for the high-aspect ratio geometries with diffraction patterns observed between the NPs at the NP/flat-surface interface. The suitability of NPs for light-trapping was then investigated by calculating diffraction efficiency (using RCWA simulations performed by J.Y. Choi), which indicated a high percentage of transmitted light at off-normal angles for poorly absorbed light. Test simulated structures were generated in FDTD for ultra-thin silicon substrates ($\approx 1\ \mu m$) to study the effect of light-trapping. The results indicated that the conventional light-trapping limit can be exceeded for certain wavelengths, approaching the limit in the full λ=700–1000 nm wavelength range for the normally incident light.

Chapter 6

PORE FORMATION IN SILICON NANOCRYSTAL THIN FILMS AND THEIR IMPACT ON OPTICAL PROPERTIES

As discussed in Chap. 2, low-refractive index inter-layers at the back surface of the solar cell (between the metal and the semiconductor) increase reflection and reduce parasitic absorption at the back contact. The NC-based films provide an alternative to thermal oxides, with the ability to easily tune the refractive index by altering their porosity. However, with increasing porosity, reduction in their performance is observed contrary to simulation that predict an improvement, when homogeneous films with equivalent effective properties are modeled. This discrepancy signaled to the increasing role of 3D inhomogeneity (i.e. arrangement of NCs, pore size distribution) with increasing porosity, whose effects are investigated here. In this chapter, the correlation between the optical properties (effective refractive index and scattering) of silicon nanocrystal (NC) thin films to their respective porosities and pore size distributions is investigated. The porosity of NC-based films is varied by adjusting the speed of cluster impaction with the substrate, and their structural and optical properties investigated using experimental and simulation approaches, starting with ellipsometry to determine film porosities based on their effective properties. The pore size distributions (PSD) were obtained using complementary approaches: nitrogen adsorption (a volumetric technique) and SEM cross-sections (physical representation of pores). Their scattering properties were then investigated using transmission haze and angular intensity distribution measurements (see Chap. 3 for method details). Nanoparticle thin films with the highest refractive index (and the smallest

average pore sizes) have peak haze values of less than 2%; the lower refractive indices have significantly higher haze values (up to 48%) for approximately the same quantity of the material. Using full-wave optical simulation, together with the synthesis of a model with random networks of NPs with different statistics, the scattering effects are associated with differences in pore size distributions related to different porosities.

6.1 Samples

Silicon (Si) NC thin films were deposited onto various types of substrates via supersonic impaction following the synthesis of Si NCs in a low-pressure silane plasma as discussed in Chap. 2. The film porosity was tuned by adjusting the distance between the exit nozzle and the substrate during deposition, which alters the speed of impaction with the substrate, and therefore the compactness of the resulting film (P. Firth performed the depositions). Table 6.1 summarizes the properties of the samples based on their effective refractive index n_{eff} obtained from ellipsometry measurements (and derived target porosities) for the thin calibration layers. To fit the n_{eff} of the NC films, we assume the refractive index of bulk crystalline silicon (n_{c-Si}) for the individual NCs and that of air ($n_{Air} = 1$) for the voids, extracting the void fraction (f_{Air}) using the Bruggeman effective medium approximation (EMA) model (Eq. 3.17, Chap. 3). Since the layers are measured directly following deposition, the effect of oxidation of silicon NCs, which was previously shown to slightly reduce n_{eff} following annealing, is not considered here. To reduce the effect of absorption (and potential differences in the refractive index of Si NCs and bulk c-Si due to confinement), the fit is performed in the 700–1700 nm wavelength range. The

root mean square error (RMSE) of the acquired ellipsometry data are also included for the full wavelength range.

TABLE 6.1: Summary of the nanoparticle-based layers properties

Target porosity (%)	Refractive index* n_{eff} at 1.2 μm (–)	EMA porosity* f_{Air} (%)	Layer thickness (nm)	RMSE** (–)
~ 70	1.566	69.2 ± 0.01	118.89 ± 0.023	2.02 (7.20)
~ 80	1.310	79.7 ± 0.02	143.66 ± 0.112	3.60 (6.14)
~ 90	1.134	90.6 ± 0.02	304.72 ± 0.354	5.49 (10.3)

*Thin layers measured with ellipsometry, fit performed in 700–1700 nm range.
**Root mean squared error (RMSE) for the fit in 700–1700 nm (350–1700 nm) range.

Figure 6.1 shows the wavelength-dependent n_{eff} and k_{eff} values for the thin calibration films with the derived porosity f_{Air} included in the legend. Directly following the deposition of calibration layers, thicker Si NC layers ($t \approx 6 - 10\ \mu m$) were simultaneously deposited on glass and silicon substrates, as well as aluminum foil sheets for nitrogen adsorption measurements.

6.2 Results and discussion

6.2.1 Physical properties

The physical properties of the NC-based films, specifically their pore size distributions, were investigated using complementary approaches: the analysis of the film vertical cross-sections, which provide a 2D microscopic view of the pores, together with BET, which gives the implied volumetric distribution of pores based on nitrogen adsorption. Pore size distribution (PSD) analysis of the cross-sectional SEM

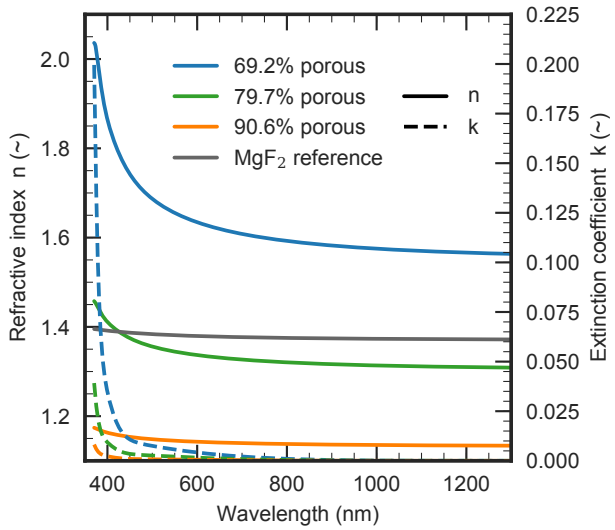

FIG. 6.1: Wavelength-dependent n_{eff} and k_{eff} values are shown for the three deposited Si NC thin films of different porosities. The Bruggeman EMA was used to obtain the n_{eff} and porosity of each film assuming bulk c-Si refractive index for the NCs. The refractive index of magnesium fluoride (MgF_2) is shown for reference.

images—based on the edge-to-edge distance between the bright pixels—was used to compare the three NC samples. Prior to imaging, the samples were cleaved vertically (along the deposition direction). Areas away from the top and bottom surfaces were then imaged (J. Carpenter cleaved the samples and performed the imaging). Figure 6.2(a)–(c) shows the cross-sectional SEM images of the ∼70%, ∼80%, and ∼90% samples, respectively, that were used for the PSD analysis. To perform the analysis, the SEM images were first converted to binary (B&W) images, representing pores and particles. Here, two image thresholding techniques are employed to obtain the binary images: global and local. Global image thresholding is based on the pixel brightness of the entire image—features that arise due to unevenness of the surface are preserved. On the other hand, local image thresholding is based on image segmentation where thresholding is determined for each region independently; as a result, features that arise due to the unevenness of the surface are smoothed over.

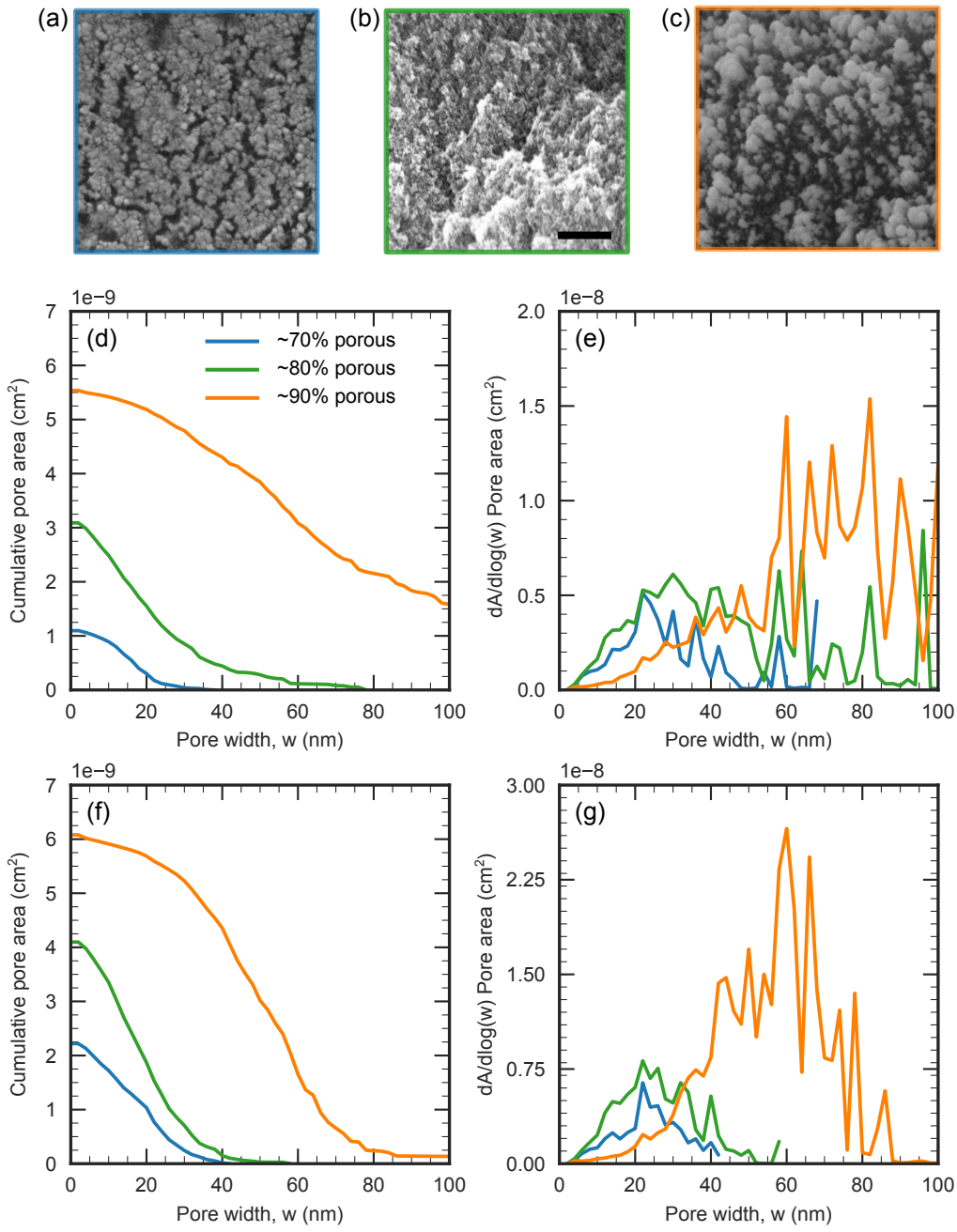

FIG. 6.2: Cross-sectional SEM images of (a) ∼70% porous, (b) ∼80% porous, and (c) ∼90% porous NC layers. The scale bar corresponds to 200 nm (J. Carpenter imaged the samples). Cumulative pore area and pore size distributions of the thresholded cross-sectional SEM images are shown using (d)–(e) global and (f)–(g) local thresholding (thresholded images with pore size distributions are included in the Appendix, Sec. B.1.)

Figures 6.2(d)–(e) and (f)–(g) show the cumulative pore area and pore size distribution when global and local thresholding techniques are used, respectively (the binary (B&W) images, corresponding to global and local image thresholding, are included in the Appendix, Sec. B.1.) Both image sets reveal an increasing pore size distributions width with increasing porosity. In the case of local thresholding, the resulting distributions are narrower, as the effect of the imaged surface unevenness due to cleaving (leading to under- and over- exposure of the image regions) is minimized. The pore size distribution analysis of the images was performed using the Xlib plug-in of the ImageJ software [121, 122].

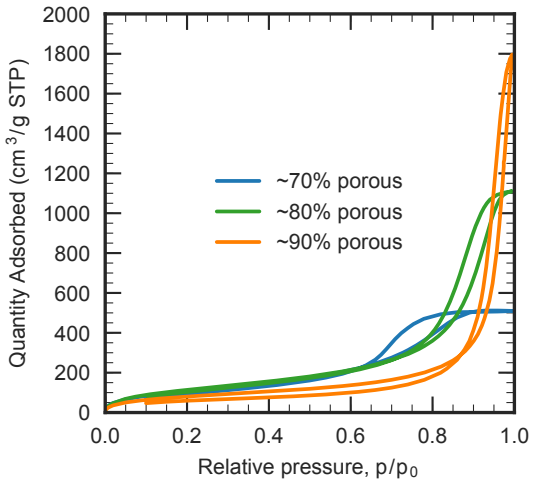

FIG. 6.3: Nitrogen adsorption isotherms at 77 K for the three nanoparticle samples of varying porosities. The data shows the sequential pore filling for lowest, middle, and highest porosity samples.

A complementary approach based on nitrogen adsorption in the pores provides implied volumetric pore size distribution. The volume of nitrogen adsorbed is monitored as pressure is varied, until saturation is reached. The absorption profile is analyzed using a model (BJH in this case) to obtain the pore size distributions (see Sec. 3.4.2 for details). Figure 6.3 shows the nitrogen adsorption isotherms at 77 K

for the three samples—the shape and hysteresis of the adsorption curves are consistent with capillary condensation in mesopores (pores ranging from 2 to 50 nm in width) [113, 115].

TABLE 6.2: Summary of BET nitrogen adsorption measurements for the three layers

EMA porosity* (%)	Cumulative volume of pores** (cm^3/g)	Calculated porosity** (%)	Average pore width** (nm)
69.2 ± 0.01	0.932	68.5 ± 1.4	6.88
79.7 ± 0.02	1.864	81.3 ± 1.2	13.42
90.6 ± 0.02	2.956	87.3 ± 0.9	30.05

*Thin calibration layers measured with ellipsometry.
**Thick layers measured using nitrogen adsorption.

Table 6.2.1 summarizes the results of the BET nitrogen adsorption measurements. We calculate the porosity based on the cumulative volume of pores obtained from nitrogen adsorption and assume the density of c-Si for the nanoparticles using Eq. 6.1 below (the obtained uncertainty is included for the mass measurements ± 1 mg):

$$Porosity[\%] = \frac{Cumulative\,pore\,volume\,[cm^3/g]}{Cumulative\,pore\,volume\,[cm^3/g] + 1/Density_{c-Si}\,[g/cm^3]} \cdot 100 \tag{6.1}$$

The calculated porosities of the three nanoparticle layers are in close agreement with those obtained with the EMA model except for the highest porosity sample, where the derived porosity values using the cumulative pore volume is slightly lower than that obtained with the EMA. Previous results on mesoporous silicon indicate that the EMA model may overestimate the porosity values of the higher porosity samples [123]. The potential impact of surface oxidation on calculated BET poros-

ity[3] is less straightforward; if the oxidation of NCs is accompanied with increase in volume (as suggest by n_{eff} reduction following annealing) accessible pore volume (f_{Air}) may still be reduced. The last column indicates the average pore width of the three samples.

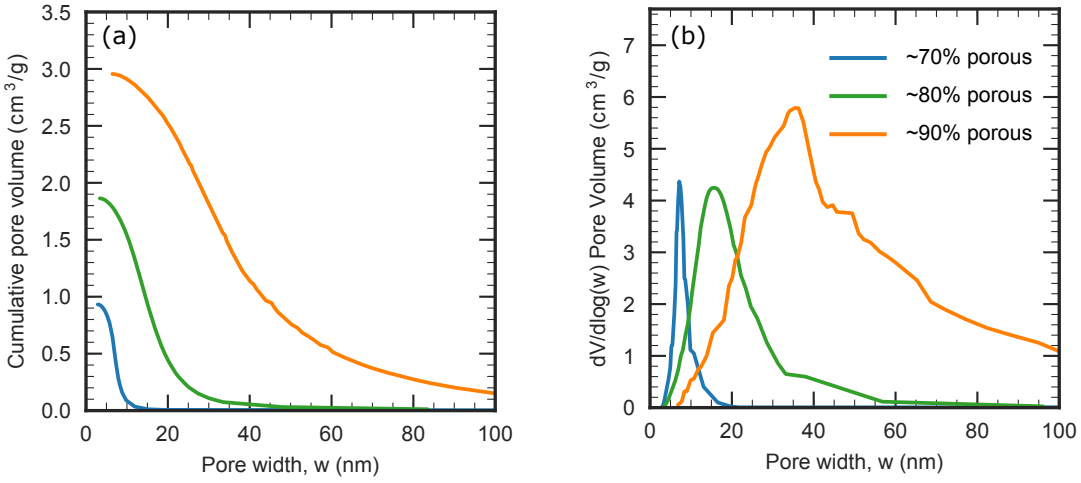

FIG. 6.4: (a) Cumulative pore volume of the three samples and (b) the pore size distributions in the nanoparticle films of different porosities determined through nitrogen adsorption and BJH pore filling analysis.

The derived cumulative pore volume and pore size distributions (using the BJH model) in Figs. 6.4(a) and (b), respectively, show the increase in distribution width with increase in porosity. The tail of the highest porosity sample extends to approximately 250 nm pore width (see Appendix, Sec. B.2). The trends that we observe from BET—wider pore size distributions with increase in porosity—are consistent with the trends we observe in the PSD of the cross-sectional SEM images (Fig. 6.2). However, the BET PSDs are narrower, with a tail extending to larger pore widths. The differences in PSD shape likely arise due to under-counting of the smallest pores

[3]BET measurements were performed > 1 week after deposition, allowing native oxide formation

in the cross-sectional SEM, due to the combination of resolution and thresholding, which results in clusters of NCs appearing as mostly homogeneous (as opposed to made up of individual particles a few nanometers in diameters). The differences between the SEM and BET PSD of the ~70% porous sample may also indicate that the larger trenches observed in the cross-sectional SEM may reveal a surface feature (i.e. surface cracking), as those larger pore sizes are negligible in the BET PSD.

6.2.2 Optical properties

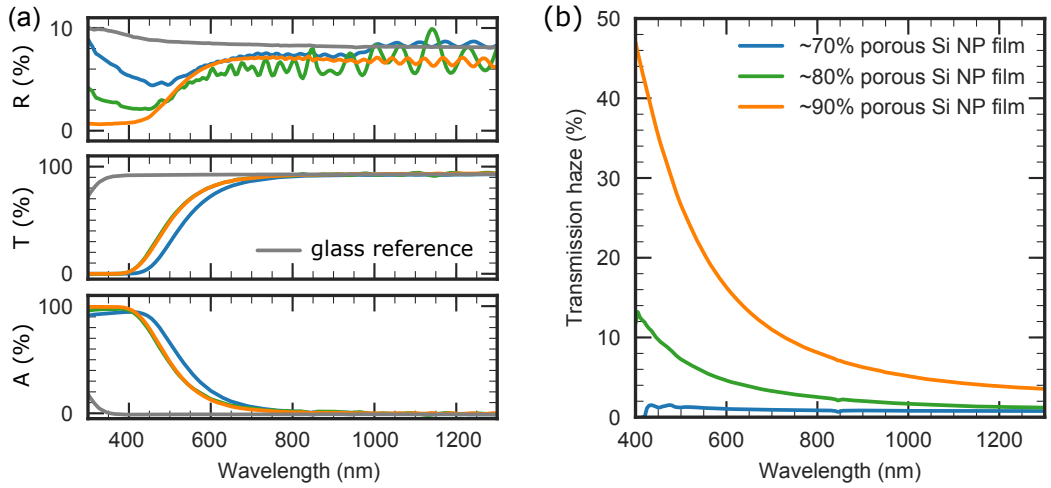

FIG. 6.5: (a) Reflectance, transmittance and absorbtance of thick silicon nanoparticle films ($t_{eff} \approx 1.5\ \mu m$) (b) Corresponding transmission haze measurements showing increasing haze values with increased porosity for approximately similar quantities of material

A spectrophotometer with an integrating sphere was used to measure the total reflection/transmission, transmission haze, and, fitted with directional reflectance/transmittance analyzer, angular intensity distribution profiles (see Sec. 3.2 for details). Figure 6.5(a) shows the reflectance (R), transmittance (T), and absorb-

tance ($1 - R - T$) of the thickest nanoparticle layers deposited on glass substrates. These nanoparticle layers were deposited under the same conditions as the thinner layers used to obtain the n_{eff} and porosity parameters in Fig. 6.1. Figure 6.5(b) shows the corresponding haze values. We observe an overall increase in haze with increase in porosity—the lowest porosity films have peak haze values of less than 2%, while the highest porosity films have significantly higher haze values (over 40%) at shorter wavelengths, where those values are highest. The haze decreases with increasing wavelength for all the samples. For the thinnest samples, the haze becomes negligible. The haze values of the highest porosity sample at different thicknesses are included in the Appendix (Sec. B.3).

While transmission haze compares the diffuse scattering integrated along all angles within a hemisphere (except the aperture window for direct transmission) and compares it to the total transmission through the sample (Fig. 6.5), angular intensity distribution (AID) measurements provide transmission intensities at different angles within a single horizontal plane. As a result, the values we obtain using AID are significantly lower than those we obtain with haze. Figures 6.6(a)–(c) show the corresponding AID of the nanoparticle samples, with the glass substrate shown for reference in d. With AID measurements, we are still able to observe similar trends with increase in porosity as we did with haze measurement, although small differences are harder to detect. Both 70% and 80% porous samples exhibit low levels of scattering, but no differences are apparent between their two angular distributions. The 90% porous film shows increased scattering across the full wavelength range, especially in the 400–800 nm region. These results are consistent with our observations in Fig. 6.5.

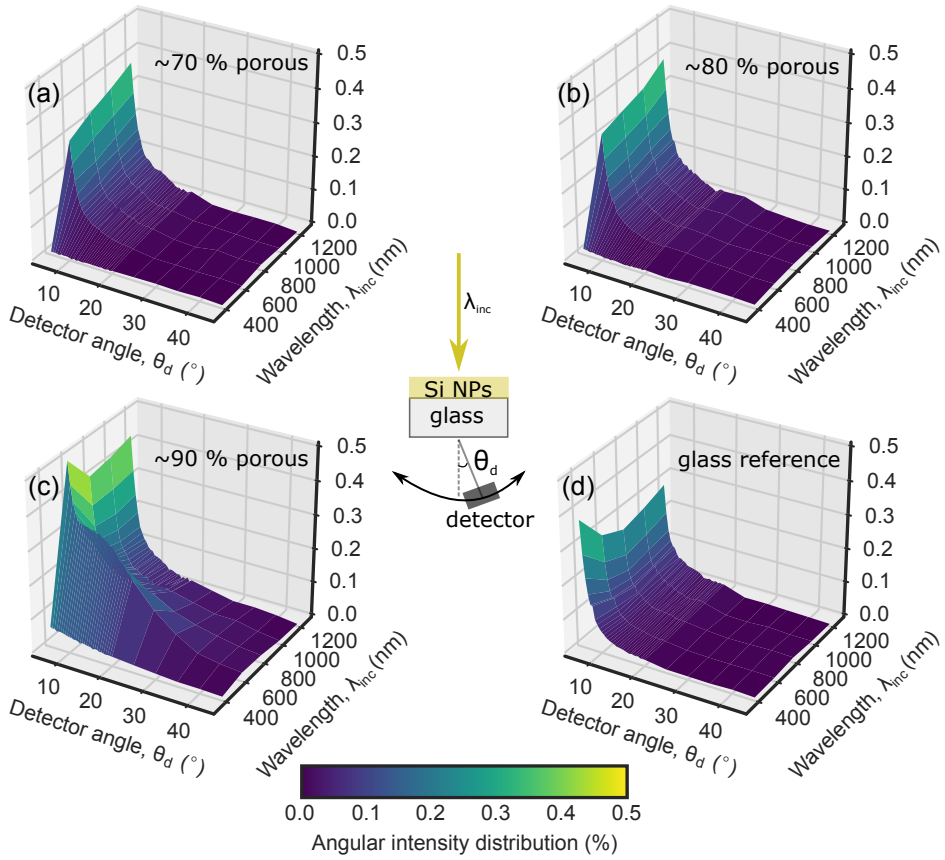

FIG. 6.6: Angle-resolved intensity scattering in transmission through Si nanoparticles films of increasing porosity from (a) to (c) deposited on glass substrates [glass reference is shown in (d)]. The incoming light is normal to the samples and is varied in energy. We observe an increase in non-specular transmission (broader scattering angles) with increasing porosity. These trends agree with the measured haze values.

.

6.3 Optical simulation results

Representative models of the three porous structures (∼70, ∼80, and ∼90%) were created assuming spherical silicon nanoparticles with the same nominal diameter as the experimental case (d=5 nm), to study the impact of the pore size distribution on the optical properties using the FDTD method discussed in Sec. 3.3. To separate the effects of porosity and pore size distribution, two sets of structures were modeled—

random and clustered—using the BET porosity values. Random structures were generated using a rejection algorithm, in which a periodic body centered cubic is generated and then the NPs are randomly removed to obtain the desired porosity. Clustered structures, on the other hand, were generated via the random addition of clusters of particles within the unit cell to achieve the desired porosity. Figure 6.7 shows the modeled structures [(a) random and (b) clustered], with the corresponding top views.

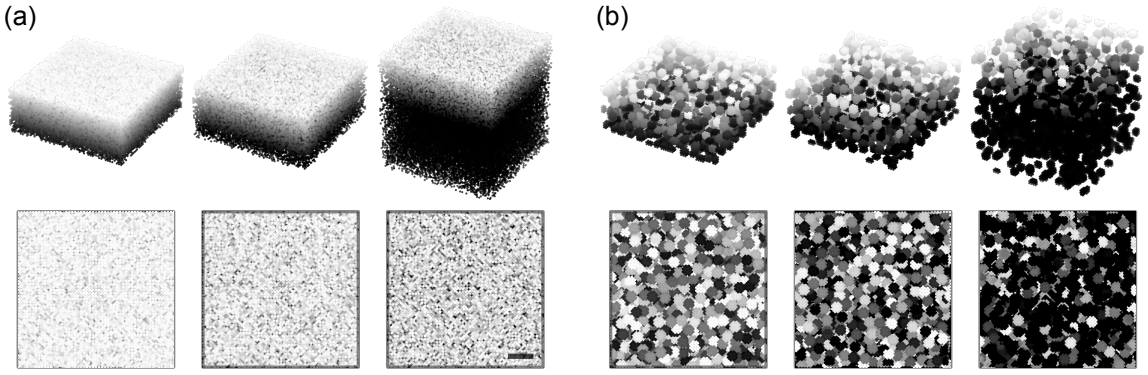

FIG. 6.7: Simulated (a) random and (b) clustered NC structures. The scale bar corresponds to 50 nm.

.

To determine their volume (3D) pore size distributions, PSD analysis was performed on image stacks consisting of individual layers of generated structures. Figure 6.8 shows the resulting PSDs of (a) random and (b) clustered samples; the latter provides a better approximation to the pore size distributions obtained using BET (see Fig. 6.4), especially for the ∼80 and ∼90% samples, with the lowest porosity sample more closely approximated with a random structure.

These structures form unit cells for the FDTD simulations, based on the full-wave solutions of the time-varying electric and magnetic fields. For computation

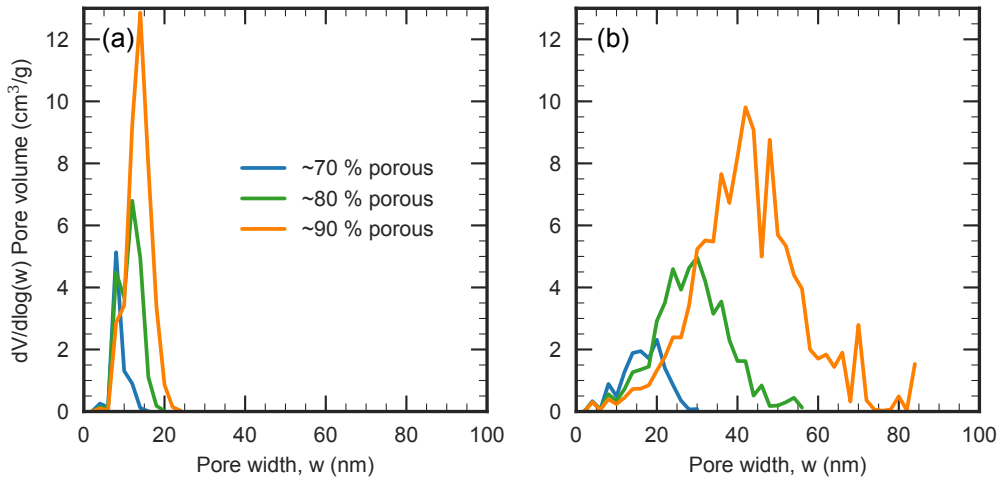

FIG. 6.8: Pore size distribution of simulated sets with (a) random and (b) clustered NC arrangements.

.

of the angular intensity distribution of scattered fields, near to far-field transformation (NFFT) was used on the FDTD solution to eliminate evanescent solutions as discussed in Sec. 3.3. To reduce the computational domain size, we implement periodic boundary conditions (PBCs) in the horizontal plane, which we validated by simulating known sources and structures compared to analytical solutions. In addition, only the thinnest layers are simulated due to computational limitations. From the far-field distributions along a hemisphere, we compute the values corresponding to our optical characterization techniques: (1) transmission haze and (2) in-plane angular intensity distribution.

Figure 6.9 compares the simulated and experimental reflectance, transmittance, absobtance (RTA) of structures with the same porosity and the corresponding electric field energy density for the random structures. Figure 6.10 does the same, but for the clustered structures. When comparing the RTA of the random and clustered structures, the smallest difference is observed for the ∼70% structure. The ∼80%

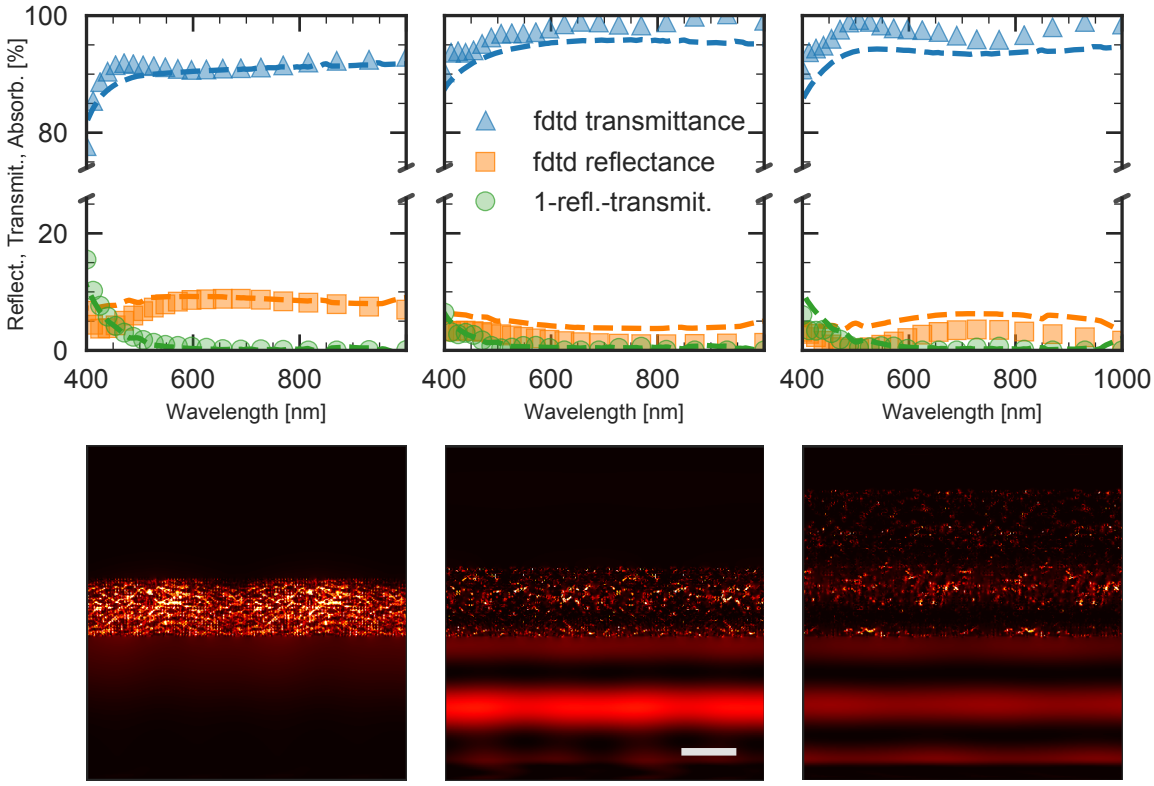

FIG. 6.9: Top row: simulated reflectance/transmittance (markers) compared to measured (dashed lines) for the 70, 80 and 90% random porous samples. Bottom row: corresponding electric field energy density distributions of the three samples. The scale bar corresponds to 100 nm.

.

structure shows a decrease in transmission accompanied by an increase in absorption. The largest difference is observed for the ~90% structure, with clustered structures showing decreased transmission, slightly increased reflection, and increased absorption in the shortest wavelength region (compared to random). The differences between the experimental and simulated RTA, especially with increased reflectance at the SiO_2 interface, partly results from differences in the experimental and simulated reference (see Appendix, Sec. B.4).

The observed differences in the RTA appear related to the differences in scatter-

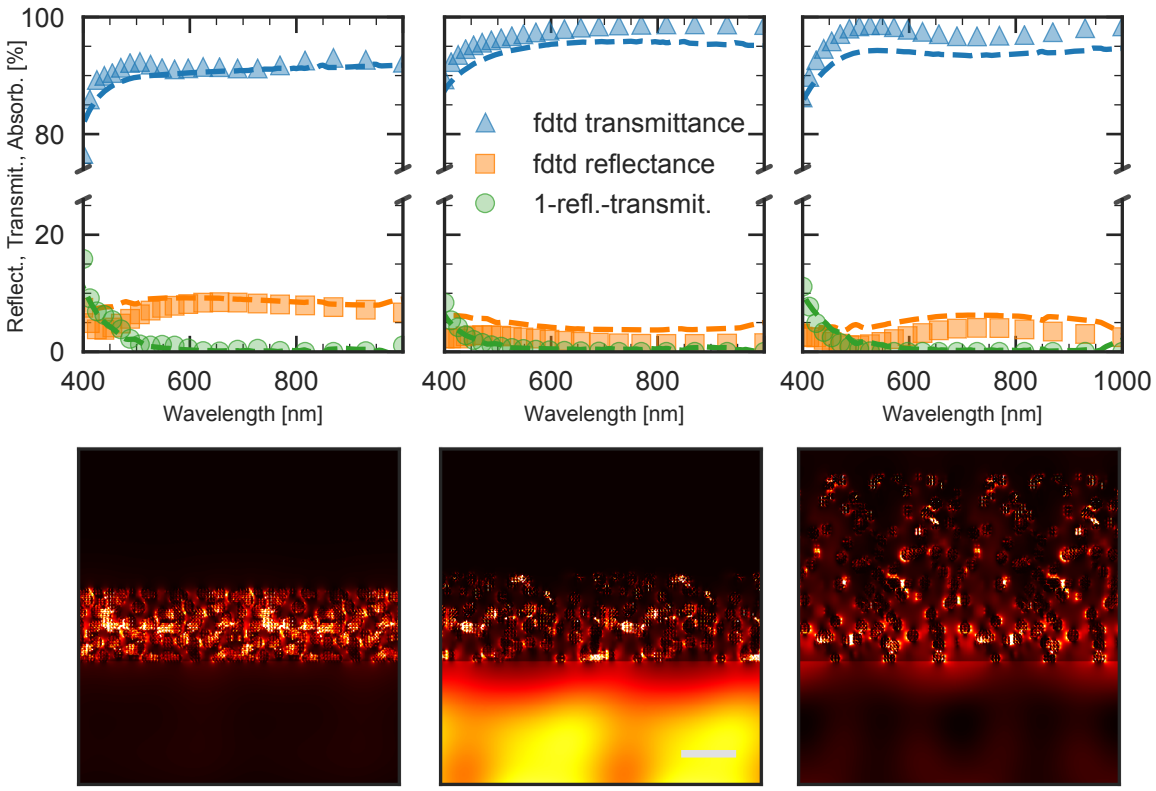

FIG. 6.10: Top row: simulated reflectance/transmittance (markers) compared to measured (dashed lines) for the 70, 80 and 90% clustered porous samples. Bottom row: corresponding simulated electric field energy density distributions of the three samples. The scale bar corresponds to 100 nm.

.

ing that we observe in the cross-sectional electric field energy density profiles for the two sets of structures. Random structures appear not to scatter the normally incident plane wave source—fringes of the plane wave are easily discernible in the SiO_2 layer, especially for the ∼80% and ∼90% structures where reflection is minimized. The corresponding clustered structures, on the other hand, show disruptions to the plane wave fringes, resulting from scattering.

Figure 6.11 shows the simulated angular intensity distribution of the corresponding structures with the air reference shown in the first frame. The full detection-angle range, shown in (a), highlights the differences in direct transmission between

the structures, similar to what is observed in the near-field. In (b), for the reduced detection-angle range ($\theta_d > 7.5°$), similar features are observed for the three samples, with no clear indication of differences in scattering. The ripples observed in these graphs arise from the dimension of the near-field monitor (600 nm x 600 nm), which, physically, acts like an aperture causing strong diffraction. The final result plotted here is the phase-corrected sum of 100 periods, which significantly reduces the broadening arising from diffraction.

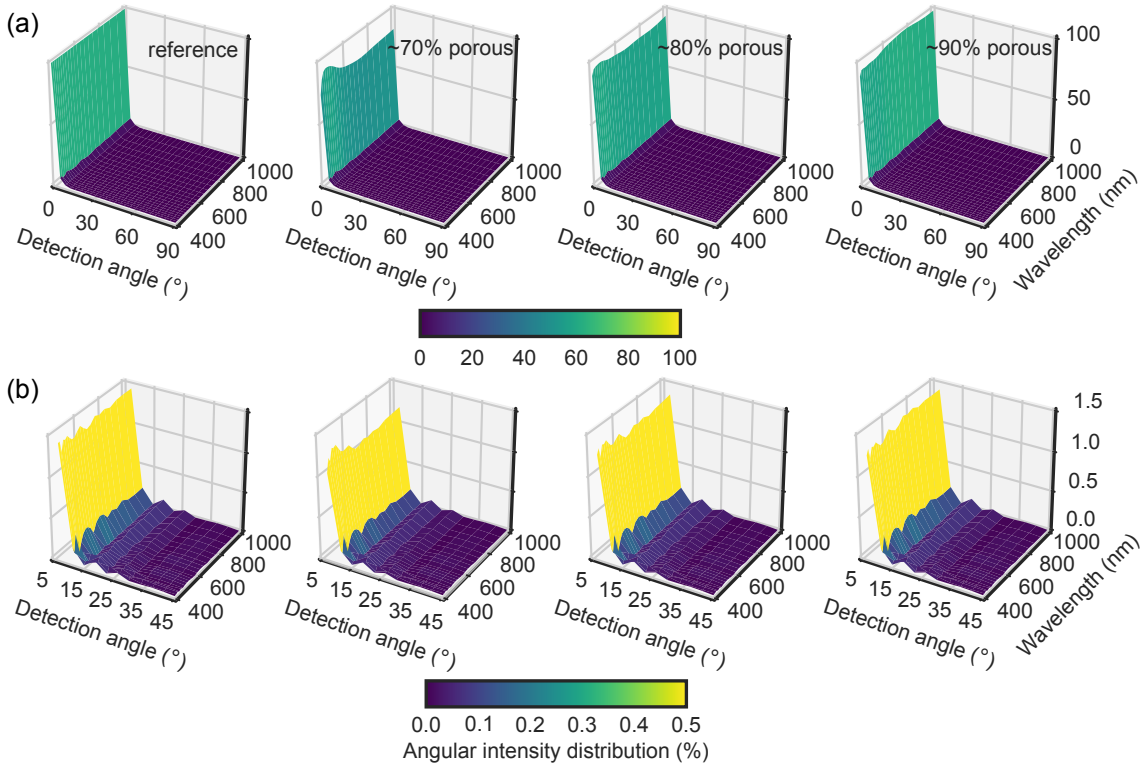

FIG. 6.11: Simulated angular intensity distribution in transmission for (a) the full range of detection angles with respect to the normal and (b) detection angles above 7.5°.

.

Figure 6.12 shows the corresponding simulated haze values, defined as the percentage of diffuse to total transmission ($Haze[\%] = \frac{T_{diffuse}}{T_{total}} \cdot 100$). To reduce the

effect of diffraction peaks on the calculated haze values, the NC structure transmission is normalized to that of air. Differences between the haze value (symbols) of the three samples appear negligible.

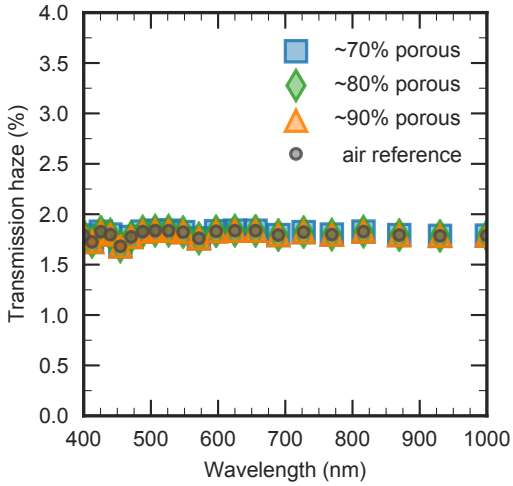

FIG. 6.12: Simulated transmission haze showing negligible differences between different porosity samples.

.

6.4 Summary

In this chapter, NC-based films of various porosities deposited via cluster beam deposition were studied using structural and optical characterization techniques, including an analysis of full-wave optical simulation results of representative structures. The films were first characterized based on their refractive index and porosity using ellipsometry data fitted to the Bruggeman's effective medium approximation model assuming intermixing of crystalline silicon particles and air. Porosity calculations using BET, a complementary volumetric method based on nitrogen adsorption within the voids provided good agreement to the porosity values obtained from EMA, with

differences arising in the highest porosity film. Pore size distributions of the structures, showing increasing width of the distribution with increasing porosity (in addition to the increase in the average pore size), were obtained by applying the BJH model to the evolution of nitrogen adsorption as a function of pressure. SEM images of the vertical cross-sections provided a direct 2D microscopic view of the pore size distributions; the results approximate the trends observed from BJH, but depend on the smoothness of the cleaved surface and the choice of thresholding. In terms of optical properties, higher porosity films show larger haze values indicating increased scattering, as is also observed in the off-normal scattering angles using angular intensity distribution measurements. Presence of scattering, especially in the highest porosity film appears correlated to the wider pore size distributions.

The effect of porosity and pore size distributions on optical properties were studied separately using full-wave optical simulation of modeled structures with different statistics assuming same porosities and nominal particle diameter of the deposited films. Two sets of structures are modeled—random and clustered—with the latter more closely approximating the pore size distributions obtained using BET nitrogen adsorption. Random arrangement of particles, having the smallest pore size distribution width, most closely approximates a homogeneous film; the simulated electric field energy density of the vertical cross-section shows negligible scattering of the normally-incident plane wave as it moves through the structure—even at highest porosity. Clustering of the particles has negligible effect on the lowest porosity layers, as observed with RTA and E-field (compared to the random structures), while increase in absorption and presence of scattering is observed for the highest porosity films. Simulated angular intensity distribution and haze show negligible differences between the samples.

Chapter 7

CONCLUSIONS

This dissertation focused on several types of semiconductor nanostructures — nanowires, nanopillars, and nanoparticles — for potential applications in thin silicon solar cells and silicon-based tandems, with an emphasis on the correlation of their structural and optical properties using combined experimental and simulation approaches. The first results presented showed the impact of wurtzite/zinc-blende polytypism in III-V nanowires on recombination mechanisms using experimental data and a rate equation modeled developed in this dissertation, providing insight into the factors contributing to reduced photovoltaic performance of single NW devices, and ways to improve them, for applications in NW-based solar cells. The most likely reduction in performance of individual NWs is due to the high non-radiative recombination losses from the uncapped surface. The potential losses due to structural inhomogeneity along the length of the NW are minimized with the radial junction geometry since carriers separate in the radial direction where crystal structure is homogeneous and mobility high. Additionally, reduced radiative recombination rates due to spatially indirect recombination of electrons (in ZB segments) and holes (in WZ segments) may be beneficial to carrier collection: the increased diffusion length of carriers due to suppressed radiative recombination increases the probability of carrier collection before the excited carriers recombine. Nevertheless, the structural inhomogeneity along the length of the NW is still expected to present an issue for carrier extraction at the contacts, where carriers must travel in the direction of low

carrier mobility to reach them. To maximize carrier extraction in highly polytype NWs, a transparent conductive oxide (TCO) conformal to the NWs is needed.

The results on the optical properties of silicon nanopillar arrays presented an analysis of mechanisms with potential for light-trapping (of poorly absorbing near-bandgap light) in ultra-thin silicon solar cells and silicon-based tandems, starting with full-wave optical simulation compared to the measured reflectance data. Simulated structures showing good agreement to measured reflectance were used to investigate the mechanisms leading to its reduction (when compared to planar substrates). The simulated electric field energy density profiles of the structures' cross-sections suggest strong forward scattering for short-aspect ratio nanopillars, with resonance absorption within and diffraction patterns between the nanopillars for the high-aspect ratio nanopillars. Complimentary analysis revealed a high percentage of transmitted light at off-normal angles for the poorly absorbed light, suggesting the suitability of nanopillars for light-trapping in ultra-thin silicon substrates. The results from the simulated test structures with $\sim \ 1\mu m$ thickness and perfectly reflective back confirmed these suggestions, showing that conventional light-trapping limit can be exceeded for certain wavelengths, approaching the limit in the 700–1000 nm range for normally incident light.

Finally, the presented results on the optical properties of nanoparticle-based silicon thin films showed the impact of pore size distribution on scattering using structural and optical characterization techniques combined with full-wave optical simulation. Porosity values derived using ellipsometry showed good agreement with the more direct nitrogen adsorption method, with discrepancies arising for the highest porosity. Results from the complementary nitrogen adsorption and cross-sectional SEM analysis showed a significant increase in pore size distribution with increase in

porosity. These differences in structure appeared to cause scattering in thick films, observed using transmission haze and angular intensity distribution measurements. The effects of porosity and pore size distribution were studied separately using full-wave optical simulation of thin films composed of random and clustered arrangements of particles, with the latter more closely approximating the experimental structures. Simulated absorption and the electric field energy density profiles of the films are compared for the two cases: the E-field profiles for random arrangements of particles show negligible effect on scattering due to their small size; with clustering, the two lowest porosity layers show negligible change in the film absorption and scattering, while the highest porosity film shows increased absorption and the presence of scattering. The onset of scattering appears related to the larger deviation from a random arrangement of nanoparticles for the highest porosity film (as observed from the simulated pore size distributions of the random and clustered structures): the inter-dispersion of particles and air is reduced, making the film less homogeneous and creating scattering centers. Used as an inter-layer at the metal/semiconductor interface, the inhomogeneity of the layer is expected to reduce the reflectance at the layer/semiconductor interface; the light transmitted through the interface would more likely get trapped in the layer inducing higher plasmonic losses. The methodology for studying nanoparticle-based systems presented here can be expanded to other applications in solar cells (e.g. anti-reflection optical coatings at the front surface) and other material systems (e.g. dielectric and metalic nanoparticle-based structures).

REFERENCES

[1] *Electricity information: Overview* (International Energy Agency, 2018).

[2] IPCC, *Climate change 2014: Synthesis report. Contribution of working groups I, II and III to the fifth assessment report of the Intergovernmental Panel on Climate Change* (IPCC, Geneva, Switzerland, 2014).

[3] IEA, *Renewables in 2018: Analysis and forcasts to 2023*, Market Report (International Energy Agency, 2018).

[4] R. Fu, R. M. Margolis, and D. J. Feldman, *US solar photovoltaic system cost benchmark: Q1 2018*, tech. rep. (National Renewable Energy Lab.(NREL), Golden, CO (United States), 2018).

[5] *Transparent cost database*, Open Energy Information, 2014.

[6] J. Nelson, *The physics of solar cells* (World Scientific Publishing Company, 2003).

[7] T. N. Tibbits, P. Beutel, M. Grave, C. Karcher, E. Oliva, G. Siefer, A. Wekkeli, M. Schachtner, F. Dimroth, A. W. Bett, et al., "New efficiency frontiers with wafer-bonded multi-junction solar cells", in 29th European PV Solar Energy Conference and Exhibition (Amsterdam, Netherlands, 2014), pp. 1–4.

[8] M. A. Green, K. Emery, Y. Hishikawa, W. Warta, E. D. Dunlop, D. H. Levi, and A. W. Y. Ho-Baillie, "Solar cell efficiency tables (version 49)", Progress in Photovoltaics: Research and Applications **25**, 3–13 (2017).

[9] W. Shockley and H. J. Queisser, "Detailed balance limit of efficiency of p-n junction solar cells", Journal of Applied Physics **32**, 510–519 (1961).

[10] A. Nozik, "Exciton multiplication and relaxation dynamics in quantum dots: applications to ultrahigh-efficiency solar photon conversion", Inorganic chemistry **44**, 6893–6899 (2005).

[11] O. E. Semonin, J. M. Luther, S. Choi, H.-Y. Chen, J. Gao, A. J. Nozik, and M. C. Beard, "Peak external photocurrent quantum efficiency exceeding 100% via MEG in a quantum dot solar cell", Science **334**, 1530–1533 (2011).

[12] R. Hathwar, M. Saraniti, and S. M. Goodnick, "Energy relaxation and non-linear transport in InAs nanowires", in Journal of physics: conference series, Vol. 647, 1 (IOP Publishing, 2015), p. 012029.

[13]A. Luque and A. Martí, "Increasing the efficiency of ideal solar cells by photon induced transitions at intermediate levels", Physical Review Letters **78**, 5014 (1997).

[14]R. T. Ross and A. J. Nozik, "Efficiency of hot-carrier solar energy converters", Journal of Applied Physics **53**, 3813–3818 (1982).

[15]W. Pelouch, R. Ellingson, P. Powers, C. Tang, D. Szmyd, and A. Nozik, "Comparison of hot-carrier relaxation in quantum wells and bulk GaAs at high carrier densities", Physical Review B **45**, 1450 (1992).

[16]S. M. Goodnick and P. Lugli, "Hot carrier relaxation in quasi-2D systems", in *Hot carriers in semiconductor nanostructures*, edited by J. Shah (Academic Press, 1992), pp. 191–234.

[17]E. Yablonovitch, "Statistical ray optics", Journal of the Optical Society of America **72**, 899–907 (1982).

[18]M. D. Kelzenberg, S. W. Boettcher, J. A. Petykiewicz, D. B. Turner-Evans, M. C. Putnam, E. L. Warren, J. M. Spurgeon, R. M. Briggs, N. S. Lewis, and H. A. Atwater, "Enhanced absorption and carrier collection in si wire arrays for photovoltaic applications", Nature Materials **9**, 239 (2010).

[19]E. Garnett and P. Yang, "Light trapping in silicon nanowire solar cells", Nano Letters **10**, 1082–1087 (2010).

[20]S. E. Han and G. Chen, "Toward the lambertian limit of light trapping in thin nanostructured silicon solar cells", Nano Letters **10**, 4692–4696 (2010).

[21]P. N. Saeta, V. E. Ferry, D. Pacifici, J. N. Munday, and H. A. Atwater, "How much can guided modes enhance absorption in thin solar cells?", Optics Express **17**, 20975–20990 (2009).

[22]A. Chutinan, N. P. Kherani, and S. Zukotynski, "High-efficiency photonic crystal solar cell architecture", Optics Express **17**, 8871–8878 (2009).

[23]Z. Yu, A. Raman, and S. Fan, "Fundamental limit of light trapping in grating structures", Optics Express **18**, A366–A380 (2010).

[24]Z. Yu, A. Raman, and S. Fan, "Fundamental limit of nanophotonic light trapping in solar cells", Proceedings of the National Academy of Sciences **107**, 17491–17496 (2010).

[25]D. M. Callahan, J. N. Munday, and H. A. Atwater, "Solar cell light trapping beyond the ray optic limit", Nano Letters **12**, 214–218 (2012).

[26]P. Krogstrup, H. I. Jorgensen, M. Heiss, O. Demichel, J. V. Holm, M. Aagesen, J. Nygard, and A. Fontcuberta i Morral, "Single-nanowire solar cells beyond the Shockley-Queisser limit", Nature Photonics **7**, 306–310 (2013).

[27]Y. Xu, T. Gong, and J. N. Munday, "The generalized Shockley-Queisser limit for nanostructured solar cells", Scientific Reports **5**, 13536 (2015).

[28]M. Heiss, E. Russo-Averchi, A. Dalmau-Mallorquí, G. Tütüncüoğlu, F. Matteini, D. Rüffer, S. Conesa-Boj, O. Demichel, E. Alarcon-Lladó, and A. Fontcuberta i Morral, "III-V nanowire arrays: growth and light interaction", Nanotechnology **25**, 014015 (2013).

[29]K. T. Fountaine, C. G. Kendall, and H. A. Atwater, "Near-unity broadband absorption designs for semiconducting nanowire arrays via localized radial mode excitation", Optics Express **22**, A930–A940 (2014).

[30]P. Spinelli, M. A. Verschuuren, and A. Polman, "Broadband omnidirectional antireflection coating based on subwavelength surface Mie resonators", Nature Communications **3**, 692 (2012).

[31]M. Boccard, P. Firth, Z. J. Yu, K. C. Fisher, M. Leilaeioun, S. Manzoor, and Z. C. Holman, "Low-refractive-index nanoparticle interlayers to reduce parasitic absorption in metallic rear reflectors of solar cells", physica status solidi (a), 1700179 (2017).

[32]P. Spinelli and A. Polman, "Light trapping in thin crystalline si solar cells using surface mie scatterers", IEEE Journal of Photovoltaics **4**, 554–559 (2014).

[33]T. Tiedje, E. Yablonovitch, G. D. Cody, and B. G. Brooks, "Limiting efficiency of silicon solar cells", IEEE Transactions on Electron Devices **31**, 711–716 (1984).

[34]J. Oh, H.-C. Yuan, and H. M. Branz, "An 18.2%-efficient black-silicon solar cell achieved through control of carrier recombination in nanostructures", Nature Nanotechnology **7**, 743–748 (2012).

[35]K. A. Bush, A. F. Palmstrom, Z. J. Yu, M. Boccard, R. Cheacharoen, J. P. Mailoa, D. P. McMeekin, R. L. Z. Hoye, C. D. Bailie, T. Leijtens, I. M. Peters, M. C. Minichetti, N. Rolston, R. Prasanna, S. Sofia, D. Harwood, W. Ma, F. Moghadam, H. J. Snaith, T. Buonassisi, Z. C. Holman, S. F. Bent, and M. D. McGehee, "23.6%-efficient monolithic perovskite/silicon tandem solar cells with improved stability", Nature Energy **2**, 17009 (2017).

[36]B. M. Kayes, H. A. Atwater, and N. S. Lewis, "Comparison of the device physics principles of planar and radial p-n junction nanorod solar cells", Journal of Applied Physics **97**, 114302–114302 (2005).

[37]S. Yu, F. Roemer, and B. Witzigmann, "Analysis of surface recombination in nanowire array solar cells", Journal of Photonics for Energy **2**, 028002–1 (2012).

[38]R. Wagner and W. Ellis, "Vapor-liquid-solid mechanism of single crystal growth", Applied Physics Letters **4**, 89–90 (1964).

[39]C. Colombo, D. Spirkoska, M. Frimmer, G. Abstreiter, and A. Fontcuberta i Morral, "Ga-assisted catalyst-free growth mechanism of GaAs nanowires by molecular beam epitaxy", Physical Review B **77**, 155326 (2008).

[40]L. J. Lauhon, M. S. Gudiksen, D. Wang, and C. M. Lieber, "Epitaxial core-shell and core-multishell nanowire heterostructures", Nature **420**, 57 (2002).

[41]M. Heigoldt, J. Arbiol, D. Spirkoska, J. M. Rebled, S. Conesa-Boj, G. Abstreiter, F. Peiró, J. R. Morante, and A. Fontcuberta i Morral, "Long range epitaxial growth of prismatic heterostructures on the facets of catalyst-free GaAs nanowires", Journal of Materials Chemistry **19**, 840 (2009).

[42]Y. Fontana, "Optically active quantum dots in bottom-up nanowires", PhD thesis (École Polytechnique Fédéralé de Lausanne, 2015).

[43]E. C. Garnett, M. L. Brongersma, Y. Cui, and M. D. McGehee, "Nanowire solar cells", Annual Review of Materials Research **41**, 269–295 (2011).

[44]R. R. LaPierre, A. C. E. Chia, S. J. Gibson, C. M. Haapamaki, J. Boulanger, R. Yee, P. Kuyanov, J. Zhang, N. Tajik, N. Jewell, and K. M. A. Rahman, "III-V nanowire photovoltaics: review of design for high efficiency", Physica Status Solidi Rapid Research Letters **7**, 815–830 (2013).

[45]S. M. Goodnick, "Nanotechnology pathways to next-generation photovoltaics", in *Semiconductor nanotechnology* (Springer, 2018), pp. 1–36.

[46]A. Standing, S. Assali, L. Gao, M. A. Verheijen, D. Van Dam, Y. Cui, P. H. Notten, J. E. Haverkort, and E. P. Bakkers, "Efficient water reduction with gallium phosphide nanowires", Nature communications **6**, 7824 (2015).

[47]J. Wu, Y. Li, J. Kubota, K. Domen, M. Aagesen, T. Ward, A. Sanchez, R. Beanland, Y. Zhang, M. Tang, et al., "Wafer-scale fabrication of self-catalyzed 1.7 eV GaAsP

core-shell nanowire photocathode on silicon substrates", Nano Letters **14**, 2013–2018 (2014).

[48]S. Hu, C.-Y. Chi, K. T. Fountaine, M. Yao, H. A. Atwater, P. D. Dapkus, N. S. Lewis, and C. Zhou, "Optical, electrical, and solar energy-conversion properties of gallium arsenide nanowire-array photoanodes", Energy & Environmental Science **6**, 1879–1890 (2013).

[49]L. Cao, J. S. White, J.-S. Park, J. A. Schuller, B. M. Clemens, and M. L. Brongersma, "Engineering light absorption in semiconductor nanowire devices", Nature Materials **8**, 643 (2009).

[50]C. Colombo, M. Heiss, M. Grätzel, and A. Fontcuberta i Morral, "Gallium arsenide p-i-n radial structures for photovoltaic applications", Applied Physics Letters **94**, 173108 (2009).

[51]L. C. Chuang, F. G. Sedgwick, R. Chen, W. S. Ko, M. Moewe, K. W. Ng, T.-T. D. Tran, and C. Chang-Hasnain, "GaAs-based nanoneedle light emitting diode and avalanche photodiode monolithically integrated on a silicon substrate", Nano Letters **11**, 385–390 (2010).

[52]M. A. Green, "Third generation photovoltaics: ultra-high conversion efficiency at low cost", Progress in Photovoltaics: Research and Applications **9**, 123–135 (2001).

[53]M. Woodhouse and A. Goodrich, *A manufacturing cost analysis relevant to single-and dual-junction photovoltaic cells fabricated with III-Vs and III-Vs grown on Czochralski silicon*, tech. rep. (National Renewable Energy Laboratory, 2013).

[54]F. Matteini, G. Tütüncüoğlu, H. Potts, F. Jabeen, and A. Fontcuberta i Morral, "Wetting of Ga on SiOx and its impact on GaAs nanowire growth", Crystal Growth & Design **15**, 3105–3109 (2015).

[55]I. Åberg, G. Vescovi, D. Asoli, U. Naseem, J. P. Gilboy, C. Sundvall, A. Dahlgren, K. E. Svensson, N. Anttu, M. T. Björk, et al., "A GaAs nanowire array solar cell with 15.3% efficiency at 1 Sun", IEEE Journal of Photovoltaics **6**, 185–190 (2016).

[56]D. van Dam, N. J. J. van Hoof, Y. Cui, P. J. van Veldhoven, E. P. A. M. Bakkers, J. Gómez Rivas, and J. E. M. Haverkort, "High-efficiency nanowire solar cells with omnidirectionally enhanced absorption due to self-aligned indium-tin-oxide Mie scatterers", ACS Nano **10**, 11414–11419 (2016).

[58]P. Krogstrup, R. Popovitz-Biro, E. Johnson, M. H. Madsen, J. Nygård, and H. Shtrikman, "Structural phase control in self-catalyzed growth of GaAs nanowires on silicon (111)", Nano Letters **10**, 4475–4482 (2010).

[59]D. Jacobsson, F. Panciera, J. Tersoff, M. C. Reuter, S. Lehmann, S. Hofmann, K. A. Dick, and F. M. Ross, "Interface dynamics and crystal phase switching in GaAs nanowires", Nature **531**, 317 (2016).

[60]M. Murayama and T. Nakayama, "Chemical trend of band offsets at wurtzite/zinc-blende heterocrystalline semiconductor interfaces", Physical Review B **49**, 4710–4724 (1994).

[61]A. De and C. E. Pryor, "Predicted band structures of III-V semiconductors in the wurtzite phase", Physical Review B **81**, 155210 (2010).

[62]J. L. Birman, "Simplified LCAO method for zincblende, wurtzite, and mixed crystal structures", Physical Review **115**, 1493–1505 (1959).

[63]D. Spirkoska, J. Arbiol, A. Gustafsson, S. Conesa-Boj, F. Glas, I. Zardo, M. Heigoldt, M. Gass, A. L. Bleloch, S. Estrade, M. Kaniber, J. Rossler, F. Peiro, J. Morante, G. Abstreiter, L. Samuelson, and A. Fontcuberta i Morral, "Structural and optical properties of high quality zinc-blende/wurtzite GaAs nanowire heterostructures", Physical Review B **80**, 245325 (2009).

[64]P. Corfdir, B. Van Hattem, E. Uccelli, A. Fontcuberta i Morral, and R. T. Phillips, "Charge carrier generation, relaxation, and recombination in polytypic GaAs nanowires studied by photoluminescence excitation spectroscopy", Applied Physics Letters **103**, 133109 (2013).

[65]A. M. Graham, P. Corfdir, M. Heiss, S. Conesa-Boj, E. Uccelli, A. Fontcuberta i Morral, and R. T. Phillips, "Exciton localization mechanisms in wurtzite/zinc-blende GaAs nanowires", Physical Review B **87**, 125304 (2013).

[66]N. Vainorius, S. Lehmann, D. Jacobsson, L. Samuelson, K. A. Dick, and M.-E. Pistol, "Confinement in thickness-controlled GaAs polytype nanodots", Nano Letters **15**, 2652–2656 (2015).

[67]B. Loitsch, M. Müller, J. Winnerl, P. Veit, D. Rudolph, G. Abstreiter, J. J. Finley, F. Bertram, J. Christen, and G. Koblmüller, "Microscopic nature of crystal phase quantum dots in ultrathin GaAs nanowires by nanoscale luminescence characterization", New Journal of Physics **18**, 063009 (2016).

[68]M. Heiss, S. Conesa-Boj, J. Ren, H.-H. Tseng, A. Gali, A. Rudolph, E. Uccelli, F. Peiró, J. R. Morante, D. Schuh, E. Reiger, E. Kaxiras, J. Arbiol, and A. Fontcuberta i Morral, "Direct correlation of crystal structure and optical properties in wurtzite/zinc-blende gaas nanowire heterostructures", Physical Review B **83**, 045303 (2011).

[69]N. Akopian, G. Patriarche, L. Liu, J.-C. Harmand, and V. Zwiller, "Crystal phase quantum dots", Nano Letters **10**, 1198–1201 (2010).

[70]O. Demichel, M. Heiss, J. Bleuse, H. Mariette, and A. Fontcuberta i Morral, "Impact of surfaces on the optical properties of GaAs nanowires", Applied Physics Letters **97**, 201907 (2010).

[71]L. M. Ephrath, "Reactive ion etching", US Patent No 4,283,249 (1981).

[72]Z. Huang, N. Geyer, P. Werner, J. de Boor, and U. Gösele, "Metal-assisted chemical etching of silicon: a review", Advanced Materials **23**, 285–308 (2011).

[73]S. Y. Chou, P. R. Krauss, and P. J. Renstrom, "Nanoimprint lithography", Journal of Vacuum Science & Technology B: Microelectronics and Nanometer Structures Processing, Measurement, and Phenomena **14**, 4129–4133 (1996).

[74]Z. Huang, H. Fang, and J. Zhu, "Fabrication of silicon nanowire arrays with controlled diameter, length, and density", Advanced Materials **19**, 744–748 (2007).

[75]J.-Y. Choi, T. L. Alford, and C. B. Honsberg, "Solvent-controlled spin-coating method for large-scale area deposition of two-dimensional silica nanosphere assembled layers", Langmuir **30**, 5732–5738 (2014).

[76]J.-Y. Choi, T. L. Alford, and C. B. Honsberg, "Fabrication of periodic silicon nanopillars in a two-dimensional hexagonal array with enhanced control on structural dimension and period", Langmuir **31**, 4018–4023 (2015).

[77]G. Mie, "Beiträge zur optik trüber medien, speziell kolloidaler metallösungen", Annalen der physik **330**, 377–445 (1908).

[78]N. Vulic, J. Y. Choi, C. B. Honsberg, and S. M. Goodnick, "Silica nanosphere lithography defined light trapping structures for ultra-thin Si photovoltaics", MRS Proceedings **1770**, 31–36 (2015).

[79]J. Y. Choi, N. Vulic, S. Goodnick, and C. B. Honsberg, "Enhanced forward scattering and transmitted light diffraction in low aspect-ratio Si nanopillars for high

efficiency si solar cells", in 2015 IEEE 42nd Photovoltaic Specialist Conference (PVSC) (2015), pp. 1–5.

[80]L. Mangolini, E. Thimsen, and U. Kortshagen, "High-yield plasma synthesis of luminescent silicon nanocrystals", Nano Letters **5**, 655–659 (2005).

[81]Z. C. Holman and U. R. Kortshagen, "A flexible method for depositing dense nanocrystal thin films: impaction of germanium nanocrystals", Nanotechnology **21**, 335302 (2010).

[82]A. Cullis, L. T. Canham, and P. Calcott, "The structural and luminescence properties of porous silicon", Journal of Applied Physics **82**, 909–965 (1997).

[83]N. N. Ledentsov, V. M. Ustinov, V. A. Shchukin, P. S. Kop'ev, Z. I. Alferov, and D. Bimberg, "Quantum dot heterostructures: fabrication, properties, lasers (review)", Semiconductors **32**, 343–365 (1998).

[84]H.-C. Yuan, V. E. Yost, M. R. Page, P. Stradins, D. L. Meier, and H. M. Branz, "Efficient black silicon solar cell with a density-graded nanoporous surface: optical properties, performance limitations, and design rules", Applied Physics Letters **95**, 123501 (2009).

[85]P. Menna, G. D. Francia, and V. L. Ferrara, "Porous silicon in solar cells: a review and a description of its application as an ar coating", Solar Energy Materials and Solar Cells **37**, 13–24 (1995).

[86]F. A. Harraz, "Porous silicon chemical sensors and biosensors: a review", Sensors and Actuators B: Chemical **202**, 897–912 (2014).

[87]J. Hernández-Montelongo, A. Muñoz-Noval, J. P. García-Ruíz, V. Torres-Costa, R. J. Martín-Palma, and M. Manso-Silván, "Nanostructured porous silicon: the winding road from photonics to cell scaffolds - a review", Frontiers in Bioengineering and Biotechnology **3**, 60–60 (2015).

[88]J. H. Fendler, *Nanoparticles and nanostructured films: preparation, characterization, and applications* (John Wiley & Sons, 2008).

[89]R. Khazaka, E. Moulin, M. Boccard, L. Garcia, S. Hänni, F.-J. Haug, F. Meillaud, and C. Ballif, "Silver versus white sheet as a back reflector for microcrystalline silicon solar cells deposited on LPCVD-ZnO electrodes of various textures", Progress in Photovoltaics: Research and Applications **23**, 1182–1189 (2015).

[90]D. O'Connor, *Time-correlated single photon counting* (Academic Press, 2012).

[91]M. Wahl, *Time-correlated single photon counting*, tech. rep. (Pico Quant, 2014).

[92]F. W. Billmeyer and Y. Chen, "On the measurement of haze", Color Research & Application **10**, 219–224 (1985).

[93]P. Van Nijnatten, "An automated directional reflectance/transmittance analyser for coating analysis", Thin Solid Films **442**, 74–79 (2003).

[94]K. Yee, "Numerical solution of initial boundary value problems involving Maxwell's equations in isotropic media", IEEE Transactions on Antennas and Propagation **14**, 302–307 (1966).

[95]A. Taflove, "Application of the finite-difference time-domain method to sinusoidal steady-state electromagnetic-penetration problems", IEEE Transactions on Electromagnetic Compatibility, 191–202 (1980).

[96]A. Oskooi and S. G. Johnson, "Electromagnetic wave source conditions", arXiv preprint (2013).

[97]A. F. Oskooi, D. Roundy, M. Ibanescu, P. Bermel, J. D. Joannopoulos, and S. G. Johnson, "Meep: a flexible free-software package for electromagnetic simulations by the FDTD method", Computer Physics Communications **181**, 687–702 (2010).

[98]A. Deinega, I. Valuev, B. Potapkin, and Y. Lozovik, "Minimizing light reflection from dielectric textured surfaces", Journal of the Optical Society of America A, Optics and Image Science **28**, 770–777 (2011).

[99]M. A. Green and M. J. Keevers, "Optical properties of intrinsic silicon at 300 k", Progress in Photovoltaics: Research and Applications **3**, 189–192 (1995).

[100]C. A. Balanis, *Advanced engineering electromagnetics* (John Wiley & Sons, 1999).

[101]J.-P. Berenger, "A perfectly matched layer for the absorption of electromagnetic waves", Journal of Computational Physics **114**, 185–200 (1994).

[102]A. Oskooi and S. G. Johnson, "Distinguishing correct from incorrect PML proposals and a corrected unsplit PML for anisotropic, dispersive media", Journal of Computational Physics **230**, 2369–2377 (2011).

[103]Z. S. Sacks, D. M. Kingsland, R. Lee, and J.-F. Lee, "A perfectly matched anisotropic absorber for use as an absorbing boundary condition", IEEE Transactions on Antennas and Propagation **43**, 1460–1463 (1995).

[104]A. F. Oskooi, L. Zhang, Y. Avniel, and S. G. Johnson, "The failure of perfectly matched layers, and towards their redemption by adiabatic absorbers", Optics Express **16**, 11376–11392 (2008).

[105]J. D. Joannopoulos, S. G. Johnson, J. N. Winn, and R. D. Meade, *Photonic crystals: Molding the flow of light*, Second (Princeton University Press, Princeton, New Jersey, 2008).

[106]A. Taflove, A. Oskooi, and S. G. Johnson, *Advances in FDTD computational electrodynamics, Photonics and nanotechnology* (Artech house, 2013) Chap. 4.

[107]V. D. Bruggeman, "Berechnung verschiedener physikalischer Konstanten von heterogenen Substanzen. I. Dielektrizitätskonstanten und Leitfähigkeiten der Mischkörper aus isotropen Substanzen", Annalen der Physik **416**, 636–664 (1935).

[108]M. M. Braun and L. Pilon, "Effective optical properties of non-absorbing nanoporous thin films", Thin Solid Films **496**, 505–514 (2006).

[109]G. A. Niklasson, C. Granqvist, and O. Hunderi, "Effective medium models for the optical properties of inhomogeneous materials", Applied Optics **20**, 26–30 (1981).

[110]S. Brunauer, P. H. Emmett, and E. Teller, "Adsorption of gases in multimolecular layers", Journal of the American Chemical Society **60**, 309–319 (1938).

[111]E. P. Barrett, L. G. Joyner, and P. P. Halenda, "The determination of pore volume and area distributions in porous substances. I. Computations from nitrogen isotherms", Journal of the American Chemical Society **73**, 373–380 (1951).

[112]M. Thommes, K. Kaneko, A. V. Neimark, J. P. Olivier, F. Rodriguez-Reinoso, J. Rouquerol, and K. S. Sing, "Physisorption of gases, with special reference to the evaluation of surface area and pore size distribution (IUPAC technical report)", Pure and Applied Chemistry **87**, 1051–1069 (2015).

[113]M. Thommes, "Physical adsorption characterization of nanoporous materials", Chemie Ingenieur Technik **82**, 1059–1073 (2010).

[114]A. Trunschke, *Modern methods in heterogeneous catalysis research (presentation)*, 2013.

[115]K. S. W. Sing, D. H. Everett, R. A. W. Haul, L. Moscou, R. A. Pierotti, J. Rouquerol, and T. Siemieniewska, "Reporting physisorption data for gas/solid systems", in *Handbook of heterogeneous catalysis* (Wiley-VCH Verlag GmbH & Co. KGaA, 2008).

[116]Y. Varshni, "Temperature dependence of the energy gap in semiconductors", Physica **34**, 149–154 (1967).

[117]P. Corfdir, H. Küpers, R. B. Lewis, T. Flissikowski, H. T. Grahn, L. Geelhaar, and O. Brandt, "Exciton dynamics in GaAs/(Al,Ga)As core-shell nanowires with shell quantum dots", Physical Review B **94**, 155413 (2016).

[118]C. Hauswald, P. Corfdir, J. Zettler, V. Kaganer, K. Sabelfeld, S. Fernandez-Garrido, T. Flissikowski, V. Consonni, T. Gotschke, H. Grahn, L. Geelhaar, and O. Brandt, "Origin of the nonradiative decay of bound excitons in GaN nanowires", Physical Review B **90**, 165304 (2014).

[119]Q. Li, S. J. Xu, M. H. Xie, and S. Y. Tong, "A model for steady-state luminescence of localized-state ensemble", Europhysics Letters **71**, 994 (2005).

[120]J. Choi, "Development of nanosphere lithography technique with enhanced lithographical accuracy on periodic Si nanostructure for thin Si solar cell application", PhD thesis (Arizona State University, 2015).

[121]C. A. Schneider, W. S. Rasband, and K. W. Eliceiri, "NIH Image to ImageJ: 25 years of image analysis", Nature Methods **9**, 671 (2012).

[122]B. Münch and L. Holzer, "Contradicting geometrical concepts in pore size analysis attained with electron microscopy and mercury intrusion", Journal of the American Ceramic Society **91**, 4059–4067 (2008).

[123]M. Khardani, M. Bouaicha, and B. Bessais, "Bruggeman effective medium approach for modelling optical properties of porous silicon: comparison with experiment", physica status solidi (c) **4**, 1986–1990 (2007).

APPENDIX A

PREVIOUSLY PUBLISHED WORK IN THIS THESIS

A.1 Chapter 4 publication

The results and the main body of the text presented in Chap. 4 are based on the following peer-reviewed publication:

N. Vulic and S. M. Goodnick, "Analysis of recombination processes in polytype gallium arsenide nanowires", Nano Energy **56**, 196–206 (2019)

A.2 Chapter 5 publications

The results and the main body of the text presented in Chap. 5 are partially based on the following conference publications:

N. Vulic, J. Y. Choi, C. B. Honsberg, and S. M. Goodnick, "Silica nanosphere lithography defined light trapping structures for ultra-thin Si photovoltaics", MRS Proceedings **1770**, 31–36 (2015)

J. Y. Choi, N. Vulic, S. Goodnick, and C. B. Honsberg, "Enhanced forward scattering and transmitted light diffraction in low aspect-ratio si nanopillars for high efficiency si solar cells", in 2015 IEEE 42nd Photovoltaic Specialist Conference (PVSC) (2015), pp. 1–5

The measurements and imaging performed by the co-author are clearly indicated in the text.

APPENDIX B

CHAPTER 6 SUPPLEMENTARY INFORMATION

B.1 Pore size distribution from cross-sectional SEM images

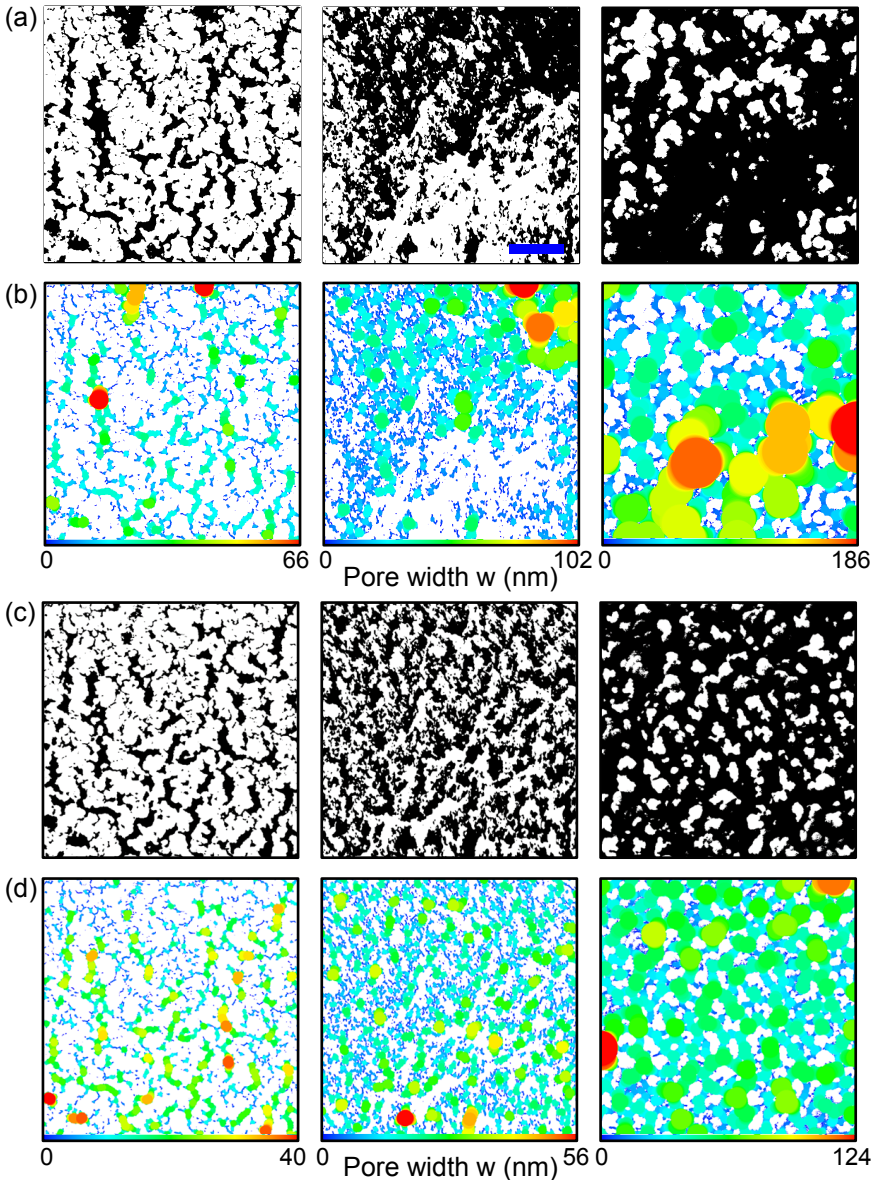

FIG. B.1: SEM cross-section images using (a) global and (c) local thresholding and the corresponding pore size distributions in (b) and (d). Scale bar corresponds to 200 nm.

B.2 BET pore size distribution, tail-end

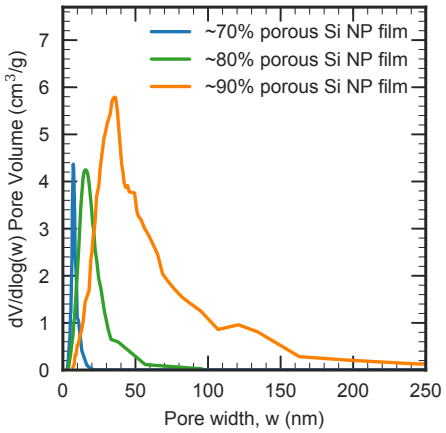

FIG. B.2: BET pore size distribution showing the tail extension of the ~90% sample.

B.3 Haze with respect to thickness of the most porous film

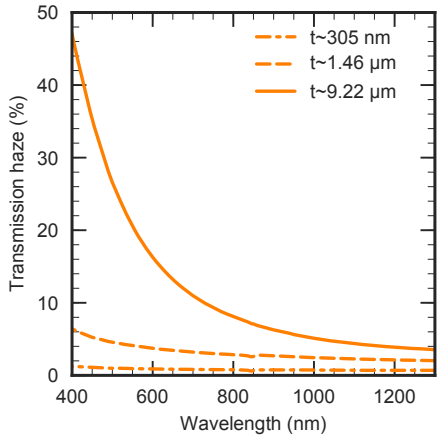

FIG. B.3: Haze of the ~90% porous film at different thicknesses.

B.4 Reference glass substrate: measured vs. simulated

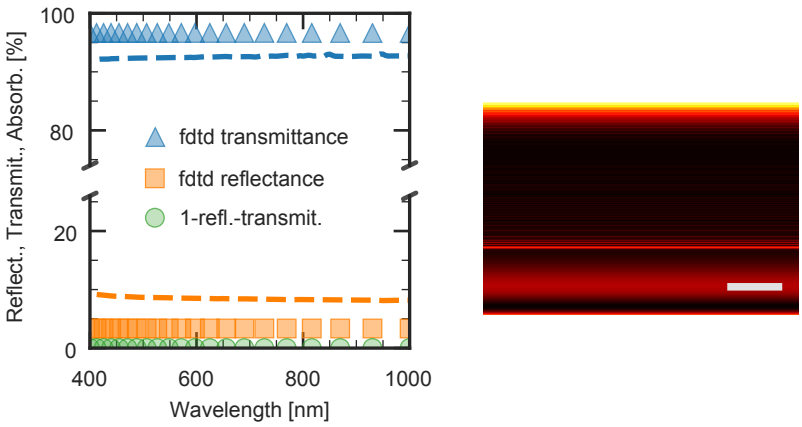

FIG. B.4: Measured (dashed lines) vs. simulated (symbols) RTA for the glass reference. The electric field energy density is included on the right. The scale bar corresponds to 100 nm.

LIST OF PUBLICATIONS

Journal publications

N. Vulic and S. M. Goodnick, "Analysis of recombination processes in polytype gallium arsenide nanowires", Nano Energy **56**, 196–206 (2019)

D. Mikulik, M. Ricci, G. Tütüncüoglu, F. Matteini, J. Vukajlovic, N. Vulic, E. Alarcon-Llado, and A. Fontcuberta i Morral, "Conductive-probe atomic force microscopy as a characterization tool for nanowire-based solar cells", Nano Energy **41**, 566–572 (2017)

S. Y. Herasimenka, C. J. Tracy, V. Sharma, N. Vulic, W. J. Dauksher, and S. G. Bowden, "Surface passivation of n-type c-Si wafers by a-Si/SiO2/SiNx stack with <1 cm/s effective surface recombination velocity", Applied Physics Letters **103**, 183903 (2013)

Conference proceedings

J. Y. Choi, N. Vulic, S. Goodnick, and C. B. Honsberg, "Enhanced forward scattering and transmitted light diffraction in low aspect-ratio si nanopillars for high efficiency si solar cells", in 2015 IEEE 42nd Photovoltaic Specialist Conference (PVSC) (2015), pp. 1–5

N. Vulic, J. Y. Choi, C. B. Honsberg, and S. M. Goodnick, "Silica nanosphere lithog-

raphy defined light trapping structures for ultra-thin Si photovoltaics", MRS Proceedings **1770**, 31–36 (2015)

N. Vulic, M. Patil, Y. Zou, S. H. Amilineni, C. B. Honsberg, and S. M. Goodnick, "Matching AC loads to solar peak production using thermal energy storage in building cooling systems - A case study at Arizona State University", in 2014 IEEE 40th Photovoltaic Specialist Conference (PVSC) (2014), pp. 1504–1509

Other conference presentations

N. Vulic, D. Mikulik, G. Tütüncüoglu, H. Potts, S. Goodnick, and A. Fontcuberta i Morral, "Surface effects in polytypic gallium arsenide nanowires (poster presentation)", in Material Research Society Spring Meeting (2017)

N. Vulic, D. Mikulik, E. Alarcon-Llado, F. Matteini, G. Tütüncüoglu, H. Potts, S. M. Goodnick, and A. Fontcuberta i Morral, "Optimization of radial junction p-i-n GaAs NWs for top-cell integration on silicon (oral presentation)", in Material Research Society Spring Meeting (2016)